A Thesis for the Degree of Ph.D. in Engineering

Material Removal Mechanism and Surface Integrity in Ultraprecision Cutting of Porous Materials

February 2018

Graduate School of Science and Technology
Keio University

Mehdi Heidari

DISSERTATION
Submitted to the School of Integrated Design Engineering, Keio University, in partial fulfillment of the requirements for the Degree of Doctor of Philosophy

For my parents for loving me unconditionally

and

For my wife, for her love, support, and sacrifices

Table of Contents

List of figures .... **vi**

List of tables .... **xii**

Abstract .... **xiii**

Acknowledgements .... **xv**

Chapter 1 : Motivation and introduction **2**

1.1 Overview 2

1.2 Significance of the research 3

1.3 Research objectives 4

1.4 Organization of dissertation 5

Chapter 2 : Literature review **8**

2.1 Ultraprecision machining technology 8

2.1.1 Introduction 8

2.1.2 Ceramic materials 10

2.1.3 Metallic materials 13

2.2 Background and previous works on porous material machining 17

2.2.1 Introduction 17

2.2.2 Porous carbon 18

2.2.3 Porous silicon 19

2.2.4 Porous titanium 20

2.2.5 Other porous materials 21

Chapter 3 : Machining of porous carbon **24**

3.1 Material and methods 24

3.1.1 Machining apparatus 24

3.1.2 Diamond tool 25

3.1.3 Workpiece materials 26

3.1.4 Machining condition 26

3.1.5 Measurement apparatus 28
3.2 Results and discussion 29
3.2.1 Categories of material removal behavior 29
3.2.2 Effects of machining parameters on cutting mechanisms 32
3.2.3 Effects of tool rake angle on cutting mechanisms 34
3.2.4 Surface roughness analysis 36
3.2.5 Bearing area curve 40
3.2.6 Surface porosity 42
3.3 Conclusions 44
Chapter 4 : Machining of porous silicon 47
4.1 Material and methods 47
4.1.1 Machining apparatus 47
4.1.2 Diamond tool 48
4.1.3 Workpiece materials 49
4.1.4 Machining conditions 50
4.1.5 Measurement apparatus 52
4.1.6 Finite element simulation 52
4.2 Results and discussion 53
4.2.1 Microfracture phenomena 53
4.2.2 Raman spectroscopy 60
4.2.3 Finite element simulation of stress distribution 62
4.2.4 Effects of wax infiltrant 64
4.2.5 Effects of tool chipping 65
4.2.6 Cutting force characteristics 67
4.2.7 Surface flatness 70
4.3 Conclusions 72
Chapter 5 : Machining of porous titanium 75

5.1 Material and methods 75

5.1.1 Machining apparatus 75

5.1.2 Diamond tool.. 76

5.1.3 Workpiece materials.. 77

5.1.4 Machining conditions.. 77

5.1.5 Measurement apparatus.. 78

5.1.6 Finite element simulation.. 78

5.2 Results and discussion.. 79

5.2.1 Cutting force characteristics.. 79

5.2.2 Shear angle 80

5.2.3 Chip morphology.. 83

5.2.4 Chip tearing 87

5.2.5 Pore deformation mechanism.. 93

5.2.6 Machined surface topography 99

5.2.7 Coolant effects.. 107

5.2.8 Tool wear and material adhesion 110

5.3 Conclusions 114

Chapter 6 : General modelling 117

6.1 Introduction 117

6.2 Porous material characteristics 117

6.2.1 Base-material properties 117

6.2.2 Pore characteristics 122

6.3 Cutting parameters and conditions 125

6.4 Conclusions 126

Chapter 7 : Conclusions and future work 131

7.1 Conclusions 131

7.2 Future work.. 132

References **133**

List of achievements **148**

List of figures

Figure 2-1: Cutting model of a round-nosed tool 12

Figure 2-2: Schematic model for cutting mechanism in silicon during ductile machining 13

Figure 2-3: Three different zones (1) shear (2) compressive pressure (3) chip-tool friction zones in the mechanism of titanium cutting 15

Figure 2-4: SEM micrograph of the free surface and back surface of chip in pure titanium cutting (feed rate=10 μm/rev, depth of cut=15 μm) 17

Figure 3-1: Schematic model for diamond turning of porous carbon 24

Figure 3-2: Photograph of experimental setup 25

Figure 3-3: (a) Tool insert geometry, (b) Tool holders for rake angle adjustment 26

Figure 3-4: SEM images of porous carbon surfaces, (a) before (b) after machining 29

Figure 3-5: Three typical material removal mechanisms: ((a1) and (a2)) shear fracture, ((b1) and (b2)) brittle fracture, and (c) grain rotation. 30

Figure 3-6: Schematic illustration of cutting mechanisms for porous carbon involving (a) shear fracture, (b) brittle fracture, and (c) grain rotation. 31

Figure 3-7: Observation results of chips: (a) and (b) show chips entering pores during cutting process; (c) and (d) show increase of chip size with depth of cut 32

Figure 3-8: The effects of depth of cut and feed rate on cutting mechanisms (a) plastic deformation (b) wavy plastic deformation and brittle fracture, type a (c) wavy plastic deformation and brittle crack, type b (d) brittle fracture, type a 34

Figure 3-9: SEM images of surfaces machined at tool rake angles of (a) 0°, (b) -15°, (c) -30° and (d) -45° 35

Figure 3-10: Schematic illustration of cutting mechanisms under a negative tool rake angle 36

Figure 3-11: (a) 2D and (b) 3D surface topographies for calculating roughness parameters R_a and S_a 37

Figure 3-12: The influence of three independent parameters on surface roughness S_a 38

Figure 3-13: Effects of feed rate and depth of cut on surface roughness S_a 38

Figure 3-14: Effects of (a) depth of cut and (b) tool rake angle on the surface roughness S_a . 39

Figure 3-15: (a) and (b) show definition of parameters S_{pk}, S_k and S_{vk} in a bearing area curve; (c) and (d) are bearing ratio curves of test 1 and test 4, respectively 40

Figure 3-16: (a) Definition of skewness distribution curve; (b) skewness distribution graph for porous carbon diamond turned at conditions: f (100 mm/min), v (30 m/min) and a (0.8 mm) 42

Figure 3-17: (a) SEM image of a diamond turned surface; (b) Image-processed results for calculating surface porosity 43

Figure 3-18: Effects of (a) three machining parameters with their levels (Table 3-1) and (b) tool rake angle on surface porosity 44

Figure 4-1: Photograph of experimental setup 47

Figure 4-2: Tool geometry 48

Figure 4-3: Cutting model for porous silicon using a round-nosed tool 49

Figure 4-4: Porous silicon workpiece (a) overview photograph (b) SEM micrograph of anodization area 50

Figure 4-5: Schematic illustration of machined areas on workpiece 51

Figure 4-6: SEM micrographs of porous silicon cross sections showing (a) before (b) after wax coating 51

Figure 4-7: SEM micrographs of machined surfaces of single-crystal silicon without pores and porous silicon at different undeformed chip thicknesses: ((a) and (c)) h_{max} =12nm, ((b) and (d)) h_{max} =794nm. 54

Figure 4-8: Magnified SEM micrographs of machined surface of porous silicon at different undeformed chip thicknesses (a) h_{max}=122 nm (b) h_{max}=532 nm 55

Figure 4-9: Schematic illustrations of four areas of pore edges 56

Figure 4-10: Material removal behavior around pores: (a) h_{max}=174 nm (f=2.0 μm/rev, a=2.0 μm); (b) h_{max} =17 nm (f=0.2 μm/rev, a=2.0 μm); (c) h_{max} =122 nm (f=2.0 μm/rev, a=1.0 μm); (d) h_{max} =12.6 nm (f=0.2 μm/rev, a=1.0 μm).................................... 57

Figure 4-11: Schematic illustrations of cutting mechanisms near a pore (a) I area (b) pore area (c) IV area 58

Figure 4-12: Schematic illustrations of cutting mechanisms in (a) II area and (b) III area 59

Figure 4-13: SEM micrograph of surfaces machined at f=2.0 μm/rev and different depth of cuts 60

Figure 4-14: Laser micro-Raman spectra of I, II, III and IV areas machined at h_{max} = 174nm (f=2.0 μm/rev, a=2.0 μm) 61

Figure 4-15: Laser micro-Raman spectra of chips in a pore.. 62

Figure 4-16: Stress distribution in the I and IV areas 63

Figure 4-17: SEM micrographs of surfaces machined using wax as infiltrant at different undeformed chip thicknesses: (a) h_{max} =12 nm; (b) h_{max} =286 nm; (c) h_{max} =724 nm; (d) h_{max} =1446 nm.. 64

Figure 4-18: Behavior of cutting in various pore areas when using wax (h_{max}=25 nm).......... 65

Figure 4-19: SEM photographs of the cutting edge, showing occurrence of micro-chippings66

Figure 4-20: Machined surface of porous silicon using (a) a new tool and (b) a chipped tool67

Figure 4-21: Cutting force measurement results.. 68

Figure 4-22: Schematic model for undeformed chip cross section... 69

Figure 4-23: Flatness of machined surfaces... 71

Figure 4-24: 3D surface topographies of (a) original porous silicon and (b) machined one ... 72

Figure 5-1: Schematic diagram of experimental setup 75

Figure 5-2: SEM micrograph and contour profile of a diamond tool edge 76

Figure 5-3: Cutting model for a round-nosed tool 77

Figure 5-4: Cutting forces of pure titanium (Ti) and porous titanium (PTi) in dry condition at depth of cut (a) 5 µm and (b) 15 µm 80

Figure 5-5: SEM micrograph of chip (f=100 µm/rev, a=5 µm) used for measuring chip thickness 81

Figure 5-6: Changes of shear angle with h_{max} 81

Figure 5-7: FE simulations of strain rate distribution at three different depth of cuts: (a) a=2.0×r (b) a=1.0×r (c) a=0.5×r 82

Figure 5-8: SEM micrographs of chip obtained at ((a) and (b)) h_{max} =7405 nm and ((c) and (d)) h_{max} =1679 nm 83

Figure 5-9: Change of resultant force angle with h_{max} 84

Figure 5-10: Schematic model for tool-workpiece contact area 84

Figure 5-11: Model for calculating specific cutting force 85

Figure 5-12: Changes of specific cutting force with h_{max} 86

Figure 5-13: SEM micrographs of chips formed by a tool after a cutting distance of (a) 250 m, (b) 75 m at h_{max}=172 nm 87

Figure 5-14: SEM micrograph of deformed chip profile (h_{max} =7405 nm) 88

Figure 5-15: Schematic model for critical thickness on chip edges at two different feed rates 89

Figure 5-16: SEM micrographs of torn chip at h_{max}=99 nm 90

Figure 5-17: SEM micrographs of chips generated at h_{max}= (a) 10 nm, (b) 30 nm (c) 50 nm. 92

Figure 5-18: Change of r_{ct} with h_{max} 93

Figure 5-19: Schematic illustration of pore deformation in cutting porous titanium 94

Figure 5-20: SEM micrographs of back sides of chips at (a) h_{max}=1676 nm, (b) h_{max}=12331 nm in cutting porous titanium, and (c) h_{max}=1676 nm, (d) h_{max}=12331 nm in cutting pure titanium 95

Figure 5-21: SEM micrographs of chips generated in porous titanium cutting at (a) h_{max}=4999 nm and (b) h_{max}=949 nm. For comparison, chips generated in pure titanium cutting at (c) h_{max}=4999 nm and (d) h_{max}=949 nm are also shown. 96

Figure 5-22: FE simulations of chip formation behavior near a pore (a=2.0×r) 97

Figure 5-23: SEM micrographs of front sides of chips of (a) porous titanium and (b) pure titanium at the same undeformed chip thickness (h_{max}=172 nm) 98

Figure 5-24: Surface roughness (Sa) of machined surface at different feed rates and depth of cuts 99

Figure 5-25: SEM micrographs and three-dimensional surface topographies of machined surfaces at ((a1) and (a2)) f=100 µm/rev (h_{max}=12331 nm); ((b1) and (b2)) f=10 µm/rev (h_{max}=1676 nm); ((c1) and (c2)) f=1 µm/rev (h_{max}=172 nm) 100

Figure 5-26: SEM micrographs of machined surfaces at (a) h_{max}=12331 nm and (b) h_{max}=172 nm 101

Figure 5-27: FE simulation of pressure distributions at (a) a=2.0r and (b) a=0.5r 102

Figure 5-28: SEM micrograph of the detached parts of a chip 103

Figure 5-29: SEM micrographs of machined surface of porous titanium at (a) h_{max}=12331 nm, (b) h_{max}=1676 nm, and (c) h_{max}=172 nm 104

Figure 5-30: Image-processed results for calculating surface porosity on the machined surface of porous titanium at h_{max} =12331 nm 105

Figure 5-31: Change of porosity percentage with h_{max} 106

Figure 5-32: FE simulations of cutting behavior near pores at (a) a=r and (b) a=2r 107

Figure 5-33: Cutting forces of pure titanium (Ti) and porous titanium (PTi) in wet condition at depth of cut (a) 5 µm and (b) 15 µm 108

Figure 5-34: Schematic illustration of coolant effects 109

Figure 5-35: SEM micrographs of tool after a cutting distance of (a1~3) 75 m and (b1~3) 250 m.........111

Figure 5-36: SEM micrographs of tool tip in cutting of porous titanium for a cutting distance of 100 m at (a) dry (b) wet conditions 112

Figure 5-37: SEM micrographs of tool tip in cutting of porous titanium for a cutting distance of 1 km at (a) dry (b) wet conditions 113

Figure 5-38: SEM micrographs of tool tip in cutting of porous titanium for a cutting distance of 2 km at dry condition.........113

Figure 6-1: Mechanisms of cutting in (a) brittle and (b) ductile materials (a=2r) 120

Figure 6-2: Mechanisms of cutting on pore edge in (a) brittle and (b) ductile materials (a=2r) 121

Figure 6-3: Principal force comparison in ductile and brittle workpiece cutting 122

Figure 6-4: Pore size effects on cutting deformation ((a1) and (a2)) small pore and ((b1) and (b2)) big pore 123

Figure 6-5: Pore shape effects on cutting deformation.........124

Figure 6-6: Flowchart of porous material categories.........127

Figure 6-7: The guideline to produce high quality surface in porous material cutting.........129

List of tables

Table 3-1: Independent variables and their levels 27

Table 3-2: Design of experiment matrix 27

Table 3-3: Experimental conditions for tool rake angle effect 28

Table 3-4: Experimental conditions for individual effect of depth of cut and feed rate 33

Table 4-1: FEM modeling parameters of workpiece 53

Table 4-2: Machining pressure 70

Table 5-1: Chemical compositions of porous titanium 77

Table 5-2: Machining conditions 78

Table 5-3: Vicker hardness (HV) of machined surface 109

Table 6-1: Material properties of porous materials workpieces 119

Abstract

With the introduction of foam structure in medical technology within the last few decades, porous materials have received great interest. Special properties of porous materials, such as high surface area, reduced volumetric density and increased permeability, which cannot be obtained with dense materials, make porous materials useful not only in medical science but also in a variety of industrial applications. Furthermore, if these materials exhibit open porosity, they become permeable and have a very high specific surface. These features are ideal for surface exchange and flow-through applications.

With the increasing adoption of porous materials, there is also an increased demand of complex products. Applications in various fields such as biomedical science have a requirement of complex shapes with special surface integrity, microstructures and porosity. Such porous parts are generally manufactured close to their final shape. However, due to their specific properties (structure), structural changes may occur during machining. Therefore, choosing the right machining method becomes an enormous challenge. High-precision fabrication technologies, such as ultraprecision cutting, are thus expected to meet these requirements and open new technological possibilities for manufacturing this class of products.

Nevertheless, unlike dense materials, the research carried out on the cutting mechanism of porous materials are limited to a few materials and mostly in the micrometer scale and above. Furthermore, the micro pores in porous materials make the cutting process more complicated, and as a result, machining mechanisms will be significantly different from those of dense materials.

This research tries to present a comprehensive investigation on the ultraprecision machining of this new class of engineering materials. Three types of porous materials were selected based on their specific characteristics, as well as their mechanism of cutting during the

machining process. The mechanism of cutting and surface integrity in the ultraprecision diamond turning of these porous materials in comparison to that of dense materials were studied by both experiments and finite element simulations under various conditions. Major factors dominating the surface integrity in the nanometer-scale ultraprecision cutting of porous materials using single-crystal diamond tools were investigated. The results demonstrated that the presence of pores significantly changed the mechanism of cutting as well as the tool wear. Experiments also showed that the challenge in ductile porous material cutting was a high level of plastic deformation, while, in brittle porous material cutting, brittle fracture around pores, filled by chips, and grain rotation leading to a sharp drop of surface porosity remained a great concern. Thus, the strategy to address each of these challenges should be different. The chip morphology and surface topography depend on different parameters such as pore size and cutting scale. By controlling these parameters and in some cases using an infiltrant, the desired machined surface with open pores can be achieved.

Acknowledgements

Firstly, I would like to express my deepest and special appreciation and thanks to my advisor Professor Jiwang Yan for the continuous support of my Ph.D. study, for his patience, motivation, and immense knowledge. His guidance helped me throughout my research and writing of this thesis.

Besides my advisor, I would also like to thank my committee members: Professor Hideki Aoyama, Professor Masaki Omiya, and Associate Professor Yasuhiro Kakinuma, for their brilliant comments and suggestions, but also for the question which incented me to widen my research from various perspectives and for letting my defense be an enjoyable moment.

My sincere thanks also go to companies, TANKEN SEAL SEIKO, QUANTUM14 KK, NAGAMINE MANUFACTURING, SHINKINZOKU INDUSTRY, and THIRD WAVE SYSTEMS for providing me with technical support and workpieces during my research.

I would like to thank Keio University for providing a sufficient environment and facilities to support my study. A great source of motivation and inspiration for me has also come from my friends and colleagues here in the Precision Machining and Nano Processing Laboratory (Yan Lab).

CHAPTER 1

Motivation and introduction

Chapter 1 : Motivation and introduction

1.1 Overview

Porous materials are a special class of engineering materials which are characterized by special properties such as a high surface area [1], reduced volumetric density, and increased permeability. This combinations of properties cannot be obtained with dense materials. They are thermally and electrically conductive and they maintain their mechanical properties at much higher temperatures compared to materials such as polymers. If they have open porosity, they are permeable and can have very high specific surface areas; these characteristics are required for flow-through applications or when surface exchanges are involved. Because of these excellent properties, porous materials are used in a variety of industrial and medical applications [2–4].

Concerning applications, a wide variety of base material can be used in manufacturing of porous structures, e.g. porous carbon is used in industries as air bearings, while porous silicon has attracted great attention because of its applications in Li-ion batteries and solar cells owing to its high theoretical capacity, wide absorption band and high transmission respectively [5–9]. Porous titanium is a potential material for various dental and orthopedic applications due to its excellent biocompatibility properties [10,11]. In addition, two important factors, namely porosity and pore size, must be controlled during the manufacturing process to make them more suitable for their applications. Porosity is defined as the ratio of total pore volume to apparent volume of the particle and pores size is determined based on average diameters. The variations in porosity and pores size significantly influence the function of porous materials, e.g. higher porosity increases the adherence between an implant and a neighboring

bone, as well as their biocompatibility in porous titanium, while it decreases mechanical properties such as structural strength.

The required structure and properties strongly depend on the application. Closed porosity is generally sought for lightweight structure and thermal insulation, while open porosity is particularly of interest for applications requiring permeability and involving surface exchange phenomena. Due to their unique combination of properties, open cell structures have been used in many different applications such as for the fabrication of filters, implants, heat exchangers, electrodes, batteries, and fluid treatment units, as well as for sound absorption [12].

1.2 Significance of the research

Porous metals can be generated through a multitude of manufacturing processes. The most common operations used to fabricate them are sintering, deposition of metals on polymeric foams, powder metallurgy, and anodization. These materials components fabricated by net-shape technologies require further machining processes to improve the surface quality and form accuracy, and in turn, the added value of the products.

The great challenge in the machining of porous materials is the presence of pores in the porous structure. The mechanism of cutting in pore area is also dependent on its base material, e.g. material removal of ductile material like titanium is significantly different from that of brittle material like silicon. This makes the cutting process more complicated and difficult. The lack of knowledge in material removal mechanism of porous materials leads to the low quality of machined surface that has a remarkable impact on limiting their applications.

High-precision fabrication technologies, such as ultraprecision cutting, are expected to meet these requirements and open new technological possibilities for manufacturing this class of products. Ultraprecision cutting, which is often referred to as single-point diamond turning

(SPDT), is an established technology for manufacturing microstructured surfaces with nanometer-level form accuracy, high surface quality, and complex shapes.

1.3 Research objectives

The objectives of this research are as follows:

1. To investigate the fundamental mechanisms of material removal in micro/nanometer-scale single point diamond turning of porous materials compared with those of dense materials.
2. To determine the impact of different cutting parameters and undeformed chip thickness down to the nanometer scale on the mechanism of cutting and surface integrity.
3. To study the behavior of hydrostatic stress induced by the cutting tool near the edge of a pore in porous brittle material cutting.
4. To develop a method, using wax as an infiltrant to prevent chips from filling pores during machining of porous silicon and improve surface quality to the nanometer level.
5. To understand the changes in shear angle and specific cutting force as undeformed chip thickness decreases from the micro down to the nanometer scale in porous metal cutting compared to dense metal cutting.
6. To consider the effects of pore size and location on chip morphology and surface topography in ultraprecision machining of porous titanium.
7. To identify the characteristics of tool wear in the cutting of porous structure compared to a dense structure in both porous silicon and porous titanium.

1.4 Organization of dissertation

Chapter 1 provides the introduction and overview of the issues regarding research. The research significance and the research objectives were included in this chapter.

Chapter 2 provides an introduction to ultraprecision cutting technology and an overview of the mechanism of cutting of hard brittle materials like ceramic and ductile materials like metallic materials, as well as past research works on the machining of porous materials.

Chapter 3 presents the results of the investigation on fundamental characteristics of material removal and surface formation in diamond turning of porous carbon. Influence on surface roughness by observed deformation, fracture, and rotation of carbon grains on a tool tip is revealed. It also presents the result of analysis of variance of experimental data to indicate the effect of feed rate, cutting speed and depth of cut on surface roughness. The effects of tool rake angle on material removal behavior are also considered in this chapter.

Chapter 4 contains the discussion of the fundamental mechanisms of material removal in the ultraprecision diamond turning of porous silicon. Influence of anisotropy and cutting stress field near the edge of a pore is investigated and cutting condition to accomplish flatness in nanometer scale is presented. Three types of material removal behaviors in various areas around a pore are confirmed based on the direction of cutting with respect to the pore edge orientation in the chapter. The results of the material structures of subsurface layers are also presented. A method of using wax as an infiltrant is developed to improve the surface quality in terms of decreasing brittle fractures. The results of measuring the cutting forces in machining of porous silicon compared to silicon are illustrated. Tool wear results are also presented in this chapter.

Chapter 5 presents the discussion of the fundamental mechanisms of material removal and surface integrity in ultraprecision cutting of porous titanium in comparison with pure

titanium which has no pore. The chip formation behavior of pure and porous titanium in nanometer-scale ultraprecision diamond turning tests was investigated by both experiments and FE simulation. The results of the changes in shear angle and specific cutting force as undeformed chip thickness decreases to the nanometer scale are identified in this chapter. The role of chip tearing and welding phenomenon plays on porosity percentage of the machined surface are clarified. The effects of pore size and location on chip morphology and surface topography in ultraprecision machining of porous titanium are considered. Coolant effect on the mechanism of cutting and the hardness of machined surface in porous titanium cutting are recognized. The characteristics of tool wear in the cutting of porous structure compared to a dense structure in both porous titanium and pure titanium are presented in this chapter.

Chapter 6 presents the general modeling for machining of the porous materials based on their material properties and pore characteristics which provides a guideline to decide cutting parameters.

Chapter 7 consists of the overall conclusion of the research. The future work of this research area is also included.

CHAPTER 2

Literature review

Chapter 2 : Literature review

2.1 Ultraprecision machining technology

2.1.1 Introduction

Ultraprecision cutting is an established technology for manufacturing microstructured surfaces with nanometer level form accuracy, high surface quality, and complex shapes. It has been commonly used to fabricate high-quality optical components without any post-polishing, such as digital camera lens, CCD camera lens, DVD lens etc. Some typical optics applications cover lighting, telecommunications, medical facilities, military, and aerospace [13,14]. During the 1980s, Taniguchi proposed a predictive map of development in ultraprecision manufacturing [15,16], and this remains true as we approach 2020. Recently, Shore et al. [17] mentioned that Taniguchi's chart is analogous to Moore's Law which is a mid-1960s prediction for the next 50 years of manufacturing precision.

The 21st century has witnessed the rapid emergence of a variety of non-conventional micro-/nano-machining (MNM) processes capable of being applied to a range of engineering materials, including metals, ceramics, plastics, and composites. Miniaturization has pushed manufacturing improvements with regrads to attainable accuracies and tolerances to the sub-micron range, especially in the fields of medicine and biotechnology as well as optics and electronics. Further improvements are necessary for applications relating to fuel cells, microscale pumps, valves and mixing devices, fluidic micro-chemical reactors, micro-fluidic systems, micro nozzles for high-temperature jets, micro holes for fiber optics, micro moulds and deep X-ray lithography masks etc. [18]. Micro-/nano-machining (MNM) processes which are used to finish these components can broadly be divided into two major categories based on whether they involve the addition of material or the removal of material during the process.

The first category involves deposition of material and includes processes such as Ultrasonic laser deposition, Chemical vapor deposition, Rapid prototyping, LIGA and Electric discharge deposition. The second category of micro-machining involves the removal of material. This may be accomplished by mechanical, chemical or physical means. The focus of this research work is the diamond-machining process, which falls into the category of material removal processes as a mechanical process. Machining by mechanical means is considered to be almost universal in its applicability [13] to most materials.

One major difference between the micro and nanometer scale machining is the size of the attainable chip thickness [18]. Aside from this major difference, the chip formation mechanism, the distribution of cutting forces, the role of material microstructure and crystal anisotropy, and the elastic recovery of the machined surface, all result in the transition of the scale of machining from the macro to the nanometer level. The foremost of these is the mechanism of chip formation which shifts from continuous to discrete as the cutting scale decreases [19].

Single point diamond turning (SPDT) is one of the most efficient ultraprecision material removal processes. It is capable of removing material at the scale of a few nanometers to produce optical quality machined surfaces using a single point diamond-cutting tool. SPDT provides machining form accuracy and machined surface finish that are among the best ranges obtained via a multitude of processes such as lapping and polishing [17]. Moreover, the components produced through an SPDT operation have a much better metallurgical structure than the one obtained through polishing and lapping processes [20]. This couples further with the fact that SPDT offers the flexibility of generated figure, better step-definition, deterministic form accuracy and economy of fabrication time [13]. Nevertheless, the performance and cutting mechanism of SPDT process towards two class of engineering materials, ceramic and metallic materials are different.

2.1.2 Ceramic materials

Although ceramic materials for technical applications have been known for more than two hundred years, unlike traditional materials in composition, microstructure, and properties, have been developed since approximately 1970. Whereas silicate ceramics and refractory materials are basically derived from natural minerals and manufactured by comparatively simple processing steps, this new class of materials, the "advanced", "high-tech," or in Japanese terms "fine" ceramics requires an entirely different fabrication route starting from chemically well-define, fine, highly-purified, and artificial raw materials. These materials have been created for a variety applications in which other conventional materials like metals or polymers have failed. Due to the large variety of chemical, electrical, biological, and mechanical properties that ceramics presently exhibit, there are almost no industrial applications without ceramics. In the electronic and manufacturing industries, as well as in technologies that require materials sustaining extremely high temperatures and corrosive environments, high-tech ceramics play the role of key materials; novel technologies, processes, and machines are finally made possible only by means of specially tailored ceramics [21].

Today's advanced technology industry relies on the development of new advanced materials. In particular, hard brittle materials such as glass, silicon, quartz, and other kinds of ceramics are important for recent high technology industry because of their unique characteristics. However, their primary characteristics (e.g., fragile, hard, and brittle) are disadvantageous for practical use in terms of productivity and cost-efficiency. A breakthrough in machining technology, especially for hard-brittle materials, is needed for the development of high technology industry [22].

Bridgman [23] was one of the first who considered the possibility of machining brittle materials in the ductile-regime mode. They showed that, under high hydrostatic pressure, a

brittle material exhibited ductility. In the late 1990s, Blake and Scattergood [24] indicated that there is a critical chip thickness separating the regime of plastic deformation from brittle fracture material removal. They suggested a new machining model to explain the ductile-regime machining of brittle materials which has also been verified experimentally. Figure 2.1 shows a schematic classical model for diamond turning with a round-nosed tool.

During SPDT operation, the undesirable fracture damage is assumed to initiate at the critical chip thickness, which propagates up to a depth. The critical crack length varies along the nose radius according to the feed rate of the tool. The crack does not penetrate below the subsurface damage at smaller feed rates and hence does not affect the final machined surface. However, as feed rate increases, cracks begin to propagate into the final cut surface. As long as the fracture damage does not penetrate into the final machined surface, ductile-regime machining is achieved. It is worth mentioning that the fractured material in the remaining region of the uncut shoulder is carried away by the tool in the succeeding passes.

Now, it is well-known that there is a brittle-ductile transition in chip formation during the cutting of brittle materials using SPDT when the undeformed chip thickness is reduced [25–27]. When undeformed chip thickness is less than the critical undeformed chip thickness, no cracks are generated. When the undeformed chip thickness is larger than the critical value, however, microfractures are generated and the density of microfractures increases with the undeformed chip thickness.

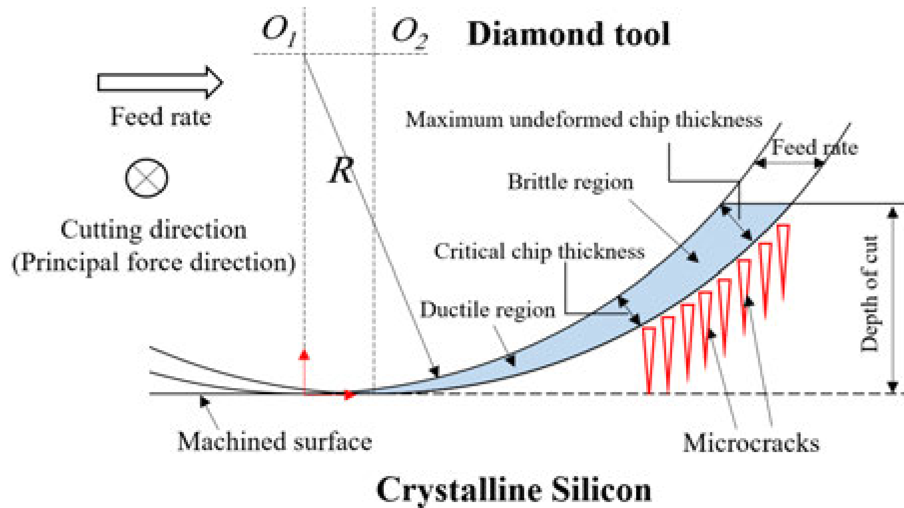

Figure 2-1: Cutting model of a round-nosed tool

Ductile mode cutting of a brittle material is based on hydrostatic pressure (compressive stress) which determines the extent of plastic deformation prior to fracture [28,29]. This stress state exists in the vicinity of cutting edge and is dependent on tool rake angle and undeformed chip thickness. When undeformed chip thickness becomes small enough, the entire cutting region will be under the high compressive stress state, such a high hydrostatic pressure becomes a prerequisite for machining brittle materials by plastic flow at room temperature [30] as shown in Figure 2-2. In addition, high hydrostatic pressure can prevent microcrack propagation by closure of cracks [31]. In the case of single crystal silicon, it is generally accepted that a structural change from diamond cubic (Si-I) to a metallic state β-Sn (Si-II) occurs under the indenter during loading as a result of the high pressure (10–13GPa). The material around the indenter would then become ductile enough to sustain plastic flow. Measurements of electrical conductivity during indentation close to the indenter on silicon showed a significant increase in conductivity, from semiconducting to highly conducting [32,33], which strongly supports the idea that a transformation into the metallic state occurs underneath the indenter. However, the metallic phase is not stable at low pressure (~4 GPa). In silicon cutting, the machining pressure in the ductile regime is higher than 10 GPa [34], which is sufficiently high to make silicon undergo phase transformation.

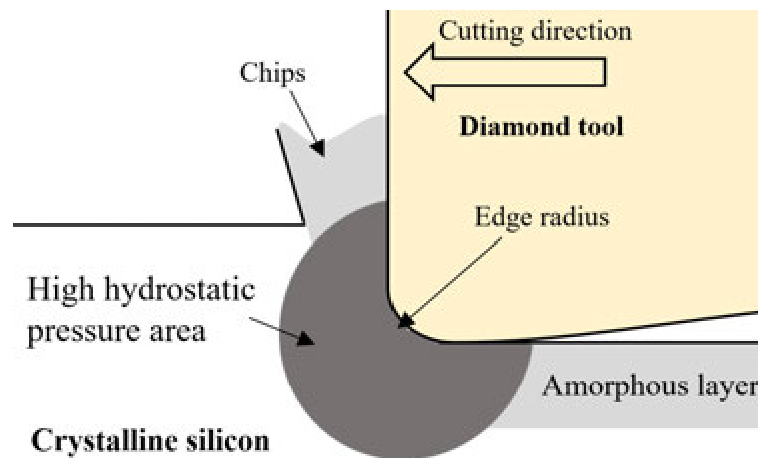

Figure 2-2: Schematic model for cutting mechanism in silicon during ductile machining

2.1.3 Metallic materials

Unlike ceramic materials, where main priority is cutting ceramics in ductile mode, the major reason to use ultraprecision machining in metallic materials is achieving a high level of surface quality (good roughness) required for distinct applications. Historically, the ultraprecision metal cutting in the present sense had begun to be investigated in the 1960's with the advent of demands in advanced science and technology for energy, computer, electronics and defense application. The ultraprecision metal cutting at present is a key technique for the manufacture of components used for the systems in a variety of advanced science and technology applications. By using precision machine tools available at more than half a century ago, it started its developments as a promising method of fabricating dedicated mechanical parts of high quality essential for a particular advanced system.

Along with wide variety of industrial applications, more recent applications of ultraprecision metal cutting are for the manufacture of medical parts with sophisticated form and extremely complex geometrical and surface quality. Titanium is one of the metallic materials attracting more and more attentions in medical applications in recent years [35,36].

Titanium is very difficult to machine owing to its low thermal conductivity, high strength and low modulus of elasticity [37–39]. To overcome the difficulties in machining titanium and its alloys, extensive studies have been done in the past decades on their cutting mechanism. These researches can be roughly classified into three main categories. First, there are studies on the fundamental cutting mechanism and chip formation and their relationship to mechanical properties of titanium [40–46]. Second, there are researches on the optimization of machining conditions to enhance the machinability of titanium [47–50]. Third, there are researches on tool wear mechanism and surface integrity in titanium machining [51–54]. However, unlike brittle materials, most of the previous cutting experiments were conducted on the micrometer scale or larger. The research work on the ultraprecision cutting of titanium is very limited.

Zareena and Veldhuis [55] investigated the tool wear mechanism in ultraprecision cutting of titanium and Ti-6Al-4V using single-crystal diamond tools. They found that high temperature and high pressure at the tool-chip interface initiated the chemical interaction between titanium and diamond. Schneider et al. [56,57] analyzed the surface integrity in titanium cutting using quick-stop orthogonal cutting tests and considered the effect of undeformed chip thickness (ranging from 0.1 μm to 10 μm) on cutting forces. Ruibin and Wu [58] investigated the influence of machining parameters on surface roughness and cutting forces. Colafemina et al. [59] studied surface damage in machining of titanium and found the surface damage was due to the material delamination phenomenon. However, to date, there is no available literature on chip formation mechanism in diamond turning of titanium down to the nanometer scale. Regarding demands for nano-precision surfaces have rapidly increased in advanced engineering fields, it is necessary to understand the cutting mechanism in the nanometer scale.

Chip formation and its morphology are important features of metal machining and yield essential information on the cutting process itself [41]. An intense shear is generated between the tool tip engaged in the material and the workpiece, the strain in the chip is confined to narrow bands between the segments called shear zone with very little deformation within these segments [60], (Figure 2-3).

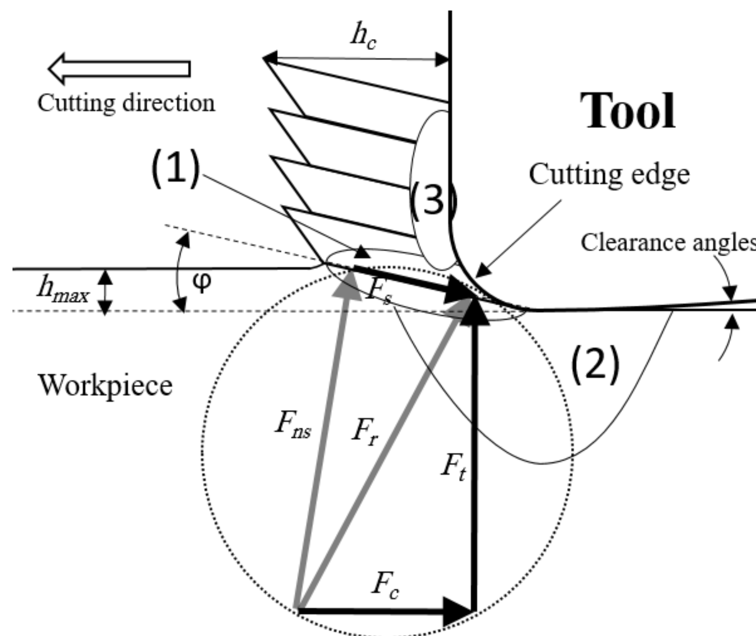

Figure 2-3: Three different zones (1) shear (2) compressive pressure (3) chip-tool friction zones in the mechanism of titanium cutting

In chip's segmentation, there is a competition between the rate of decrease in strength resulting from the local increase in temperature and the rate of increase in strength due to strain hardening in the primary shear zone. As soon as shear stress induced by tool edge exceeds the yield strength of material the chip formation occurs on a particular shear plane. The energy associated with this deformation is converted into thermal energy. This thermal energy along with titanium's poor thermal properties leads to high temperature locally in the cutting process. Local softening due to high temperature helps the strain to continue in the same plane instead of moving to a new plane in the colder material. The saw-tooth chips produced under this condition have been classified as "catastrophic shear chips" and the forming process of which has been referred to as "catastrophic thermoplastic shear" or "adiabatic shear" [40,61–64].

In addition to shear zone, there are two other zones playing important role in mechanism of cutting and chip formation. One of those is compressive pressure zone just beneath of cutting edge induced by thrust force. Nakayama and Tamura [65] have pointed out that the shear zone extends downward beyond the intended depth of cut, thus compressive pressure zone is effected by shear zone due to the natural consequence of the fact that shear deformation does not occur on a single plane (shear plane) but in a zone of finite thickness (shear zone) . This zone induces the plastic flow in the subsurface layer and has a remarkable effect on surface integrity. In such cases, after the cutting edge has passed, the newly machined surface will have a tendency to rise elastically and, possibly, even plastically. Consequently, friction between the tool flank and the machined surface is unavoidable even for a very sharply honed cutting tool [65]. As the tool wears out, plastic deformation flow and subsequently the thickness of the deformed layer increase, due to microstructural alterations [51,53]. The depth of these micro-structural alterations beneath the surface has been observed to increase when the cutting speed and feed rate are increased in conventional machining [54], and also prolonged machining with worn tools was found to increase microstructural alterations to the material in the form of severe plastic deformation and a thicker 'disturbed' layer on the machined surface [51].

The third zone is friction area between chip and rake face. Although this zone does not affect the machined surface, it, however, has a significant influence on chip formation and tool wear. Upsetting the inclined wedge of chips by the advancing tool and sliding over the tool surface causes further plastic deformations to arise in the boundary layers. In the "chip-tool friction zone" (in some references it is mentioned as secondary shear [40]), the deformation texture of which forms parallel to the rake face gives the impression of a viscous flow process with a high degree of deformation [66]. As shown in Figure 2-4 the free surface and the back surface of the chip resulting from the described chip formation process are very different from

each other. The free surface is very rough and the lamella pattern can be found on the free surface while the back surface is very smooth.

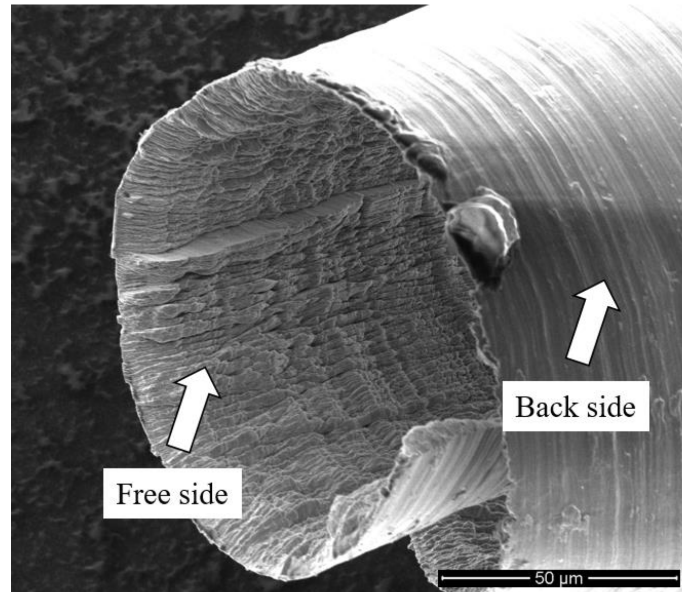

Figure 2-4: SEM micrograph of the free surface and back surface of chip in pure titanium cutting (feed rate=10 µm/rev, depth of cut=15 µm)

2.2 Background and previous works on porous material machining

2.2.1 Introduction

With the introduction of metal foams in medical technology within the last decades, porous materials have received great interest. Porous materials are a potential material for various medical applications. In biomedical applications, in addition to requirements for complex shapes, surface integrity, microstructure, and porosity significantly influence their applications. During machining of porous parts, owing to their specific structure, structural changes may take place typical for porous materials only, such as variations in their density and the state of the inter particle contacts. As a result, choosing the best method is a great challenge. High-precision fabrication technologies, such as ultraprecision cutting, are expected to meet these requirements.

Unlike nonporous materials, where a large number of investigations have been carried out in the field of micro and above machining process, discussing cutting mechanism and challenges ahead in fairly great detail, the researches carried out on the cutting mechanism of porous materials are very limited to a few materials and mostly in micron scale. The micro pores in porous materials will make the cutting process more complicated and difficult, thus their machining mechanism will be distinctly different from those of dense materials. In this part, it is tried to present a comprehensive review of the existing research works on the cutting of porous materials with a focus on porous carbon, porous silicon, and porous titanium.

2.2.2 Porous carbon

Porous carbon developed at Oak Ridge National Laboratory (ORNL) [67,68] is being investigated as a material to improve single and multiphase heat transfer due to the high material conductivity of the graphitized carbon material. Now porous carbon has been used in different applications one of which is the air bearing industry. An air bearing is a new generation of bearing having advantages such as zero friction and wear, no need to be lubricated, high precision and high speed. Air bearings are increasingly used in various fields such as ultra-precision machine tools. One of the most important parts of air bearing is porous media, where porous carbon has been one of the best materials for this purpose. Owing to the special surface structure of porous carbon, if there is an air supply failure, the counterpart surface will not be damaged and bearing may run without air pressure. Moreover, compared with non-porous materials, porous carbon provides a uniform distribution of air pressure, which enhances the spindle rotation accuracy. However, the surface quality of porous carbon depends on its machining method. To improve the service life, load capacity and wear resistance of bearing parts, it is essential to reduce surface peak height and increase core roughness depth during the machining process. Nevertheless, there are a few problems such as surface fractures,

sharp protrusions, and grain dislodgements, etc., in conventional grinding and cutting of porous carbon, which limits the surface quality improvement. However, a few researches have been carried out on the fabrication of bulk carbon to produce a porous structure in the base material [69,70], to date, there is no available literature on the mechanism of porous carbon cutting.

2.2.3 Porous silicon

The silicon-based porous material is a very promising material due to its excellent physical and thermal properties, and compatibility with silicon-based microelectronics [71]. Porous silicon is a suitable dielectric material for its large surface area within a small volume, controllable pore sizes, and active surface chemistry [72]. These features lead to interesting optical properties by mixing silicon with air in effective medium approximation. On the other hand, chemical and biological substances, cells and molecules are able to penetrate into the pores to change the performance of the original system. These excellent characteristics are driving force behind research into different applications of porous silicon such as optical sensing [73] and biomedical applications [74–76]. Recently, porous silicon has attracted great attention because of its applications in Li-ion batteries, owing to its high theoretical capacity. For example, a porous silicon electrode with Li22Si5 composition has a specific capacity of 4200 mAh/g, which is over 10 times that of an existing carbon anode [5,6]. Moreover, the application of porous silicon in solar cells is rapidly increasing as it has the capability of a wide absorption band and high transmission in a wavelength range from 700 to 1000 nm [7–9].

Porous silicon is prepared by anodization of a single-crystal silicon wafer and needs to be manufactured into various shapes for industrial and biomedical applications. Normally, the anodized porous silicon surface is uneven, which affects its performances in specific applications [9], thus needs to be flattened precisely. Conventionally, polishing has been used for smoothing a silicon wafer. However, it cannot be used for porous silicon because pores

would be filled and closed by abrasives in the slurry during the polishing process. Face milling and peripheral grinding which were used for machining sintered foams [77] are not suitable for porous silicon machining in terms of surface quality. Another alternative method is turning. However, to date, there is no available literature on the diamond turning of porous silicon. Silicon is a highly brittle material, thus its machining mechanism will be distinctly different from that of ductile metal materials.

2.2.4 Porous titanium

Titanium is an attractive material due to its unique properties such as high strength, light weight, thermal stability, and exceptional corrosion resistance. These excellent properties make titanium and its alloys useful in biomedical, chemical and petrochemical applications and aerospace and marine industries. Porous titanium is a potential material for various dental and orthopedic applications due to its excellent biocompatibility properties. In biomedical applications, in addition to requirements for complex shapes, surface integrity, microstructure, and porosity significantly influence the adherence between an implant and a neighboring bone, as well as their biocompatibility [10,78,79].

A few researches have been carried out on the cutting mechanism of porous titanium in micron scale. Abolghasemi Fakhri et al. [10] proposed an image analysis approach to optically consider the porosity in micro-milling process of porous titanium, with emphasis on cutting force monitoring. The result showed the possibility of estimating the area of porous material removal from the optical image. Bram et al. [77] monitored cutting force during grinding and face milling of sintered titanium foam to investigate the surface quality and tool wear. However, to date, there is no available literature on the mechanism of ultraprecision cutting of porous titanium in the nanometer scale.

2.2.5 Other porous materials

While the research work on machining of porous materials rarely can be found in literature, two porous materials in particular, powder metallurgical (PM) steel and porous tungsten, have been subject of considerable interest in recent years.

Porous steel (steel foam) formed by powder processing and primarily consists of powder synthesis, compacting, and sintering the structural constituents [80]. In powder metallurgy (PM) parts production, there is a large number of shapes that are difficult or impossible to produce by pressing without machining indicating a requirement for secondary finishing. However, machinability is considered to be poor due to several parameters including the hardness of powder particle, buit-up-edge formation and decreased plasticity [81–84].

There is a remarkable difference between PM steel and other porous materials that puts PM steel in different categories. Unlike porous materials, which are the subject of this work, open surface porosity is not desirable in machining of PM steel. The requirement for having proper surface porosity after machining process makes porous material machining more complex. This causes porous materials that surface porosity is not important features to be excluded from categories.

The most systematic research work on specific porous material with desirable open surface porosity have been carried out in The Institute for Sustainable Manufacturing (ISM) at the University of Kentucky where porous tungsten has been the subject of research since 2005. Chen [85] was the first in this group to conduct an investigation to improve the surface quality with a high level of surface porosity in porous tungsten machining. They studied the effects of tool geometry, tool material properties, work material properties, and machining parameters on the porosity in face turning of porous tungsten. In 2008, Tarter et al. [86] applied cryogenic methods to the machining of porous tungsten for dispenser cathode matrices. Then, Pusavec et

al. [87,88] used a multi-objective optimization model based on genetic algorithms to achieve the required post-machining porosity and surface roughness, the optimum machining parameters and tool grade in cryogenic machining method. Schoop et al. [89] observed the effect of different cryogenic pre-cooling times on the as-machined surface porosity of 81% dense porous tungsten. The results showed that longer pre-cooling condition led to a more uniform porosity distribution throughout the machined surface. In other work [90,91], they tried to enhance both surface porosity and surface roughness by controlling cutting temperature as well as other geometric parameters such as rake angle. Nevertheless, the main effort in these research has been focused on developing cryogenic machining method, not understanding fundamental of material removal mechanism.

One of the main obstacles in the way of development in machining process of porous materials is a lack of knowledge in understanding material removal mechanisms and surface formation in two main categories of porous materials including porous brittle and porous ductile materials. In this work, it is tried to select porous materials based on these two categories, as a result, porous silicon as a brittle material and porous titanium as a ductile material were selected as workpieces. Both of these materials are difficult-to-cut compared to porous carbon that is categorized as brittle material but not difficult to cut materials.

We hope this research paves the way and provides a research platform for future studies in this field.

CHAPTER 3

Machining of porous carbon

Chapter 3 : Machining of porous carbon

3.1 Material and methods

3.1.1 Machining apparatus

In order to investigate the mechanism for diamond turning of porous carbon experimentally, the face turning method was applied by using an ultra-precision lathe. Figure 3-1 schematically shows the model for diamond turning of porous carbon.

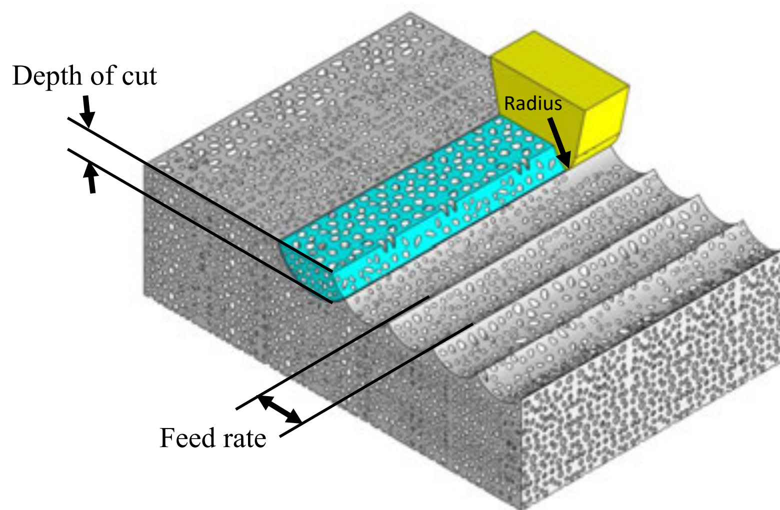

Figure 3-1: Schematic model for diamond turning of porous carbon

The cutting experiments were conducted on a three-axis CNC ultraprecision machine, NACHI ASP-15 (NACHI-FUJIKOSHI CORP.). The machine has two perpendicular linear tables supported by high-stiffness hydrostatic bearings driven by servomotors. To prevent from backlash movements in machine rotary table, it is supported by hydrostatic bearings and driven by a friction drive. The machine is equipped with laser hologram scales to accurately position all of these tables. The linear tables can be moved at 1 nm per step and the rotary table is able to rotate with an angular resolution of 0.00001°.

In order to fix the workpiece to the spindle and adjust the cutting speed, a workpiece holder was designed and fabricated. This holder uses a sliding mechanism to change cutting speed by adjusting the distance between the workpiece and the center of the spindle, and then the workpiece was fixed using two screws. In addition, on the opposite side of the workpiece, a metal piece was fixed to keep dynamic balance during spindle rotation, as illustrated in Figure 3-2.

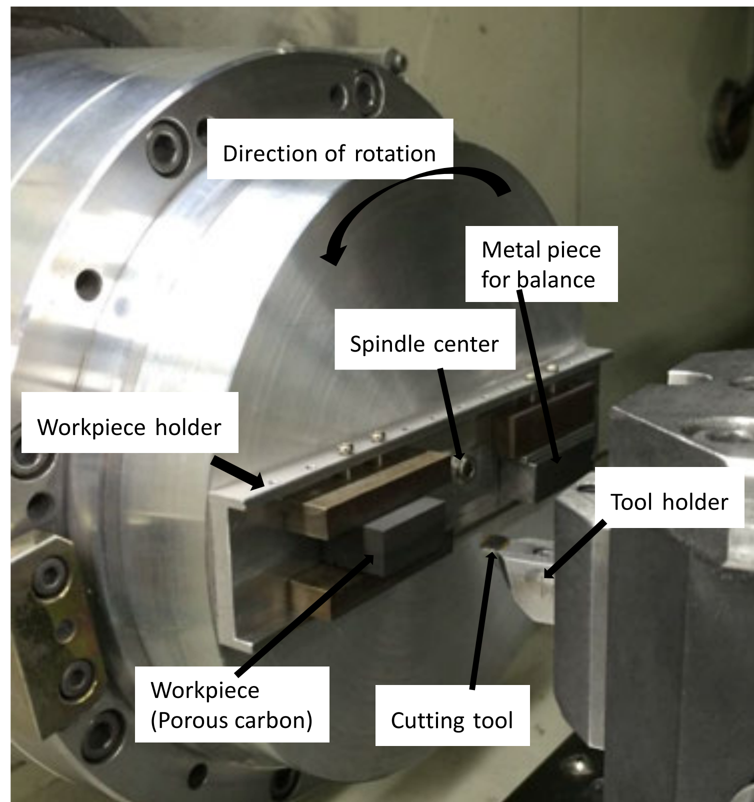

Figure 3-2: Photograph of experimental setup

3.1.2 Diamond tool

A commercially available diamond cutting tool with a nose radius of 10 mm, rake and clearance angles of 0° and 6°, respectively, was used in experiments. The tool geometry is shown in Figure 3-3a. For the purpose of changing rake angles, four tool holders having various slopes were designed to enable rake angle of 0°, –15°, –30° and –45°, as shown in Figure 3-3b.

Thus, in all the tests, the same diamond insert with 0° rake angle was used. In this case, the relief angle was changed accordingly, the effect of which was neglected.

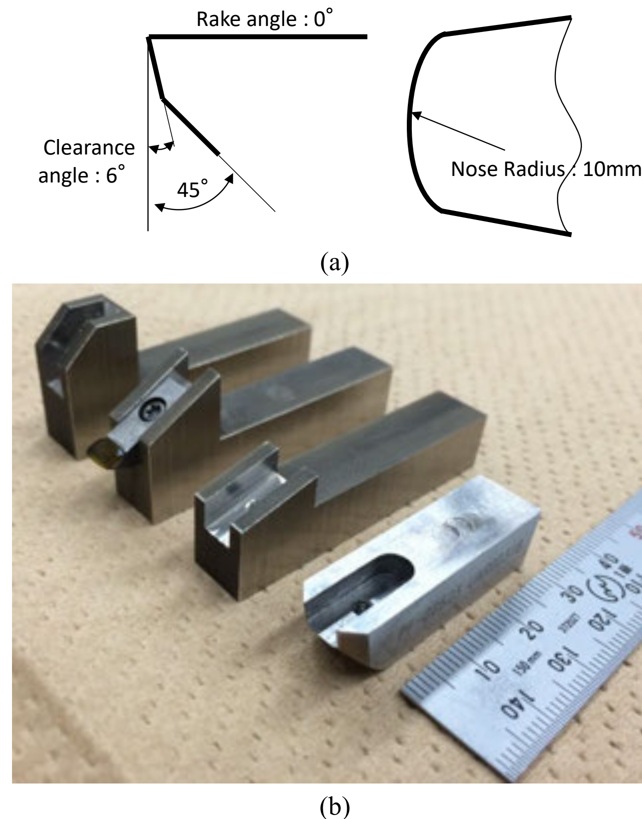

(a)

(b)

Figure 3-3: (a) Tool insert geometry, (b) Tool holders for rake angle adjustment

3.1.3 Workpiece materials

The porous carbon workpiece (30.0 mm × 20.0 mm × 10.0 mm) with purity of 0.99, the porosity of 35% and average pore size of 4μm, supplied by TANKEN SEAL SEIKO CO., LTD. was used in the experiments.

3.1.4 Machining condition

Three independent variables including feed rate, cutting speed and depth of cut, each in four levels were considered in these experiments. As Table 3-1 shows, the range of cutting parameters used were: feed rate (*f*) = 25, 50, 75, 100 mm/min, cutting speed (*v*) = 30, 60, 90, 120 m/min and depth of cut (*a*) = 0.2, 0.4, 0.6, 0.8 mm.

Table 3-1: Independent variables and their levels

No.	Factors	Units	Notation	Level -2	Level-1	Level+1	Level+2
1	Feed rate	mm/min	*f*	25	50	75	100
2	Cutting speed	m/min	*v*	30	60	90	120
3	Depth of cut	mm	*a*	0.2	0.4	0.6	0.8

A full factorial set of experiments would require 64 experimental test (three factors at four levels). In this work, Taguchi design of experiments (DOE) was used to reduce the number of tests to 16, which is called L_{16} Taguchi DOE. This design is listed in Table 3-2. This L_{16} Taguchi set of experiments, along with 16 other tests were used to clarify the effect of different parameters on material removal mechanism and surface quality.

Table 3-2: Design of experiment matrix

No.	Depth of cut (mm)	Feed rate (mm/min)	Cutting Speed (m/min)
1	0.2	25	30
2	0.2	50	60
3	0.2	75	90
4	0.2	100	120
5	0.4	25	60
6	0.4	50	30
7	0.4	75	120
8	0.4	100	90
9	0.6	25	90
10	0.6	50	120
11	0.6	75	30
12	0.6	100	60
13	0.8	25	120
14	0.8	50	90

15	0.8	75	60
16	0.8	100	30

To survey the influences of tool rake angle on the cutting mechanism, four experiments were performed under conditions shown in Table 3-3.

Table 3-3: Experimental conditions for tool rake angle effect

No.	Rake angle (°)	Depth of cut (mm)	Feed rate (mm/min)	Cutting speed (m/min)
1	0	0.4	50	60
2	-15	0.4	50	60
3	-30	0.4	50	60
4	-45	0.4	50	60

3.1.5 Measurement apparatus

In order to evaluate the surface roughness, a white light interferometer was used and the surface profile was analyzed by the Talymap software (Taylor Hobson Ltd.). According to Taguchi L_{16} DOE matrix, 16 experiments were performed and after each experiment, eight different areas of the machined sample were measured and analyzed and then the average was taken as the final result. In addition, scanning electron microscopy (SEM) and field-emission scanning electron microscopy (FE-SEM) were used to observe the sample surfaces. These images were then used for analyzing the percentage of surface porosity using the ImageJ software. In this study, “surface porosity” is evaluated, not volumetric porosity.

3.2 Results and discussion

3.2.1 Categories of material removal behavior

To clarify the mechanism of material removal in cutting, the machined surfaces were observed by FE-SEM. Figure 3-4a and Figure 3-4b are two SEM photographs of the sample surface, before and after cutting, respectively. Before machining, the surface is very rough, with protruding carbon particles and big craters. After machining, however, the surface has become obviously flattered, where some of the grains have been sliced to be very smooth.

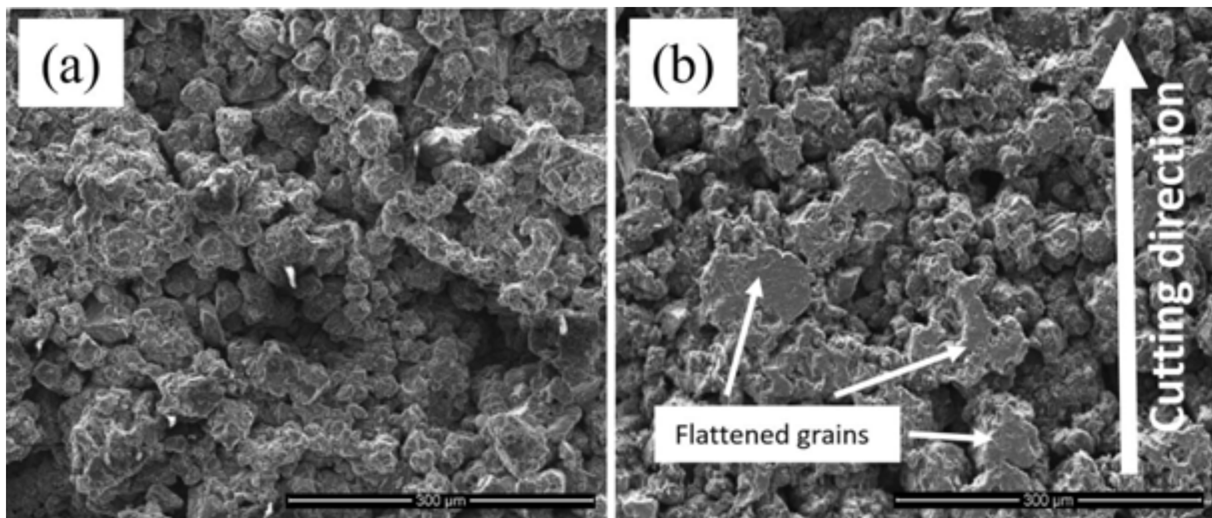

Figure 3-4: SEM images of porous carbon surfaces, (a) before (b) after machining

Through observation at higher magnifications, three types of material removal mechanisms were identified in the machining of porous carbon, namely, shear fracture (plastic deformation), brittle fracture, and grain rotation. Figure 3-5a shows the first type of material removal, i.e., shear fracture. Due to the contact of tool and workpiece surface, big carbon grains have been sliced and partially removed by shear fracture. This might be caused by the plowing forces of the tool against the workpiece surface.

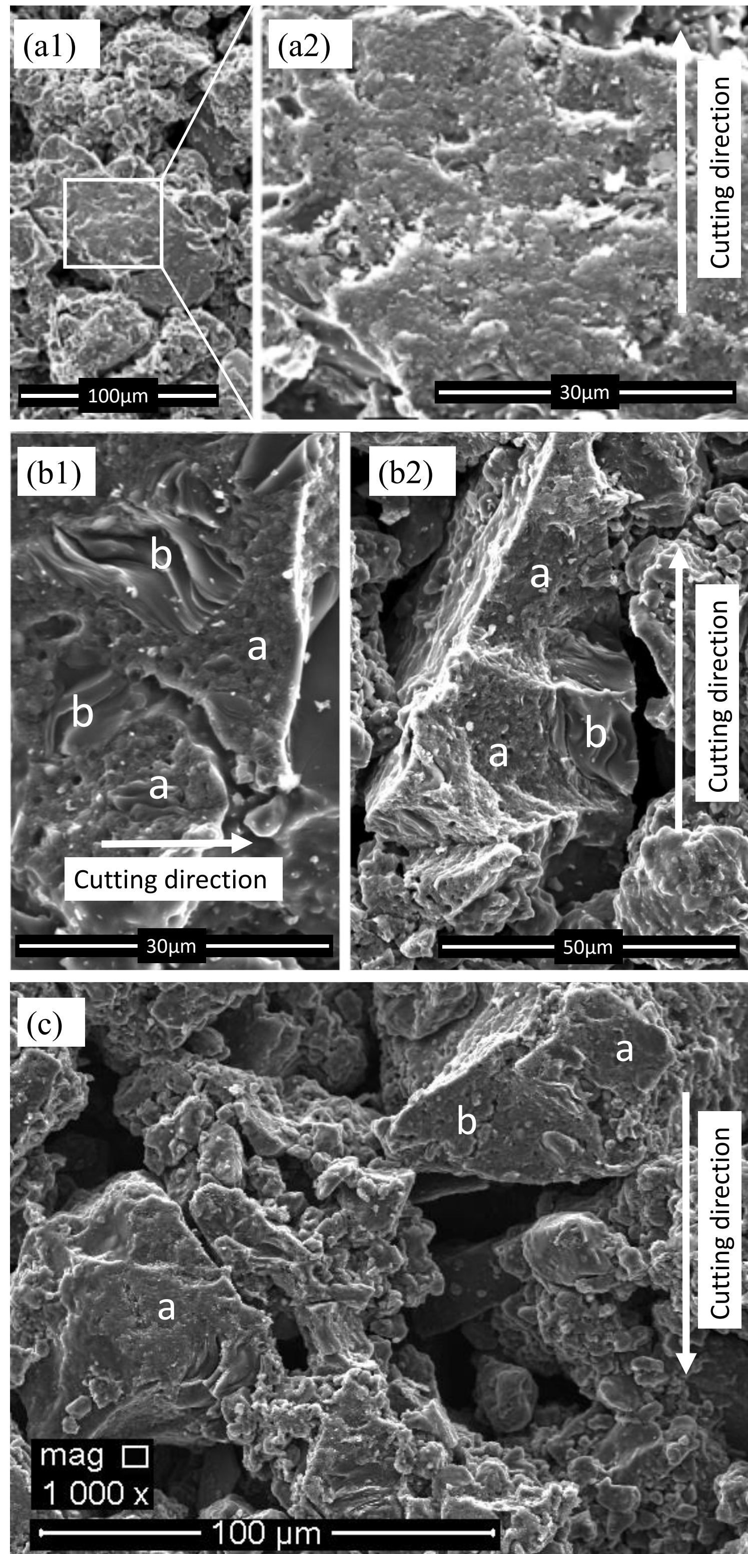

Figure 3-5: Three typical material removal mechanisms: ((a1) and (a2)) shear fracture, ((b1) and (b2)) brittle fracture, and (c) grain rotation.

Figure 3-5b gives an example of the second mechanism, i.e., brittle fracture. In Figure 3-5b, at the location indicated by 'a', the upper part of the grain aggregation was

removed due to brittle fracture along the boundary with other grains, without the appearance of plastic deformation. These phenomena took place when the bonding strength of the interface between carbon particles is less than the shear strength of the bulk of carbon grain, and brittle fracture is easy to occur along the grain boundaries by the micro impacts of the cutting tool. This kind of crack propagation mechanism in different directions leads to high surface roughness. Another type of brittle fracture occurs inside a single carbon grain bulk. As indicated by 'b' in Figure 3-5b, a part of carbon grain is separated by crack generation from the intergranular fracture, leaving curved fracture edges in the craters [92].

The third phenomenon observed is grain rotation. As shown in Figure 3-5c, three flat surface areas indicated by 'a' and 'b' are seen, which are likely to be cut through plastic deformation. Apparently, the flat 'b' is not in the same plane as the other two flat 'a'. This indicates that some of the carbon particles had been rotated due to the cutting force from the tool. The cutting force exceeded the bonding strength of the grains, leading to grain rotation along the grain boundaries during cutting. The schematic illustration of machining process involving these three mechanisms of material removal is shown in Figure 3-6.

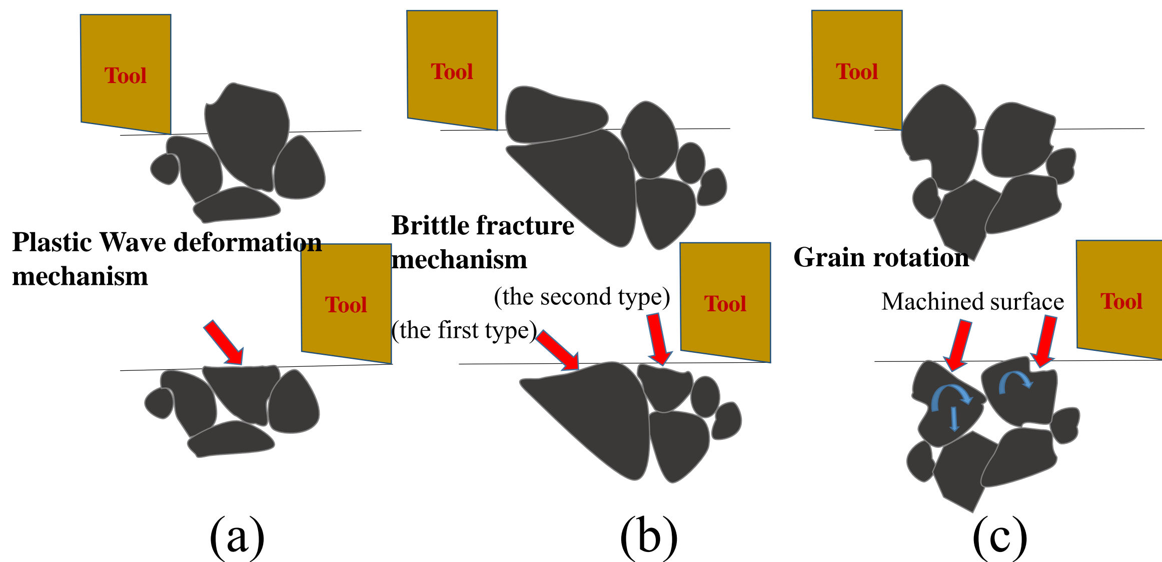

Figure 3-6: Schematic illustration of cutting mechanisms for porous carbon involving (a) shear fracture, (b) brittle fracture, and (c) grain rotation.

In addition to the above mentioned material removal mechanisms, it was found that a few particles had been pressed into the pores of the workpiece without any deformation or fracture, as shown in Figure 3-7a and Figure 3-7b. After collecting the chips and observing the chips by SEM, we found that the chip size increase with depth of cut. As shown in Figure 3-7c, the average radius of chips in machining condition of 0.2 mm depth of cut is less than 10 µm, this average size increased to 20 to 30 µm as the depth of cut reaches to 0.8 mm in Figure 3-7d.

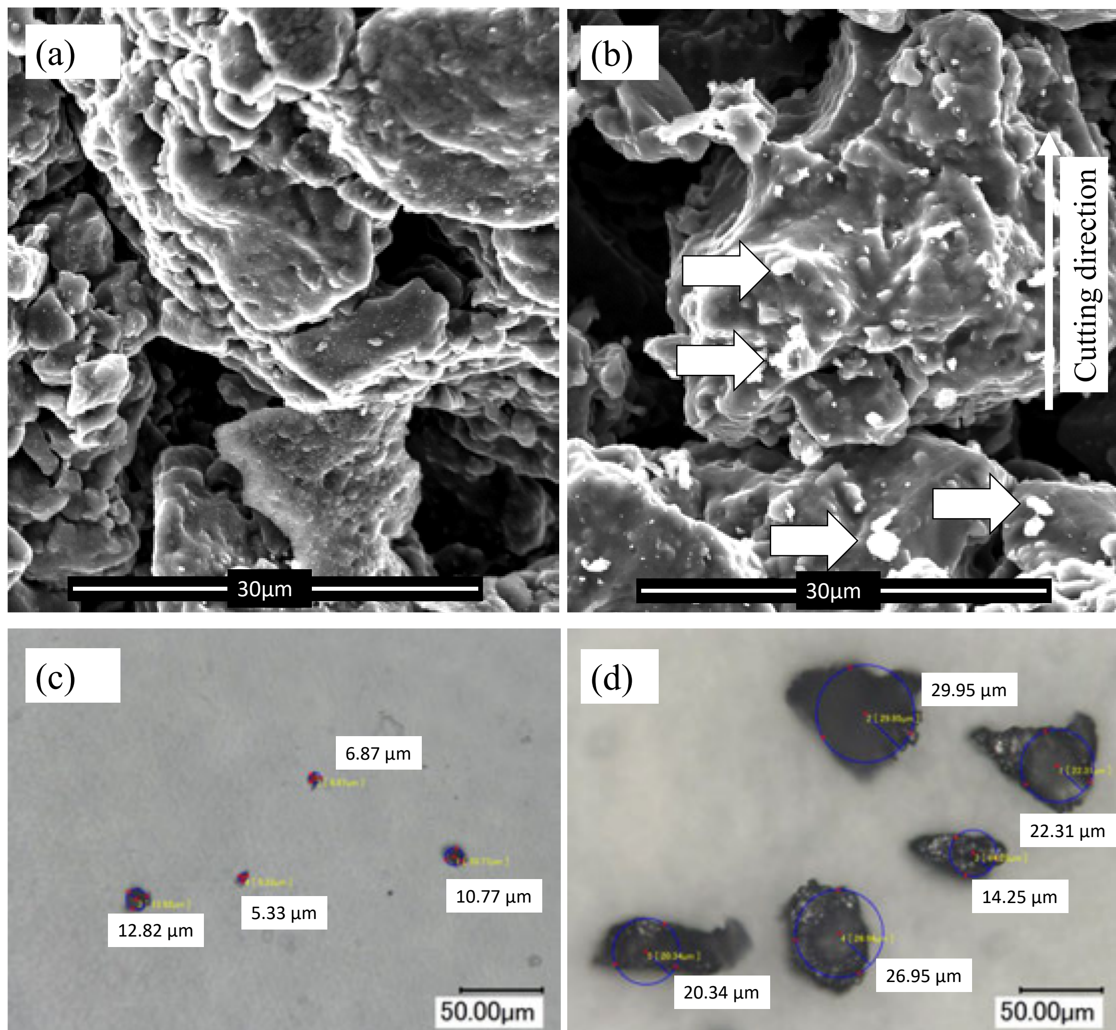

Figure 3-7: Observation results of chips: (a) and (b) show chips entering pores during cutting process; (c) and (d) show increase of chip size with depth of cut

3.2.2 Effects of machining parameters on cutting mechanisms

Next, the correlation between machining parameters and material removal mechanism was investigated. In order to study the impacts of feed rate and depth of cut, four individual

experimental tests were carried out at the same the cutting speed 60 m/min as shown in Table 3-4.

Table 3-4: Experimental conditions for individual effect of depth of cut and feed rate

No.	Depth of cut (mm)	Feed rate (mm/min)
1	0.2	25
2	0.2	100
3	0.8	25
4	0.8	100

FE-SEM observation of the machined surface indicated that in test 1, the majority of cut surface was formed by the first mechanism, i.e., shear fracture (plastic deformation), as shown in Figure 3-8a. In test 2, as shown in Figure 3-8b, both plastic deformation, the location indicated by '1', and brittle fracture (type a), the location indicated by '2', were observed. Shear fracture in this test was more significant with the generation of surface waviness. In test 3, shear fracture was more significant and the waviness is smaller compared with test 2, as shown in Figure 3-8c. In addition, brittle fracture type b was also observed in some part of the surface. As shown in Figure 3-8c, brittle fracture (type a) or crack propagation was the dominating mechanism in test 4. The aforementioned results indicate that increasing feed rate causes material removal mechanism to change from shear fracture to brittle fracture. At high feed rates, crack propagation becomes the dominating mechanism [93,94].The effect of depth of cut was similar to that of feed rate, nevertheless, the effect level was less than that of feed rate.

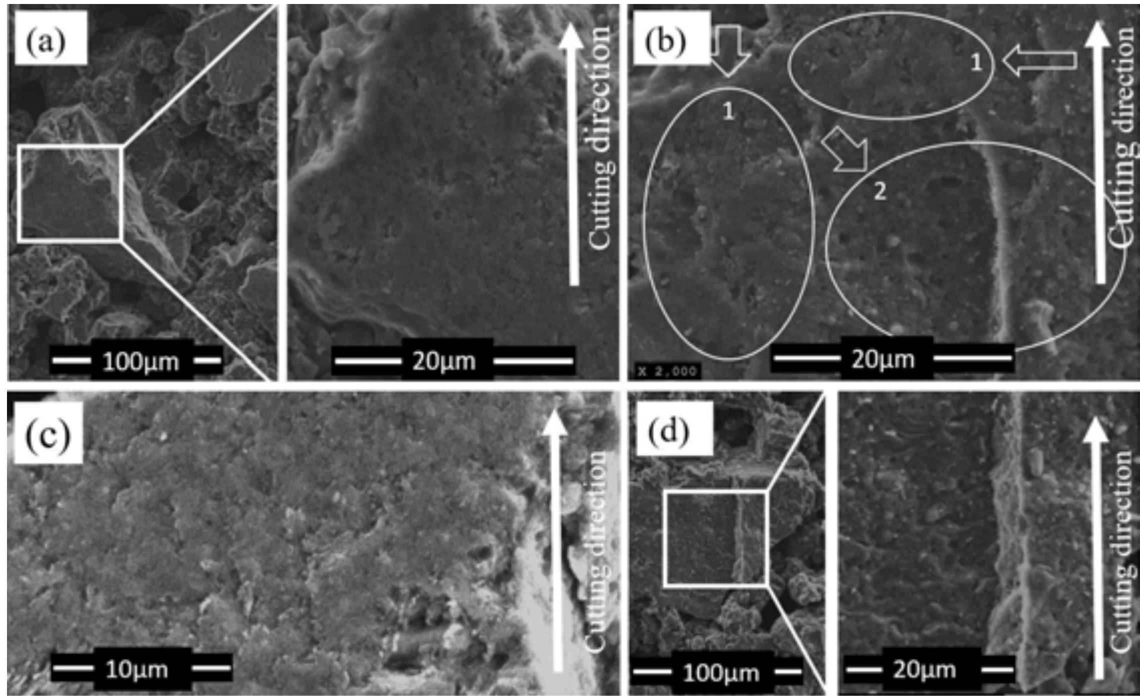

Figure 3-8: The effects of depth of cut and feed rate on cutting mechanisms (a) plastic deformation (b) wavy plastic deformation and brittle fracture, type a (c) wavy plastic deformation and brittle crack, type b (d) brittle fracture, type a

3.2.3 Effects of tool rake angle on cutting mechanisms

As known from previous researches on the diamond turning of typical hard brittle materials such as single crystalline silicon, tool rake angle significantly influences the material removal mechanism [30]. It has been well accepted that a negative rake angle is advantageous because it induces high compressive stress which prevents from the brittle fracture. On the other hand, in metal cutting, as rake angle decreases, the shear angle decreases and hence shear energy dissipation and cutting forces increase [64]. However, to date, there have been no reports on the effect of tool angle on cutting mechanisms of porous materials.

To investigate the effect rake angle on porous carbon cutting, experiments were performed under conditions shown in Table 3-3. Figure 3-9a is an FE-SEM image of the machined surface of test 1 (0° rake angle), where shear fracture is dominant. This kind of surface appearance was similar to those observed in test number 5 and 6 under conditions

shown in Table 3-2. The machined surface obtained using the tool with –15° rake angle in test 2 also presented the shear fracture mechanism, as shown in Figure 3-9b. However, there was a growth in cracks propagation through the machined surface. This phenomenon might be due to the fact that a negative angle provides greater compressive stresses, as well as a deeper affected zone below the surface, leading to more subsurface damage and surface cracks generation [95].

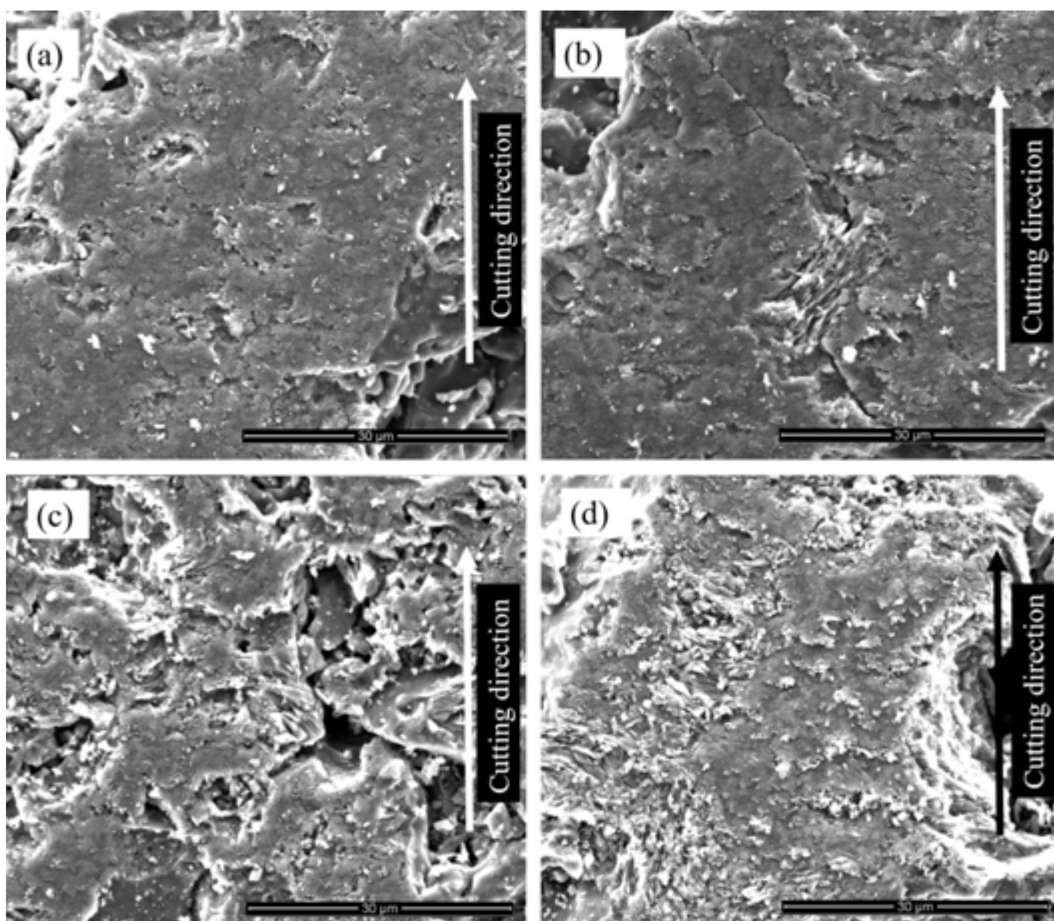

Figure 3-9: SEM images of surfaces machined at tool rake angles of (a) 0°, (b) -15°, (c) -30° and (d) -45°

Figure 3-9c and Figure 3-9d shows SEM images of surfaces machined under –30° and –45° rake angles. In addition to more significant surface cracks, the most part of the machined surface had been covered by small chips and particles. There might be two reasons for this phenomenon. Firstly, particles produced during the cutting process due to the plowing effect of the tool are pushed towards the workpiece surface under a highly negative rake angle and

accumulated on the surface. Secondly, microcracks propagation near the surface layer of the workpiece material also causes particle generation, which is easily attached to the surface.

The schematic illustration of particle generation during machining process under a negative rake angle is shown in Figure 3-10. As particle generation affects the surface integrity and surface cleanness, it is important to avoid using a highly negative rake angle when cutting porous carbon.

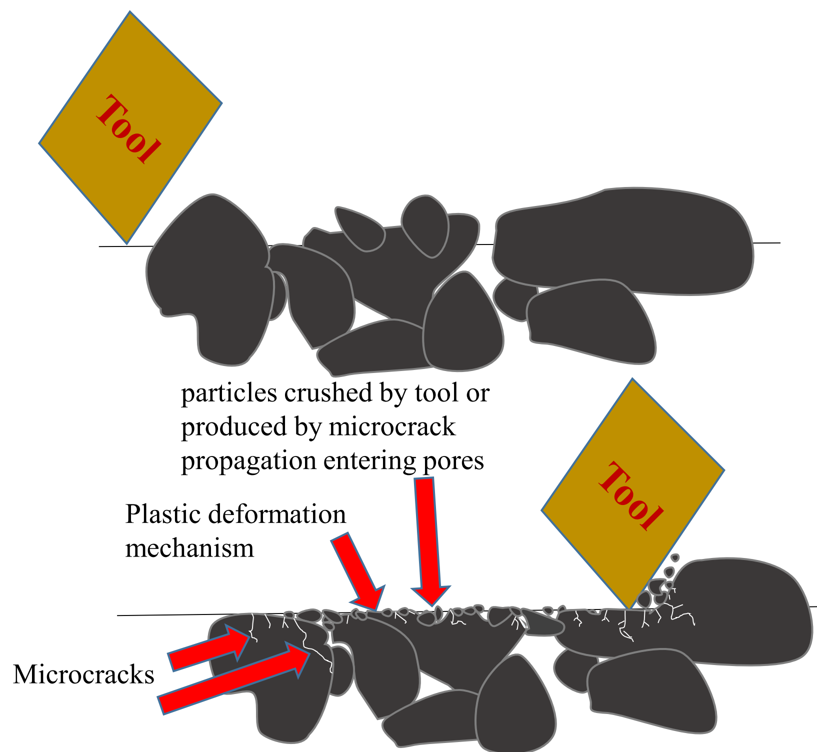

Figure 3-10: Schematic illustration of cutting mechanisms under a negative tool rake angle

3.2.4 Surface roughness analysis

Surface roughness was measured in both two-dimensional (2D) and three-dimensional (3D) forms. Figure 3-11a is a typical 2D surface profile of the machined surface, from which the algorithmic average surface roughness R_a was calculated. Figure 3-11b is a typical 3D profile of the machined surface roughness of porous carbon, from which the average arithmetical deviation of the area (S_a) was calculated by using the TalyMap software as [96,97].

$$S_a = \frac{1}{NM}\sum_{x=0}^{N-1}\sum_{y=0}^{M-1} Z_{xy} \tag{1}$$

In this research, S_a was used instead of R_a to achieve a total evaluation of surface characteristics. The experimental data were used to develop a relationship between the three machining parameters and S_a using regression methodology and ANOVA [98]. As shown in Figure 3-12, the ANOVA of data demonstrated that feed rate had a dominant effect on surface roughness (S_a) with 55.18%. The depth of cut took the second place with 38.27%. Nevertheless, the cutting speed had a negligible effect on S_a with just 6.54%. Although cutting speed is an important machining parameter and it has a significant influence on cutting temperature, this effect is strongly depended on workpiece properties. In porous carbon that is a high brittle material with a low fracture toughness, the temperature is not increased remarkably as cutting speed changes to influence the cutting process.

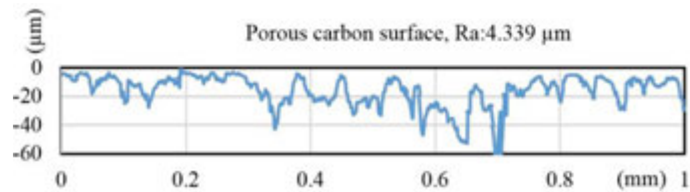

(a)

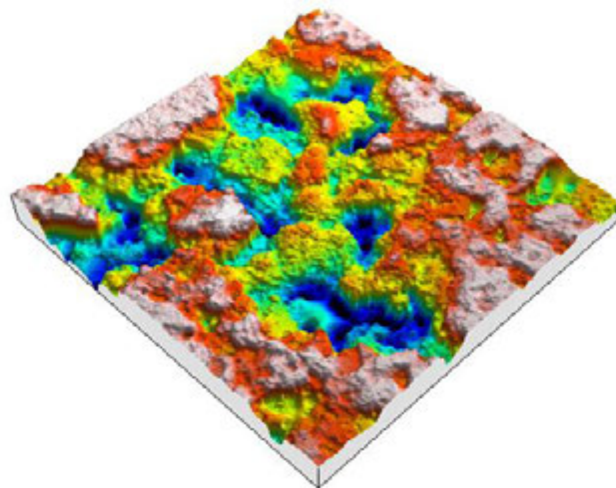

(b)

Figure 3-11: (a) 2D and (b) 3D surface topographies for calculating roughness parameters R_a and S_a

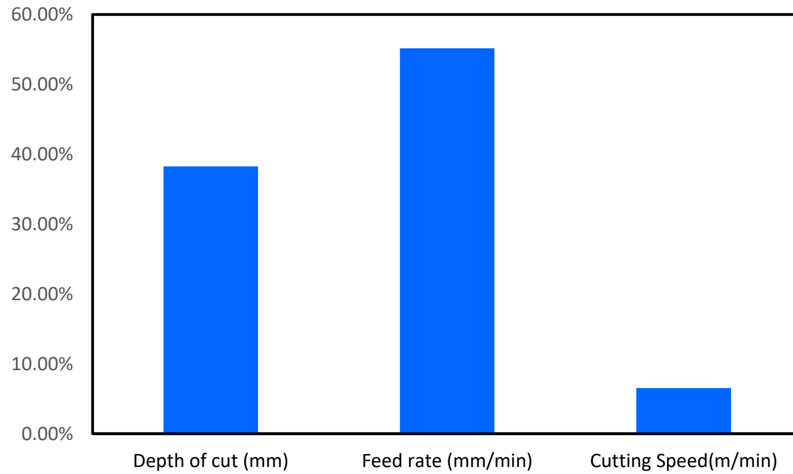

Figure 3-12: The influence of three independent parameters on surface roughness S_a

The pairwise effect of feed rate and depth of cut on surface roughness is shown in Figure 3-13. The points shown by four arrows are the tests performed in high cutting speed 120 m/min. By and large, increasing the feed rate causes increase in surface roughness, while there is no meaningful relationship between the depth of cut and surface roughness in Figure 3-13.

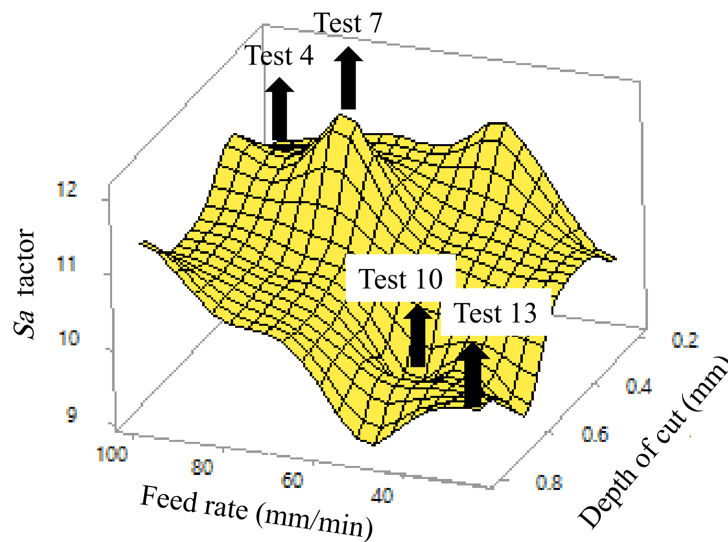

Figure 3-13: Effects of feed rate and depth of cut on surface roughness S_a

In order to study the impacts of the depth of cut, eight cutting tests were carried out at the same cutting speed (60 m/min) and feed rate (50 mm/min) but the different depth of cut from 0.1 mm to 0.8 mm. As presented in Figure 3-14a, by increasing depth of cut, surface roughness factor fluctuated between 6.5 µm and 10 µm, and the trend line (dashed line), which

is obtained using linear regression analysis method, demonstrates a slight increase. When the depth of cutting increases mechanism of removal will change towards more brittle fracture leaving more curved fracture edges in the craters. This slight increase can be seen in Figure 3-8 in which roughness of surface increases in Figure 3-8c and Figure 3-8d (0.8 mm depth of cut) compared to Figure 3-8a and Figure 3-8b (0.2 mm depth of cut) respectively. However, the effect of feed rate was more obvious in comparison with the depth of cut as already explained in Section 3.2.2.

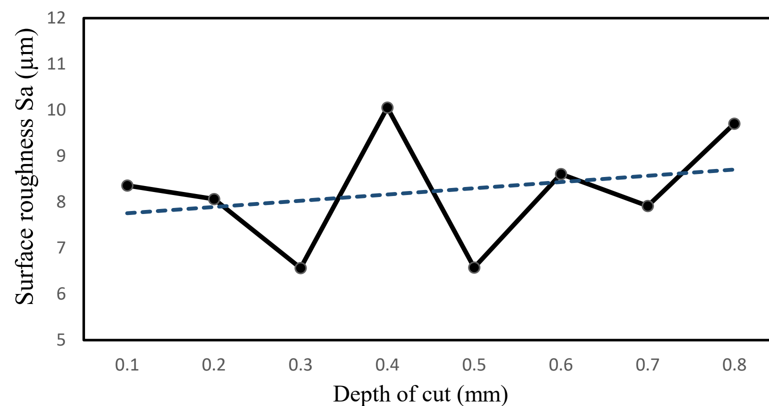

(a)

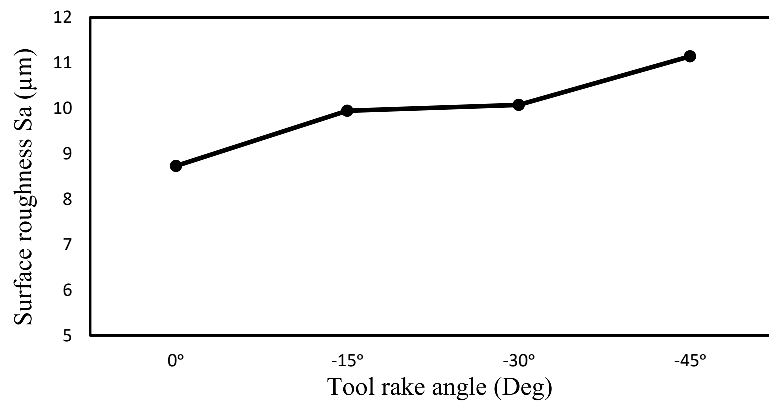

(b)

Figure 3-14: Effects of (a) depth of cut and (b) tool rake angle on the surface roughness S_a

In addition, Figure 3-14b shows effects of tool rake angle on surface roughness. There is a meaningful increase in roughness by decreasing tool rake angle. This result demonstrated again that a negative tool rake angle is disadvantageous for cutting porous carbon.

3.2.5 *Bearing area curve*

Considering the application of porous carbon in air bearing, the bearing area curve (Abbot Firestone Curve) is an important indicator of surface quality. The material ratio is defined as the ratio of the intersecting area of a plane (i.e., parallel to the mean plane) passing through the surface at a given height to the cross-sectional area of the evaluation region [99]. Bearing area curve is established by evaluating material ratio at various levels from the highest peak to the lowest valley. There are two important parameters to characterize the bearing area curve: core roughness depth S_k and peak height above the core roughness, S_{pk} (alternatively, valley depth below the core roughness S_{vk}), as shown in Figure 3-15a and Figure 3-15b.

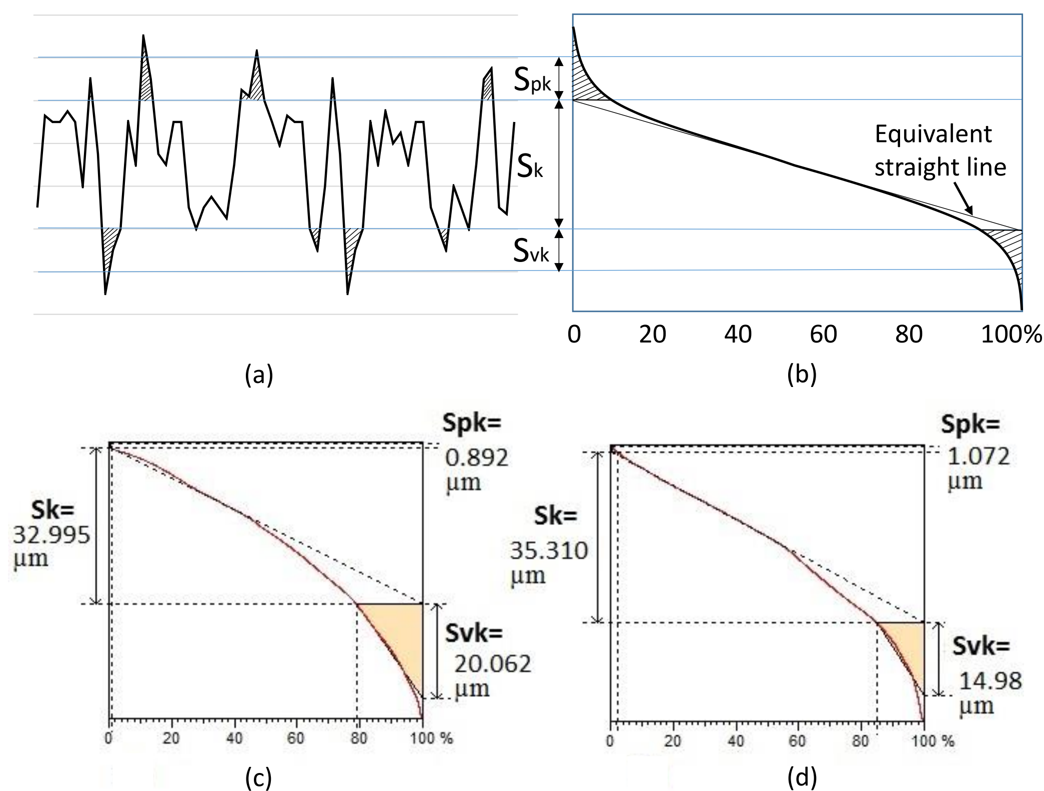

Figure 3-15: (a) and (b) show definition of parameters S_{pk}, S_k and S_{vk} in a bearing area curve; (c) and (d) are bearing ratio curves of test 1 and test 4, respectively

Analysis of S_k showed that it followed the same trend as that of S_a as shown in Figure 3-13. That is to say, feed rate and depth of cut are the dominate parameters on S_k while cutting speed did not have an impact on S_k. In order to consider the effect of feed rate on S_k

factor, we compared the bearing ratio curves of two experiments at feed rates of 25 and 100 mm/min respectively, corresponding to test 1 and 4, 5 and 8, 9 and 12 in Table 3-2. In each cutting test, 8 areas of the sample were evaluated by white light interferometer and the Talymap software. Figure 3-15c and Figure 3-15d show the results of tests 1 and 4, respectively.

It is clear that the test at higher feed rate (Figure 3-15d) presented a larger S_k than that at a lower feed rate (Figure 3-15c). Therefore, increasing feed rate will cause both surface roughness (S_a) and core roughness (S_k) to rise. Although increasing S_a is not desired, increasing S_k is advantageous because it will improve the capability of carrying the load after the initial running-in period for air bearings [100]. The effect of depth of cut on S_k indicated the same trend.

Another important factor that should be taken to account is S_{pk} which have strong effects on the ability of a surface to resist wear. In the air bearing application, a small S_{pk} leads to increasing wear resist and the life of part. In this study, the results showed that the S_{pk} in all tests is almost less than 1 µm, far smaller than S_k, as shown in Figure 3-15c and Figure 3-15d. This shows that despite of different cutting conditions, S_{pk} is negligibly small. This fact demonstrated again that it is advantageous for using a diamond turned porous carbon surface in air bearing applications [100].

The wear resistance of a surface can also be characterized by skewness distribution graph. Figure 3-16a shows two typical surface profiles and the corresponding skewness distribution. It is known that for a porous carbon surface as porous media air bearings, a negative skew is beneficial [97]. In the present study, all diamond turned porous carbon surfaces showed negative skew curves. Figure 3-16b illustrates an example of skewness distribution graph in test 16 of Table 3-2.

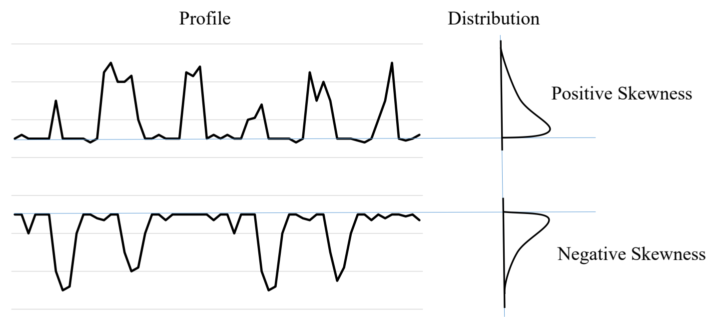

(a)

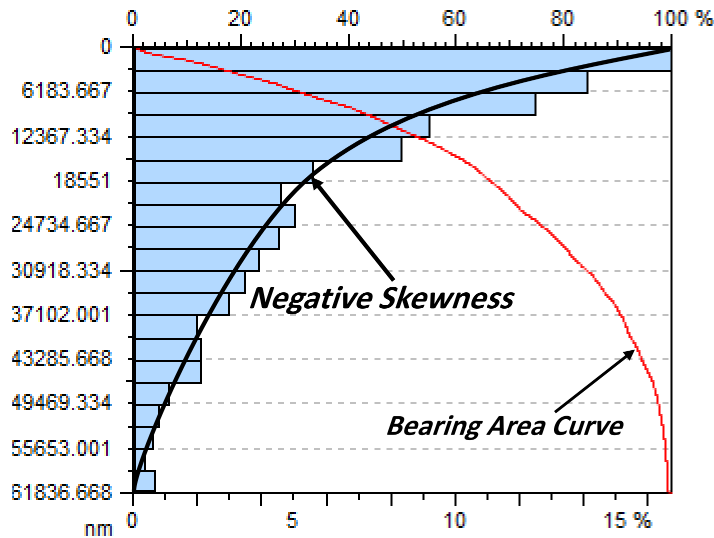

(b)

Figure 3-16: (a) Definition of skewness distribution curve; (b) skewness distribution graph for porous carbon diamond turned at conditions: *f* (100 mm/min), *v* (30 m/min) and *a* (0.8 mm)

3.2.6 Surface porosity

The surface porosity of porous carbon plays an essential role in its application as air bearing. To evaluate surface porosity, the ImageJ software was used to analyze SEM images of the machined surfaces. An example of SEM image is shown in Figure 3-17a. Then these images were processed to calculate the area ratio of surface pores. Figure 3-17b shows the processed results by the ImageJ software.

ImageJ counts and measures objects in binary or thresholded images (Threshold or Color Threshold command). Analysis is performed on the existing area selection or on the entire image if no selection is present. It works by scanning the image until it finds the edge of

an object. It then outlines the object, measures it, fills it to make it invisible, then resumes scanning until it reaches the end of the image or selection.

The particle count, total particle area, average particle size, area fraction and the mean of all parameters will be displayed in a separate summary table. For each column in the results table, calculates and displays the mean, standard deviation, minimum and maximum of the values in that column. The sum of all particle areas (uncut areas) divided by the total area will be porosity ratio.

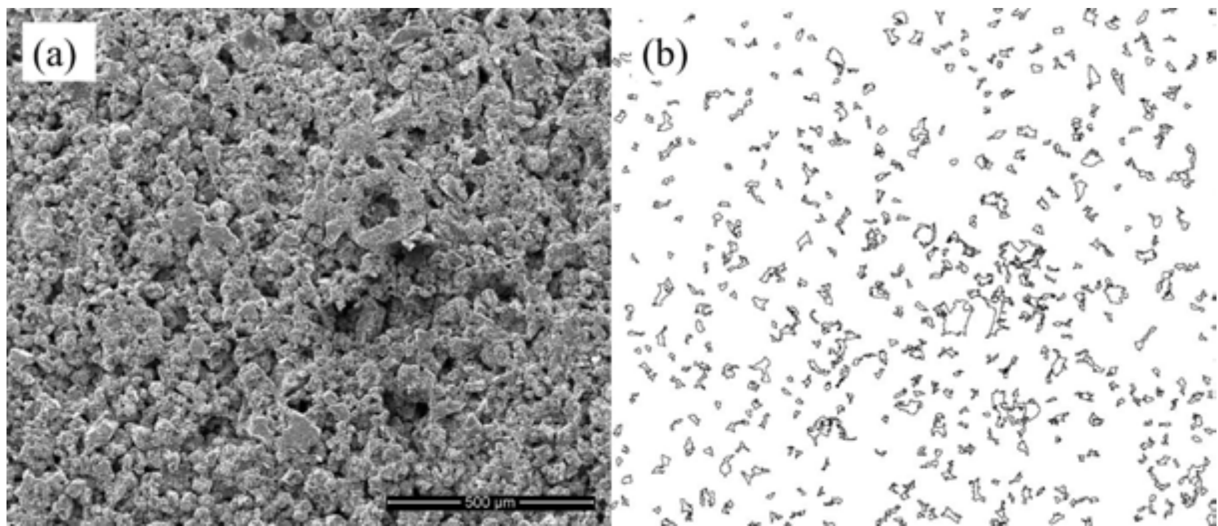

Figure 3-17: (a) SEM image of a diamond turned surface; (b) Image-processed results for calculating surface porosity

Figure 3-18a illustrates the effects of depth of cut, feed rate and cutting speed on surface porosity. Figure 3-18b presents the effect of tool rake angle on porosity. In both cases, there is no strong dependence of porosity on the machining parameters and tool rake angle. All machined samples showed an average of about 25% decrease in porosity after machining, which is acceptable for air bearing applications [101]. It is worth nothing that pressed particles into pores and rotating grains towards pores, which causes pores to be closed during the cutting process, are the main reasons in decreasing porosity percentage.

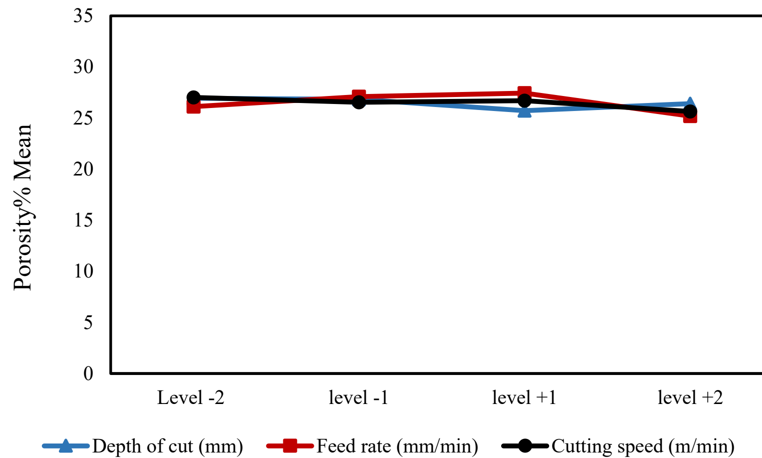

(a)

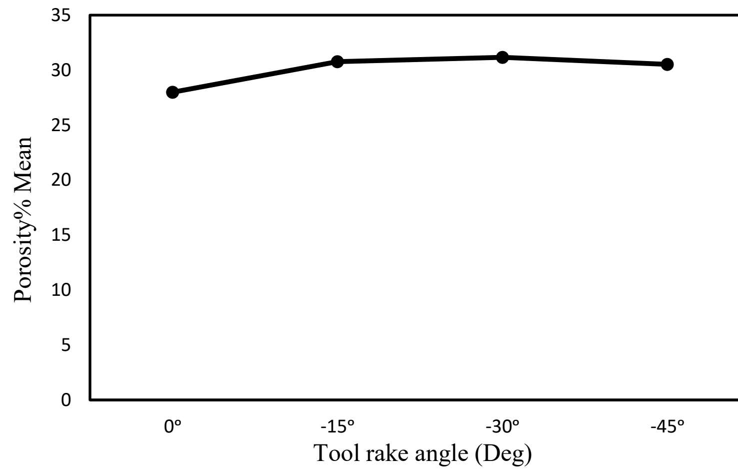

(b)

Figure 3-18: Effects of (a) three machining parameters with their levels (Table 3-1) and (b) tool rake angle on surface porosity

3.3 Conclusions

The fundamental material removal phenomena in diamond turning of porous carbon were investigated experimentally. The following conclusions were drawn.

(1) Three major mechanisms were involved in the material removal, namely, shear fracture, brittle fracture and grain rotation. The brittle fractures can be further divided into two types: grain boundary fractures and intergranular fractures.

(2) Among the three independent cutting parameters, the feed rate was the most important factor with 55.18% affecting the surface formation and surface roughness, and the

second one was the depth of cut with 38.27%; whereas cutting speed has no significant impact with just 6.54%.

(3) Tool rake angle influenced both material removal behavior and surface roughness (It has increased surface roughness from 8.73 to 11.14 μm). A negative tool rake angle was disadvantageous for machining porous carbon.

(4) The diamond-turned porous carbon surface has an extremely small peak height, a high core roughness, and a negative skewness distribution, which are advantageous for air bearing applications.

(5) The diamond-turned porous carbon surface has an average porosity of 26.5%, about 25% decrease in porosity compared with that before machining.

The results from the present study preliminarily demonstrated the possibility of fabricating high-precision air bearings of porous carbon directly by diamond turning.

CHAPTER 4

Machining of porous silicon

Chapter 4 : Machining of porous silicon

4.1 Material and methods

4.1.1 Machining apparatus

Face turning was performed using a three-axis control ultraprecision machine, NACHI ASP-15 (NACHI-FUJIKOSHI CORP). A photograph of the main section of the machine is shown in Figure 4-1. The machine has an ultraprecision air-bearing spindle, two perpendicular linear tables supported by high-stiffness hydrostatic bearings and driven by servomotors via hydrostatic screws with negligible mechanical friction, and a rotary table supported by hydrostatic bearings and driven by a friction drive in order to prevent from backlash movements. Laser hologram scales are used to accurately position all of these tables. Under precise numerical control, the linear tables can be moved at 1 nm per step and the rotary table can be rotated with an angular resolution of 0.00001°.

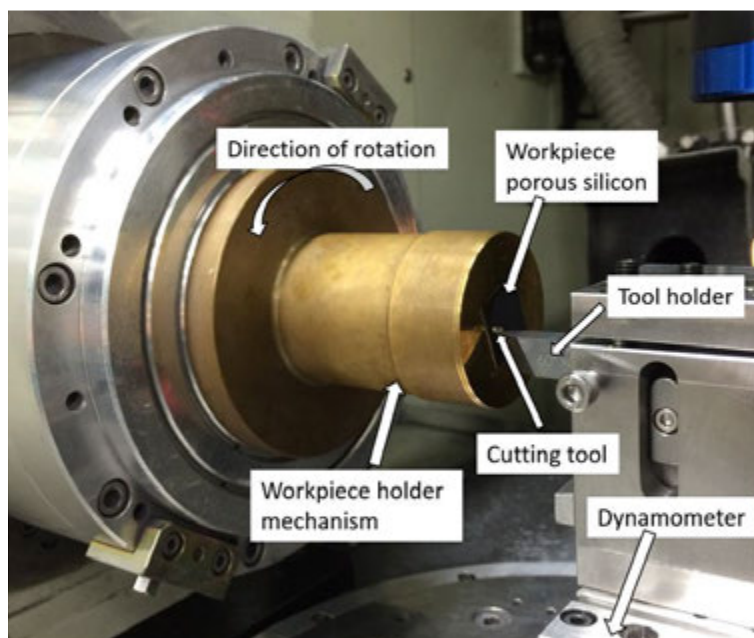

Figure 4-1: Photograph of experimental setup

4.1.2 Diamond tool

A commercially available single-crystal diamond tool with a nose radius of 0.5 mm, rake and clearance angles of 0° and 6°, respectively, as shown in Figure 4-2, was used in experiments.

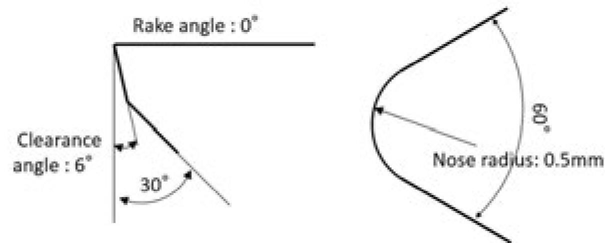

Figure 4-2: Tool geometry

Figure 4-3 shows a schematic model for diamond turning with a round-nosed tool, where the maximum undeformed chip thickness h_{max} is an important parameter to evaluate the cutting performance. h_{max} can be calculated from the tool nose radius R, depth of cut a and tool feed rate f, using the following equation when $f < \sqrt{2Ra - a^2}$ [102,103].

$$h_{max} = R - \sqrt{R^2 + f^2 - 2f\sqrt{2Ra - a^2}} \quad (2)$$

When $f \geq \sqrt{2Ra - a^2}$, however, h_{max} is equal to the depth of cut a. In this study, machining parameters were selected to make undeformed chip thickness range from ductile mode to brittle mode cutting for single crystal silicon.

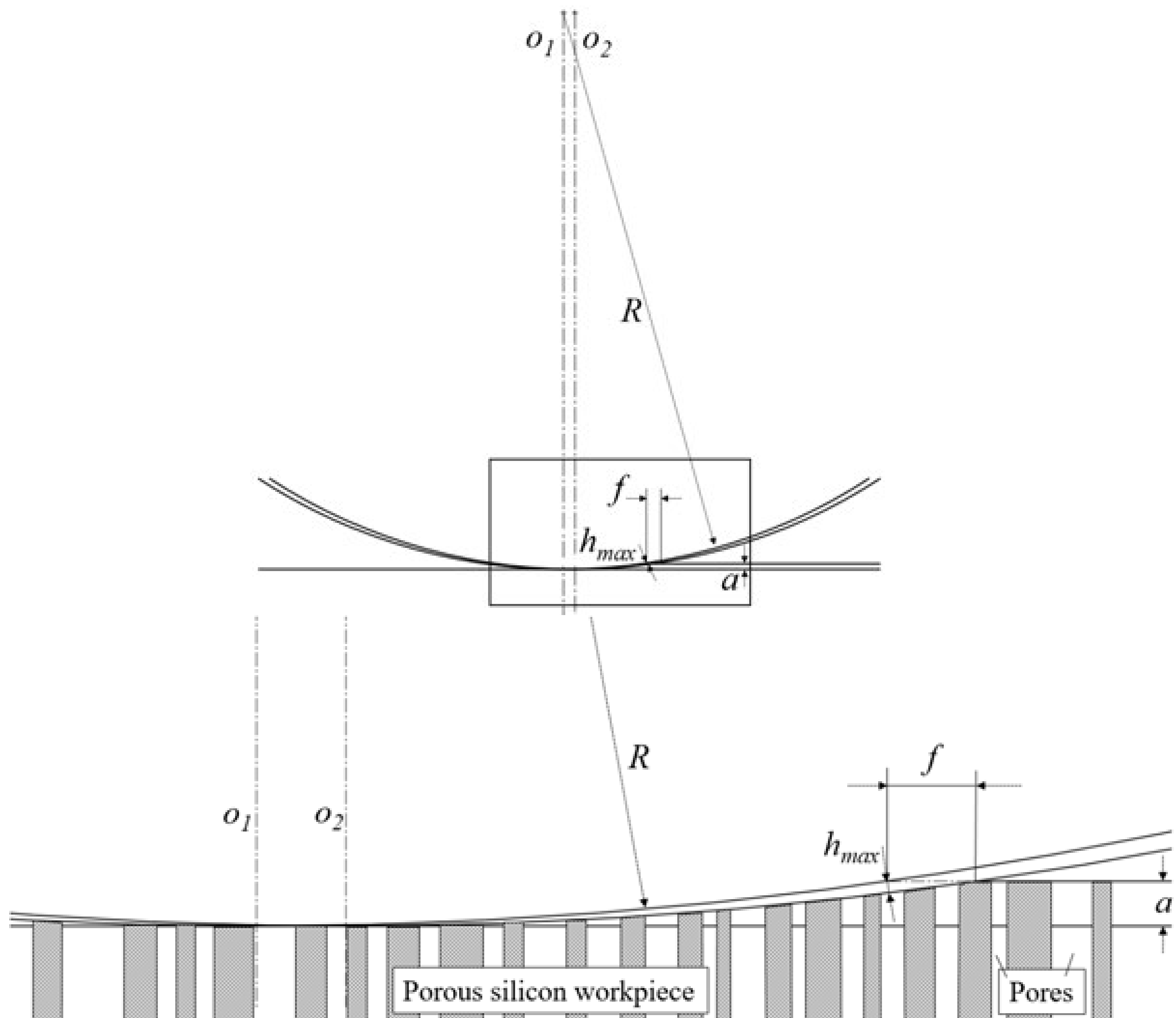

Figure 4-3: Cutting model for porous silicon using a round-nosed tool

4.1.3 Workpiece materials

Two types of porous workpieces were used. One type had a thickness of 330 μm with blind pores and the other had a thickness of 260 μm with through pores. The workpiece size for both types is 20.0 mm×20.0 mm with a porous zone of 16 mm in diameter and average pore size of 2.7 μm. Figure 4-4 shows a photograph of a sample and an SEM micrograph of its surface. These porous silicon samples had been fabricated by anodic oxidation of single-crystal silicon (100) wafers. In addition to porous silicon samples, single-crystal silicon wafers (100) without pores were also machined in this study for comparison.

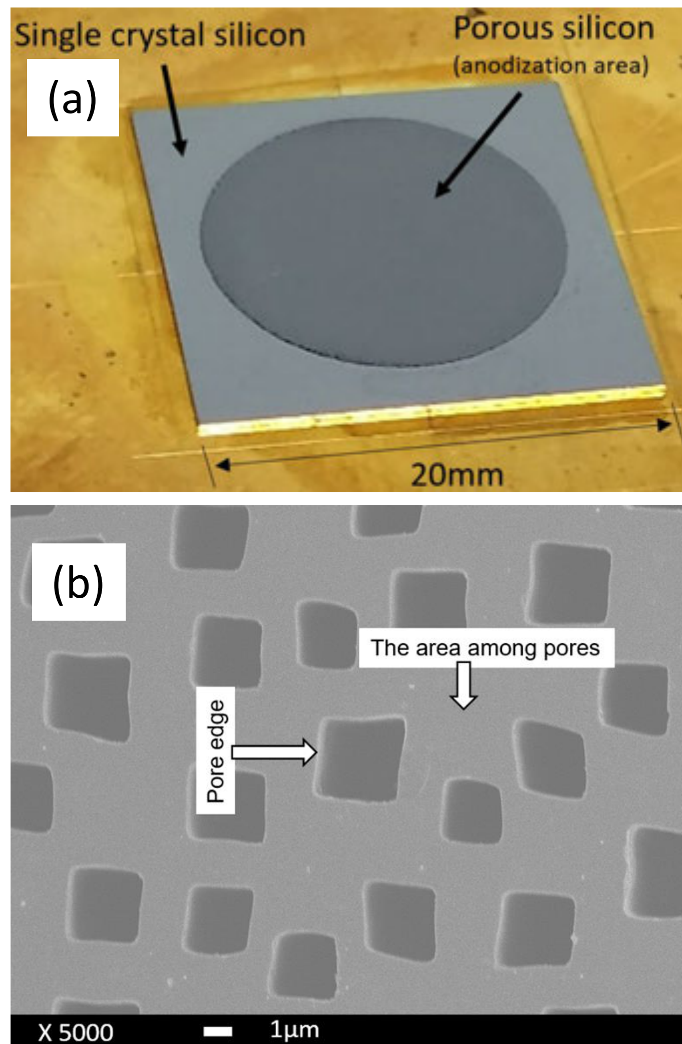

Figure 4-4: Porous silicon workpiece (a) overview photograph (b) SEM micrograph of anodization area

4.1.4 Machining conditions

Three circular areas, 1.5 mm in width for each, were cut on each sample at feed rates of 0.2, 2.0 and 10.0 μm/rev, as schematically shown in Figure 4-5. Spindle rotation rate during cutting was fixed to 1500 rpm, consequently the cutting speed changed from 0.27 to 0.90 m/s. This range of cutting speed change is insufficient to cause a remarkable difference in cutting behavior in terms of cutting forces and heat-induced material softening [24]. The depth of cut was ranged from 1 to 5 μm, and the actual depth of cut was measured from the uncut shoulder.

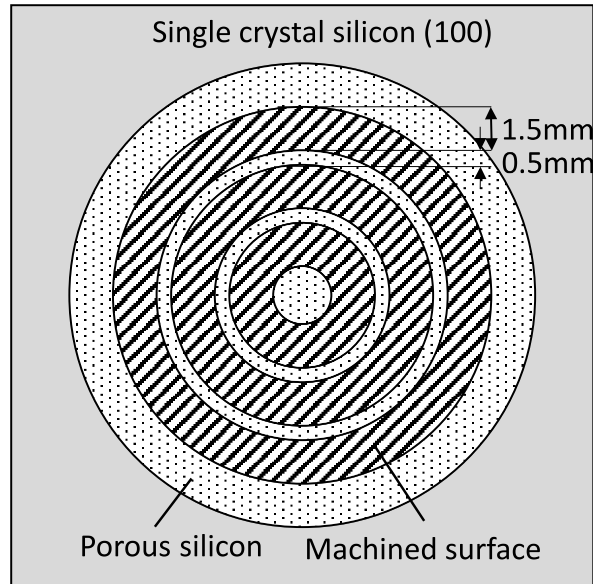

Figure 4-5: Schematic illustration of machined areas on workpiece

When cutting a porous material, cutting chips are easy to enter the pores, which might affect the surface function of the workpiece. In this work, to prevent chips from entering pores, wax was used in the experiments as pore infiltrant. The wax had a softening point of 76 ºC and adhesion strength of 40 kg/cm^2. It was melted and then coated on the porous silicon surface (the through-hole type) so that it penetrated and filled completely the pores, as shown in Figure 4-6.

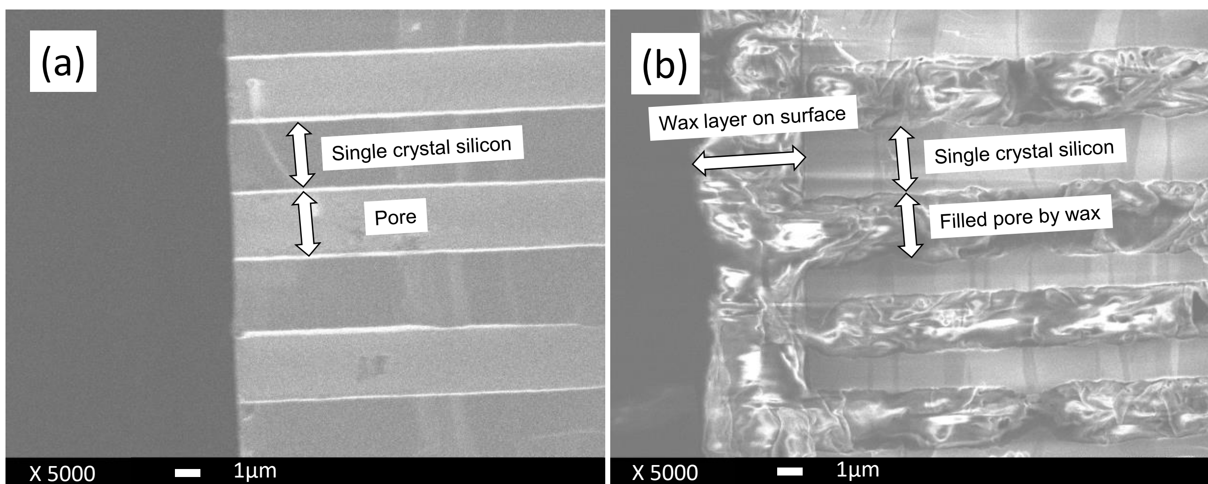

Figure 4-6: SEM micrographs of porous silicon cross sections showing (a) before (b) after wax coating

After machining, the wax was removed using ethanol and acetone compounds. Prior to machining, the sample was bonded onto a copper blank using a heat-softened wax and then vacuum chucked onto an air-bearing spindle.

4.1.5 Measurement apparatus

In order to evaluate the machined surface quality, a white light interferometer was used and the surface profile was analyzed by the Talymap software (Taylor Hobson Ltd.). A scanning electron microscope (SEM, Model Inspect S50) and a field-emission scanning electron microscope (FE-SEM, Model JSM-7600F, JEOL) were used to observe the sample surfaces and tool wear. A Laser micro-Raman spectroscope, NRS-2100 (JASCO Corp., Japan), was used to characterize the subsurface damage. In addition, a piezoelectric dynamometer (Kistler 9256C2) was mounted below the tool to measure micro-cutting forces during the cutting tests.

4.1.6 Finite element simulation

To assist understanding the material removal mechanism of porous silicon, the stress distribution in the cutting area was simulated by using AdvantEdge, a finite element (FE) machining simulation program produced by Third Wave Systems USA. Two-dimensional simulations of orthogonal cutting were performed, thus, the undeformed chip thickness was the same as the depth of cut. The tool rake angle, relief angle and cutting speed used in the simulations were the same as those used in the experiments. The pressure-sensitive Drucker-Prager constitutive model [104–106] was used to establish the material property model for silicon. The pertinent workpiece material properties are given in Table 4-1. In order to minimize boundary effects, the workpiece height should be at least five times of the depth of

cut according to AdvantEdge guideline. In this work it is 1000 times bigger than depth of cut. In addition, the length of cut should be 20 times the depth of cut.

The workpieces were constrained from displacement in the X and Y axis in the bottom plane. The right and top-most sides of the tool are fixed in the X and Y directions. The minimum element size for workpiece meshing is 0.0001 mm with 600000 maximum number of nodes, in which mesh refinement and coarsening factors are 2 and 6 respectively.

Table 4-1: FEM modeling parameters of workpiece

Parameters	**Value**
Pressure-sensitivity coefficient	0.375
Material constant (GPa)	8.125
Hardness (GPa)	13.0
Tensile yield stress (GPa)	5.9
Young's modulus (GPa)	165
Thermal Conductivity (W/m ^{o} C)	149
Heat Capacity, J/kg ^{o}C	712
Density, kg/m^3	2330

4.2 Results and discussion

4.2.1 Microfracture phenomena

Figure 4-7a and b show SEM images of the machined surface of bulk single-crystal silicon without pores. As undeformed chip thickness was increased, the cutting mode transited from ductile to brittle. Microfractures began to form at an undeformed chip thickness between 248 nm to 532 nm, and the density of the microcracks increased with undeformed chip thickness. In contrast, Figure 4-7a and d show SEM images for machined porous silicon. In this case, brittle mode machining is significant around pores while ductile mode machining

was only observed in the areas among the pores. The size of brittle fractures increased with the increase of undeformed chip thickness.

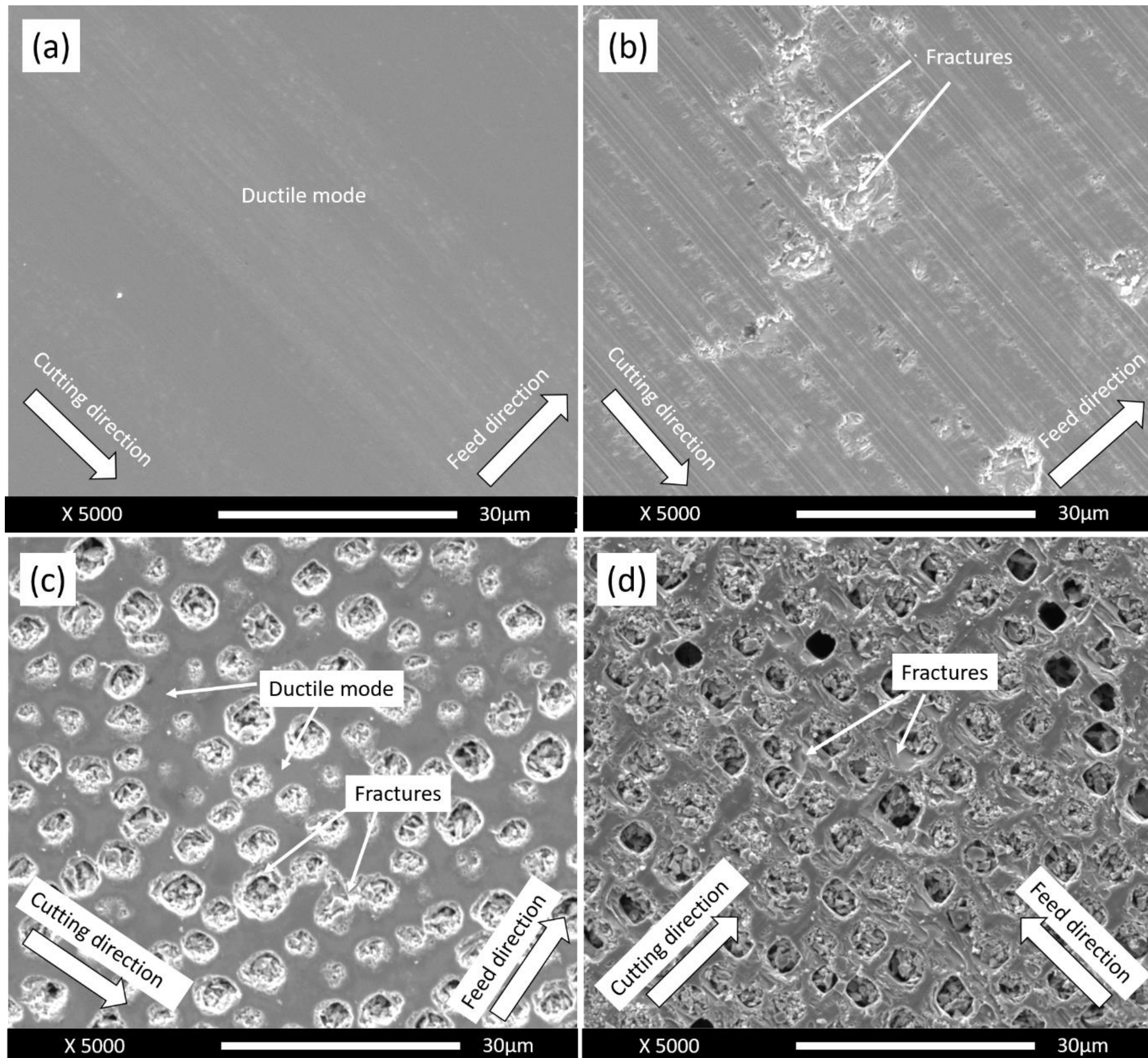

Figure 4-7: SEM micrographs of machined surfaces of single-crystal silicon without pores and porous silicon at different undeformed chip thicknesses: ((a) and (c)) h_{max} =12nm, ((b) and (d)) h_{max} =794nm.

Figure 4-8 compares the surfaces machined at undeformed chip thickness of h_{max}=122 and h_{max}=532nm at a higher magnification. At h_{max} =122 nm, brittle fracture is mostly observed at pore edges, while by increasing h_{max} to 523 nm, the areas among pores are also fractured.

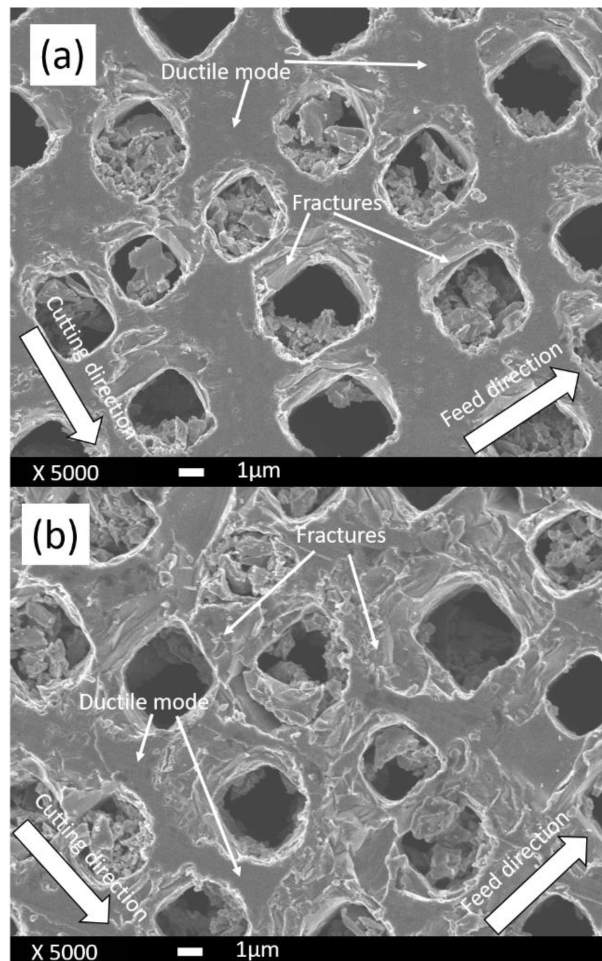

Figure 4-8: Magnified SEM micrographs of machined surface of porous silicon at different undeformed chip thicknesses (a) h_{max}=122 nm (b) h_{max}=532 nm

It is well-known that there is a brittle-ductile transition in chip formation during the cutting of brittle materials when the undeformed chip thickness is reduced [24,34,102,107,108]. When undeformed chip thickness is less than the critical undeformed chip thickness, no cracks are generated. When the undeformed chip thickness is larger than the critical value, however, microfractures are generated and the density of microfractures increases with the undeformed chip thickness.

Ductile mode cutting of a brittle material is based on hydrostatic pressure (compressive stress) which determines the extent of plastic deformation prior to fracture [28,29]. This stress state exists in the vicinity of cutting edge and is dependent on tool rake angle and undeformed chip thickness. When undeformed chip thickness becomes small enough, the entire cutting

region will be under the high compressive stress state, such a high hydrostatic pressure becomes a prerequisite for machining brittle materials by plastic flow at room temperature [30]. In addition, high hydrostatic pressure can prevent microcrack propagation by the closure of cracks [31].

Nevertheless, in a porous material, this kind of high hydrostatic pressure state cannot be maintained around a pore. This causes microcracks to propagate, and as soon as these cracks reach the pore walls, a part of silicon will be separated from the bulk, leaving fractures. To further investigate the phenomenon of material removal mechanism, the edges of a pore were divided into four groups according to the direction of cutting with respect to the orientation of a rectangular pore, as schematically shown in Figure 4-9.

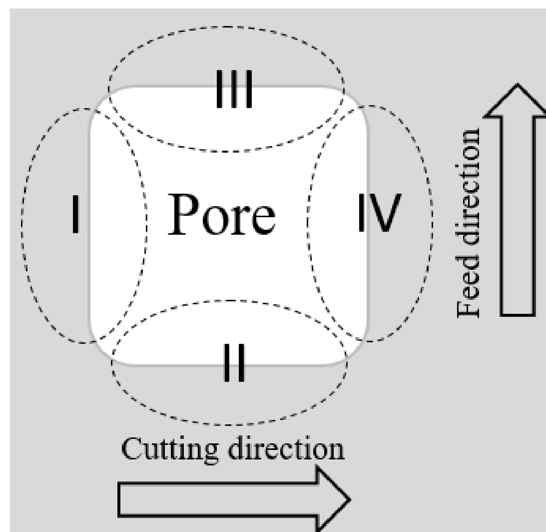

Figure 4-9: Schematic illustrations of four areas of pore edges

As shown in Figure 4-10a, the area indicated by “I” was cut in a brittle mode, while the area indicated by “IV” was cut in a ductile mode. Both “II” and “III” areas were also cut in a brittle mode but less severely in comparison with the “I” area. The size of brittle fracture decreases with tool feed rate (Figure 4-10b). Figure 4-10c and d show pores having oblique edges to the cutting direction.

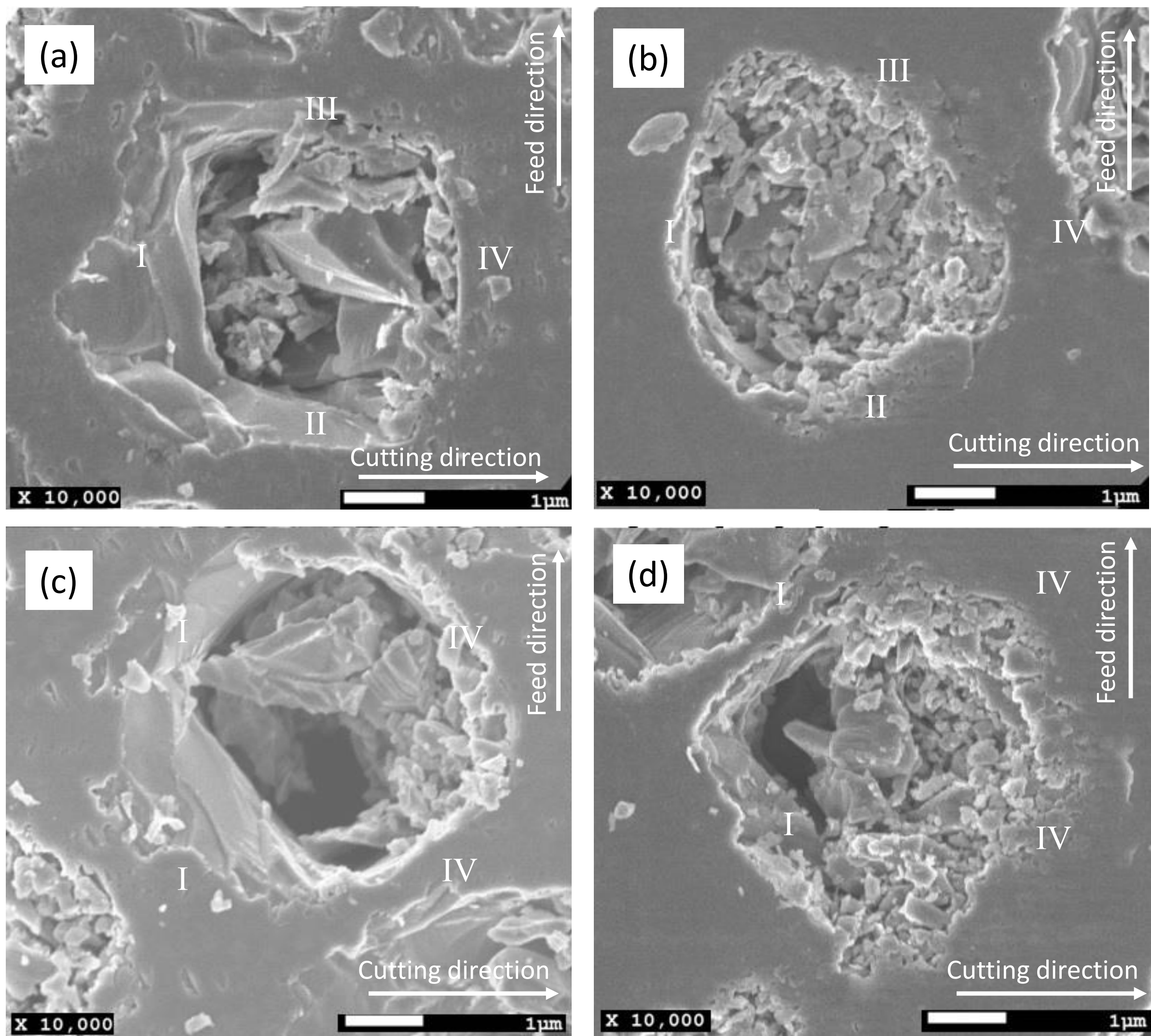

Figure 4-10: Material removal behavior around pores: (a) h_{max}=174 nm (f=2.0 µm/rev, a=2.0 µm); (b) h_{max} =17 nm (f=0.2 µm/rev, a=2.0 µm); (c) h_{max} =122 nm (f=2.0 µm/rev, a=1.0 µm); (d) h_{max} =12.6 nm (f=0.2 µm/rev, a=1.0 µm)

As shown in Figure 4-11a, the area “I” is significantly influenced by the high-pressure induced by cutting edge, providing a condition for microcracks to propagate severely to reach the wall of pore because there is no resistance in the pore. When tool passes the pore, some chips are carried away by the rake face of the tool and some other chips would be pressed into the pore (Figure 4-11b). As the tool reaches the “IV” area, as shown in Figure 4-11c, the mechanism of cutting would be like that of a non-porous bulk material except that there is an impact from the tool to the pore edge.

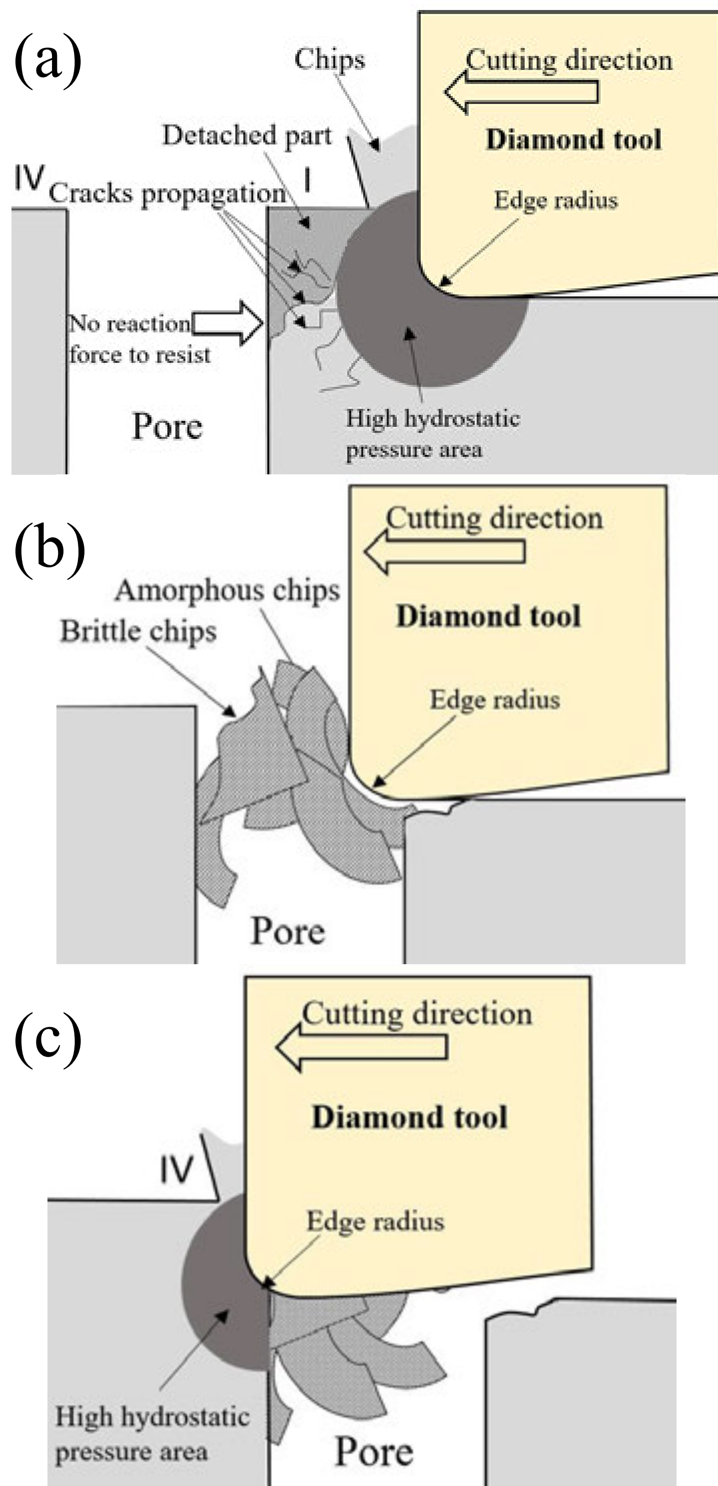

Figure 4-11: Schematic illustrations of cutting mechanisms near a pore (a) I area (b) pore area (c) IV area

The cutting mechanisms of the "II" and "III" areas involve brittle fractures too, but the size of brittle fractures depends on the relative position between the tool and the pore. When the tool feeds toward an edge of a pore, the tool feed-induced force has a significant side force component, as shown in Figure 4-12a, which will lead to large brittle fractures around the pore

edge. When the tool feeds over a pore, however, the side force component is vanishingly small, as shown in Figure 4-12b, thus brittle fracture is greatly suppressed compared to that in Figure 4-12a. From this meaning, it is presumable that using a tool with a larger nose radius can reduce the side force component.

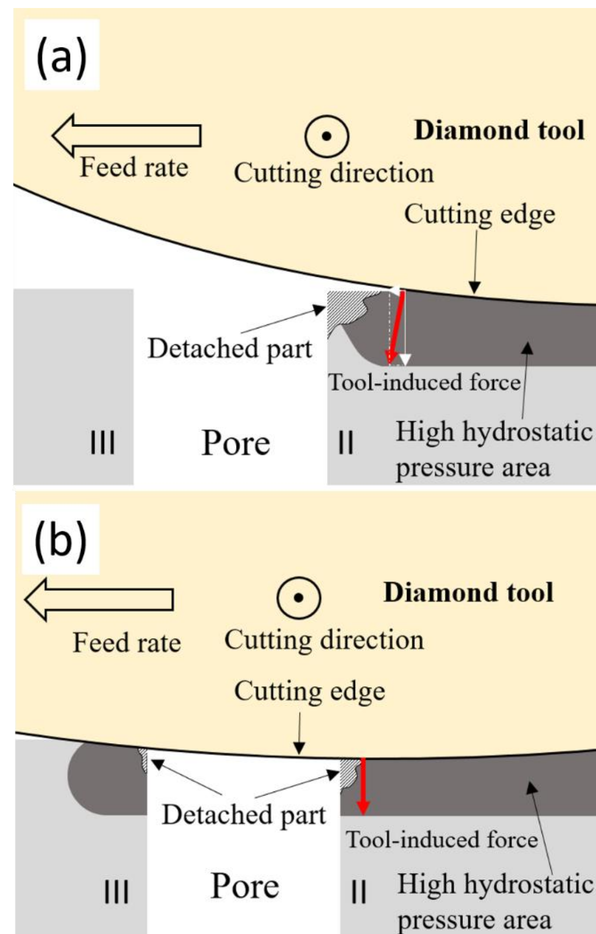

Figure 4-12: Schematic illustrations of cutting mechanisms in (a) II area and (b) III area

SEM images of the machined surface also indicated that as long as undeformed chip thickness was less than 248nm, increasing depth of cut led to significant accumulation of chips in pores. As shown in Figure 4-13, increasing depth of cut at the same feed rate results in higher material removal rate and consequently increases chip volume, and in turn, increased the chance for chips to enter pores.

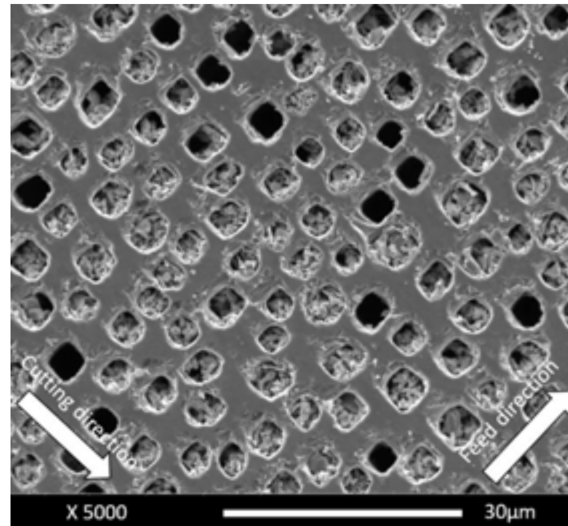

(a) a=1 µm

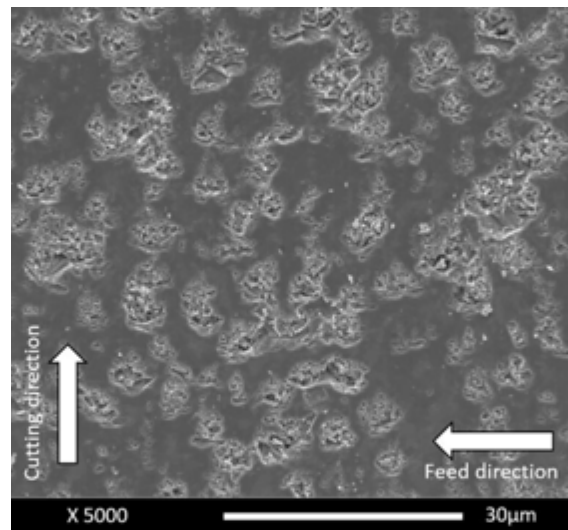

(b) a=4 µm

Figure 4-13: SEM micrograph of surfaces machined at f=2.0 µm/rev and different depth of cuts

4.2.2 *Raman spectroscopy*

It is known that for single-crystal silicon (c-Si), the triple degenerate optical phonons display in the first-order Raman spectrum a sharp peak at the Raman shift of 521 cm^{-1} and for amorphous silicon (a-Si), the first-order Raman spectrum reflects the phonon density of states and presents an optical band peak at 470 cm^{-1} [109,110]. To verify the microstructure of machined porous silicon surface, laser micro-Raman tests were performed on four areas of pores.

In Figure 4-14, curve (I) shows the Raman spectrum of the surface machined at an undeformed chip thickness of 174 nm in “I” area of a pore. There is a characteristic Raman peak of c-Si at 521 cm^{-1}, whereas the intensity at other frequencies is negligibly low. This indicates that the subsurface layer is mainly crystalline silicon. Curves (II) and (III) show the Raman spectrum of the surface machined in the “II” and “III” areas, respectively, where the intensity of the Raman peak of c-Si at 521 cm^{-1} clearly becomes lower than that in (I). However, a broadband peak centered at 470 cm^{-1} appears in (III), indicating that the subsurface layer has been partially transformed into an amorphous state. Curve (IV) shows the Raman spectrum of “IV” area of a pore. The broadband peak at 470 cm^{-1} becomes more significant, whereas a small peak can still be observed at 521 cm^{-1}. This indicates that the subsurface layer within the laser penetration depth has been mostly transformed into an amorphous state. This result is similar to that of the machined bulk single crystal [109].

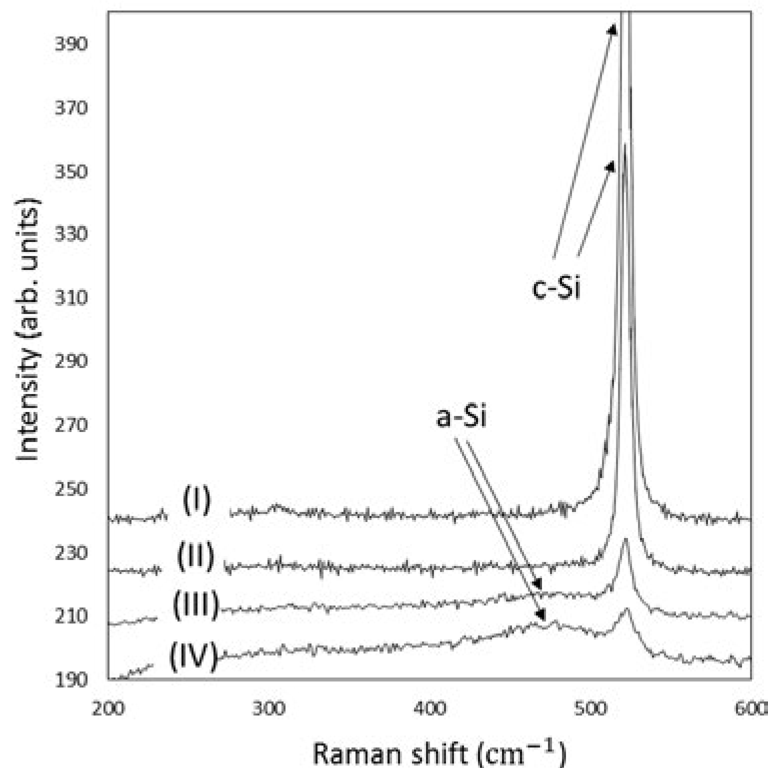

Figure 4-14: Laser micro-Raman spectra of I, II, III and IV areas machined at h_{max} = 174nm (f=2.0 μm/rev, a=2.0 μm)

Raman spectra of the cutting chips were also investigated. Figure 4-15a is the Raman spectrum of chips produced under the feed rate of 0.2 μm/rev, which shows a strong amorphous peak. In contrast, chips produced at a higher feed rate (*f*=2.0 μm/rev) showed a combination of completely amorphous, partially amorphous, as well as crystalline phases, as shown in Figure 4-15b.

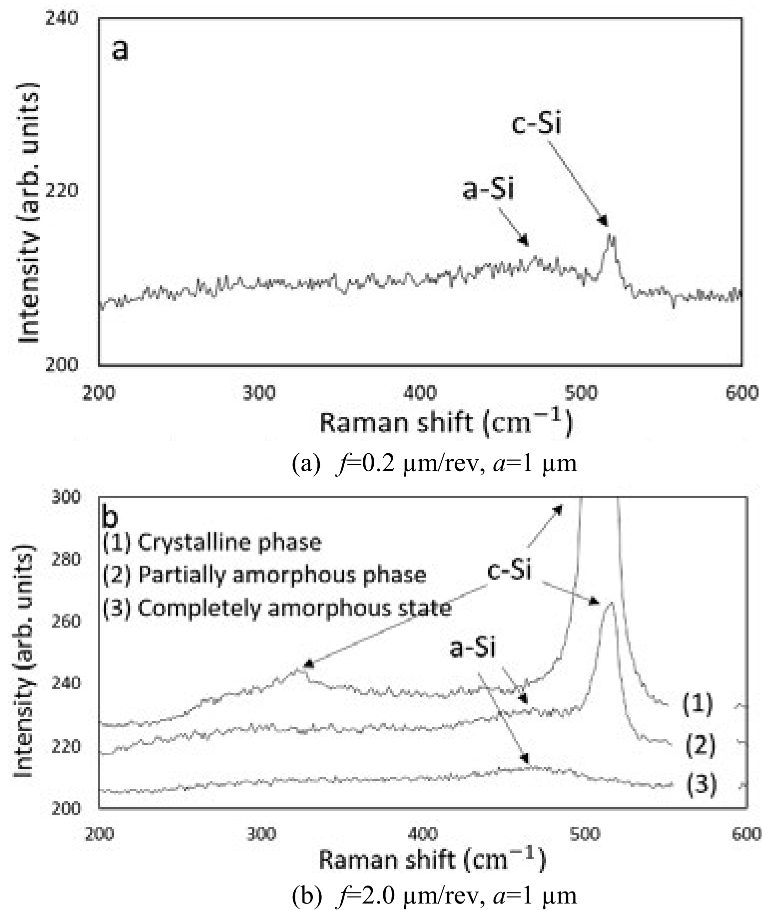

(a) *f*=0.2 μm/rev, *a*=1 μm

(b) *f*=2.0 μm/rev, *a*=1 μm

Figure 4-15: Laser micro-Raman spectra of chips in a pore

4.2.3 Finite element simulation of stress distribution

To understand the change in cutting mechanisms around a pore, the cutting-induced stress distributions at the "I" and "IV" areas around a pore were investigated using the finite element machining simulation.

Figure 4-16 shows stress distributions in the "I" and "IV" areas of a pore for an undeformed chip thickness of 532 nm. As the tool reaches the pore edge in the "I" area, as

shown in Figure 4-16a, a very large tensile stress area is formed beneath the tool tip and extending towards the pore. This kind of tensile stress induces microcrack propagation and results in brittle fractures [111,112]. In contrast, the stress distribution in the "IV" area is similar to that of bulk material cutting, where only an extremely small area beneath the tool tip is under tensile stress while the other areas are under compressive stress, as shown in Figure 4-16b. There is a long area along the wall of the pore showing tensile stress, but the tensile stress is too low to cause brittle fractures. The simulation results agree well with the experimental results in section 4.2.1, indicating that brittle fractures in the "I" area are more significant than those in the "IV" area.

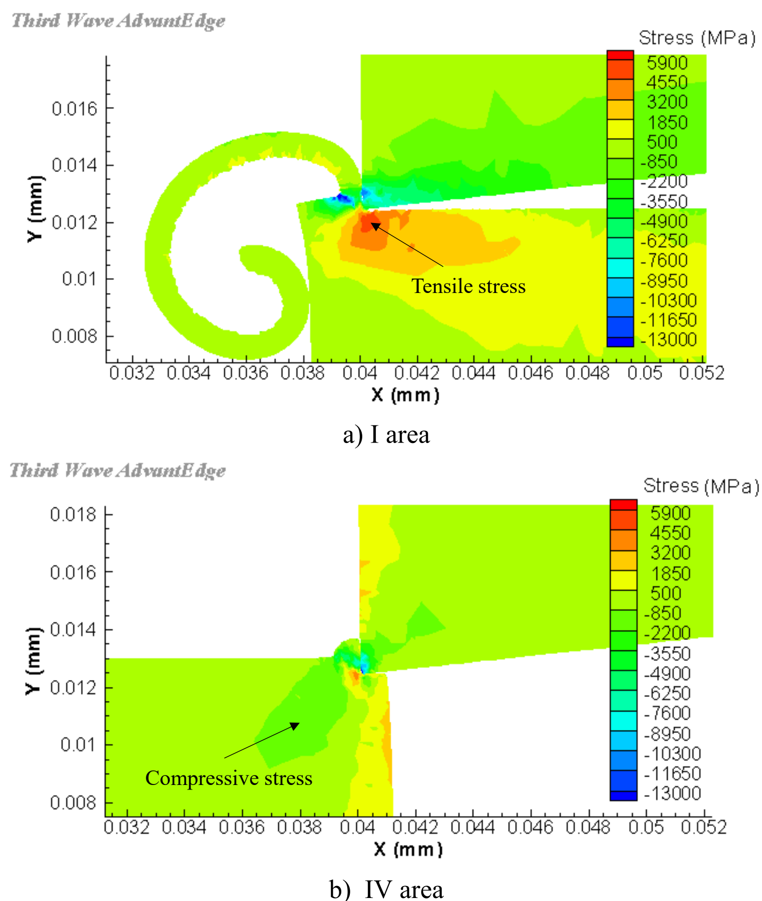

a) I area

b) IV area

Figure 4-16: Stress distribution in the I and IV areas

4.2.4 Effects of wax infiltrant

In order to prevent chips from filling pores during machining, wax was used as infiltrant in the next experiments. As shown in Figure 4-17a, by using wax infiltrant and removing the wax after machining, chip-free pores were successfully obtained. Another noteworthy phenomenon in Figure 4-17a is that there is almost no brittle fracture on the machined surface.

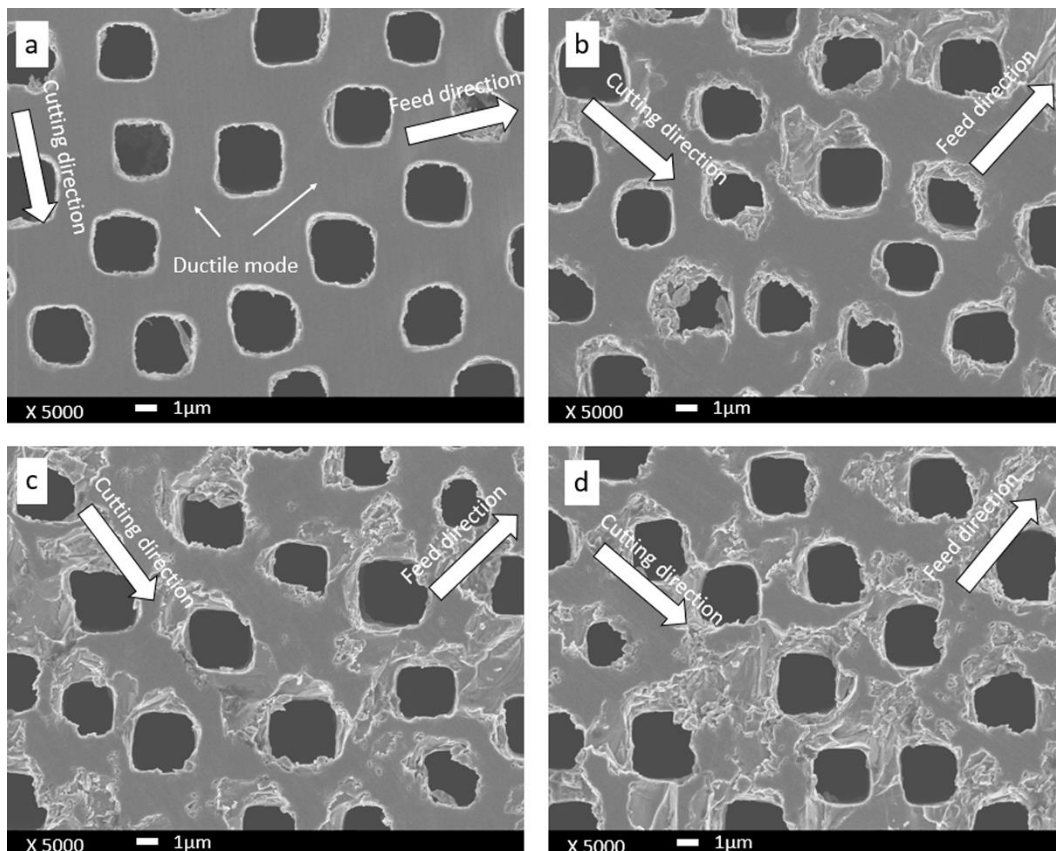

Figure 4-17: SEM micrographs of surfaces machined using wax as infiltrant at different undeformed chip thicknesses: (a) h_{max} =12 nm; (b) h_{max} =286 nm; (c) h_{max} =724 nm; (d) h_{max} =1446 nm

Though the increase in undeformed chip thickness caused brittle fracture generation around pores (Figure 4-17b-d), the brittle fractured areas are much smaller than that without wax infiltrant. In comparison to machining porous silicon without wax condition, using wax as infiltrant shows the significant improvement in the quality of the machined surface. The use of wax as infiltrant might have two advantages. First, it prevents chips from getting into pores.

Second, wax fully filling a pore can help to resist hydrostatic pressure around the pore to some extent, preventing the propagation of cracks.

Figure 4-18 shows four different fracture patterns around pores observed at h_{max}=25 nm. There are no chips in "IV" area thanks to the wax infiltrant. However, some chips are stuck on the "I" area in Figure 4-18b and d. This might be a result of chip embedding into the wax inside the pores. Supported by the wax, the embedded chips are further cut and deformed by the subsequent tool pass, thus adhered onto the pore edges.

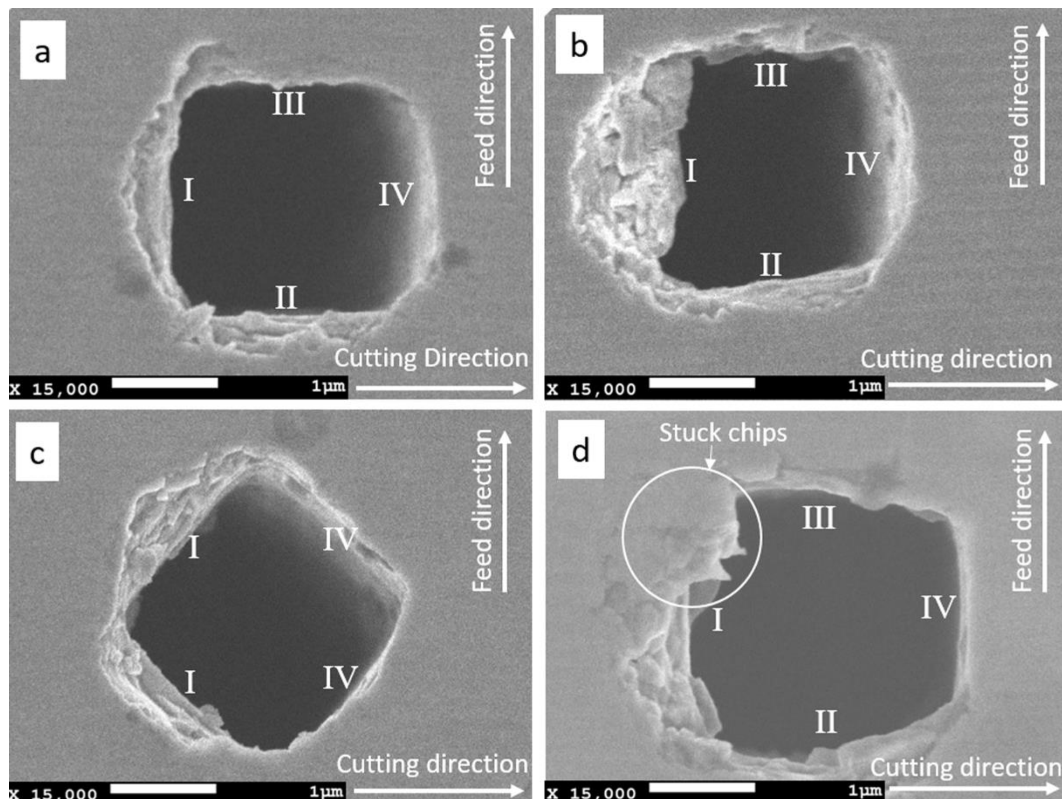

Figure 4-18: Behavior of cutting in various pore areas when using wax (h_{max}=25 nm)

4.2.5 *Effects of tool chipping*

Figure 4-19a is an SEM photograph of the tool edge after cutting of porous silicon for a total cutting distance of 105 m. The undeformed chip thickness was changed from 12.6 nm (f=0.2 μm/rev, a=1 μm) to 1163 nm (f=10.0 μm/rev, a=4 μm) during this cutting distance. In the figure, no obvious wear can be observed whereas a few micro-chippings have occurred to

the edge. The size of these micro-chippings is approximately 1 μm. As cutting distance increased, both the number and the size of the micro-chippings increased. Figure 4-19b is an SEM photograph of the cutting edge after a total cutting distance of 844m, where the size of micro-chippings ranged from 5 to 15 μm.

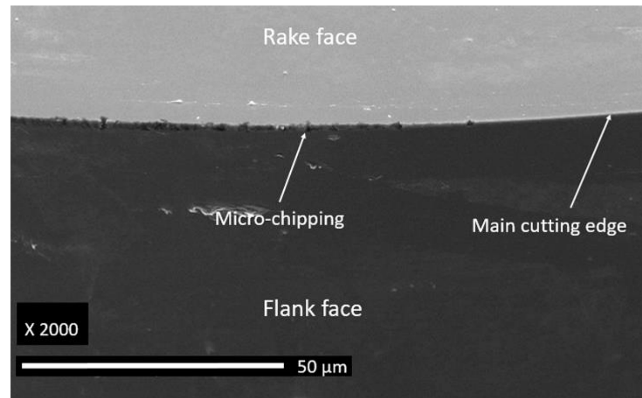

(a) Cutting edge after cutting distance of 105 m

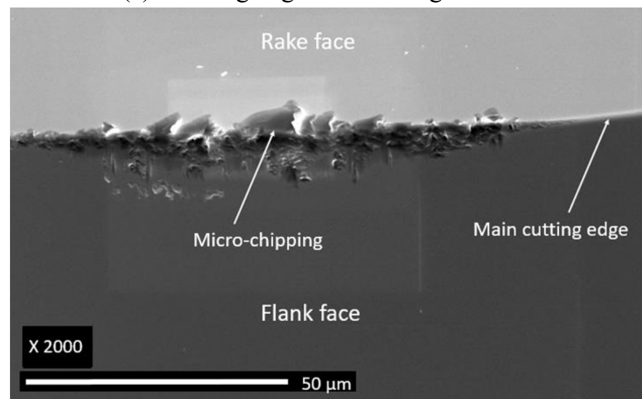

(b) Cutting edge after cutting distance of 844 m

Figure 4-19: SEM photographs of the cutting edge, showing occurrence of micro-chippings

In ultraprecision cutting of bulk single-crystal silicon, there are two types of tool wear: micro-chippings and gradual wear [113]. The tool wear in ductile cutting is a stable and gradual process, where a slight crater wear and a significant flank wear occur. However, under brittle cutting mode, micro-chippings occur to the edge, which are caused by micro impacts from the craters on the workpiece surface. Compared to bulk single-crystal silicon, the cutting mechanism of porous silicon involves numerous micro impacts from the pore edges. Thus, micro-chippings aggravate gradually, leading to bigger edge chippings. This situation is similar

to the fracture of brittle-material tools in interrupted cutting or in the cutting of materials containing hard particles and inclusions [114,115].

Next, the effect of tool chipping on machined surface quality was examined. As shown in Figure 4-20, using a chipped tool as shown in Figure 4-19b led to obvious brittle fractures around pores even at a very small undeformed chip thickness and even when using wax as infiltrant. As the size of tool micro-chippings (5~15 μm) is distinctly bigger than the depth of cut (1~5 μm), the tool will have a highly negative effective rake angle. In the cutting of non-porous silicon, a negative rake angle helps to generate hydrostatic pressure which makes brittle material deform in a plastic manner. In porous silicon cutting, however, the higher the hydrostatic pressure is, the severer the crack propagation around the pores when the high pressure is released around a pore. In addition, a highly negative rake angle pushes more chips inside the pores.

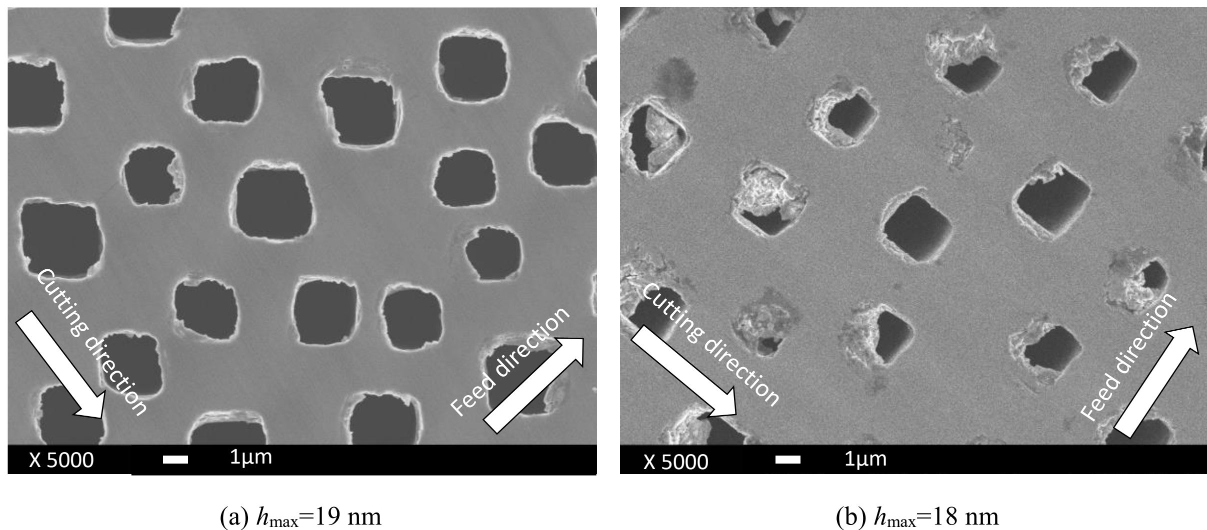

(a) h_{max}=19 nm (b) h_{max}=18 nm

Figure 4-20: Machined surface of porous silicon using (a) a new tool and (b) a chipped tool

4.2.6 Cutting force characteristics

A comparison of cutting forces (principal forces) of bulk single-crystal silicon and porous silicon is plotted in Figure 4-21. In the Figure, “a”, “b” and “c” indicate three stages of face turning: the stage of tool approaching to the workpiece, the steady cutting stage, and the

stage of tool detaching from the workpiece, respectively. Figure 4-21 indicates that the magnitude of cutting force in machining of bulk single-crystal silicon is higher than that of porous silicon. This result might be attributed to two aspects: the low density of porous silicon, and the significant brittle fractures occurring around the pores.

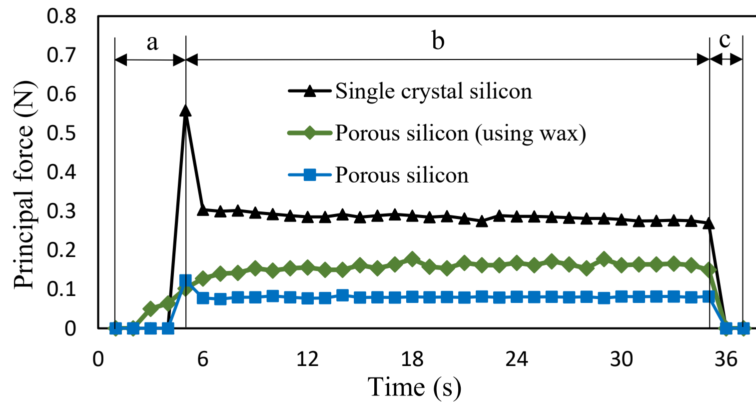

(a) h_{max}=248 nm (f=2.0 μm/rev, a=4 μm)

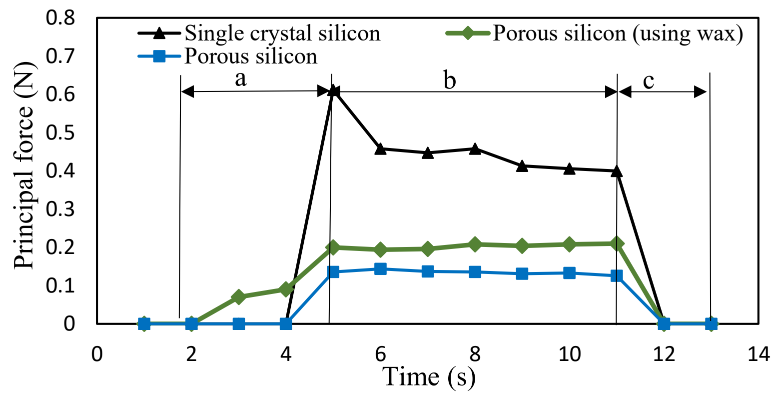

(b) h_{max}=1163 nm (f=10.0 μm/rev, a=4 μm)

Figure 4-21: Cutting force measurement results

To further investigate the major factor reducing the cutting force of porous silicon, the machining pressure induced by principal force was calculated using the chip cross section model in Figure 4-22. The pressure was calculated from the principal force F and the contact area A_c perpendicular to the principal force F_c as

$$P = \frac{F_c}{A_c} \tag{3}$$

Where F_c is derived from the experimentally measured principal force, and A_c is calculated by the following integral equation:

$$
\begin{aligned}
A_c = & \left(\int_{\frac{f}{2}}^{\sqrt{2Ra-a}} R - \sqrt{R^2 - x^2}\,\mathrm{dx}\right) + (f \times a) \\
& - \left(\int_{\frac{f}{2}}^{\sqrt{2Ra-a}+f} R - \sqrt{R^2 - (x-f)^2}\,\mathrm{dx}\right) \\
& = \left[-\frac{1}{2}R^2\left(\arcsin\left(\frac{x}{R}\right) + \frac{1}{2}\sin\left(2\arcsin\left(\frac{x}{R}\right)\right)\right) + Rx \right. \\
& \left. + \mathrm{C}_1\right] + [f \times a] \\
& - \left[-\frac{1}{2}R^2\left(\arcsin\left(\frac{x-f}{R}\right)\right.\right. \\
& \left.\left. + \frac{1}{2}\sin\left(2\arcsin\left(\frac{x-f}{R}\right)\right)\right) + R(x-f) + \mathrm{C}_2\right]
\end{aligned}
\tag{4}
$$

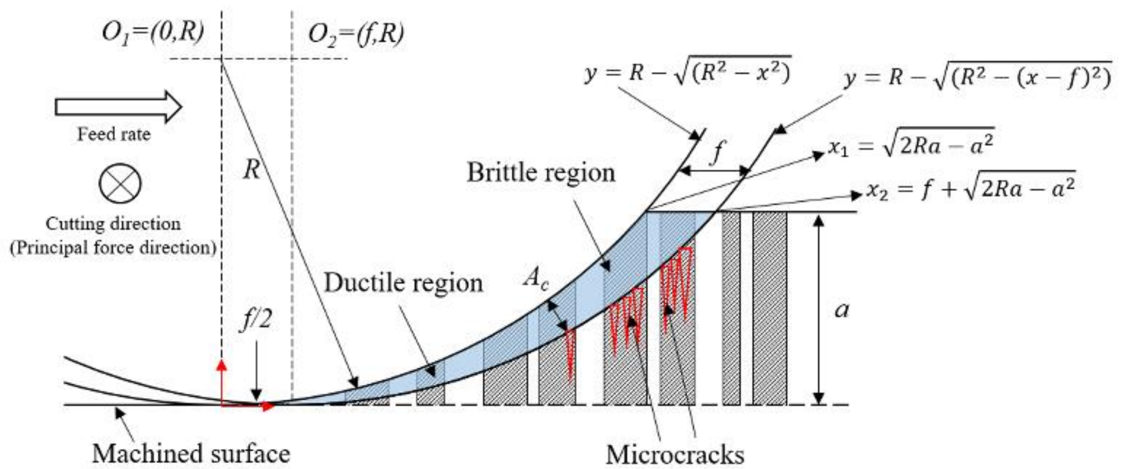

Figure 4-22: Schematic model for undeformed chip cross section

When calculating the effective contact area between silicon and diamond, the porosity of the porous silicon workpiece was estimated by analyzing the SEM images of 10 different parts of the porous silicon surface using the ImageJ software. The results indicated that the surface porosity was approximately 30%. Therefore, the effective contact area between silicon and diamond was 0.7 times that of the cross-sectional area of the chip.

Table 4-2 shows the machining pressures in single-crystal silicon and porous silicon. The result reveals that the machining pressure decreases sharply with increasing tool feed rate. As the undeformed chip thickness increases, the principal force increase, but the slope of the force increase in the brittle region is remarkably smaller than that in the ductile region, because the brittle material removal results in lower cutting forces and subsequently less machining pressure [29,34]. From this meaning, it is presumable that the reduction of machining pressure in cutting porous silicon was mainly caused by the brittle fractures occurring around the pores.

It is also noted that using wax as infiltrant leads cutting force to increase. This increase can be accounted for the cutting resistance from the wax layer, which was about 30 μm thick above the porous silicon surface. In Figure 4-21, the cutting forces between the third and fourth seconds were caused by the wax layer only.

Table 4-2: Machining pressure

Workpiece material	f(μm/rev), a(μm)	A_c ($\times 10^{-12}$m^2)	F(N)	$P=F/A_c$ (GPa)
Single crystal silicon	f=2.0, a=4	7.9993	0.2861	35.76
	f=10.0, a=4	39.9167	0.4364	10.93
Porous silicon	f=2.0, a=4	0.7×7.9993	0.0802	14.32
	f=10.0, a=4	0.7×39.9167	0.1362	4.87

4.2.7 Surface flatness

Surface flatness was measured in three-dimensional (3D) forms in which the average arithmetical deviation of the area was calculated by using the TalyMap software. As the range of measurement of the white light interferometer was from -50 μm to 50 μm, it was not able to obtain data from the bottom of a pore. Thus, surface flatness measurement was based on the data obtained from areas among pores.

As shown in Figure 4-23, the surface flatness of machined surface using wax infiltrant is better than that without wax and is almost the same as that of a single-crystal silicon wafer (flatness ranging from 8 to 13 nm) when undeformed chip thickness is $h_{max} < 25$ nm. Increasing undeformed chip thickness leads to worse surface flatness. Cutting porous silicon without wax infiltrant results in surface flatness between 80 nm to 180 nm. The surface flatness increases to ~500 nm when a chipped tool is used for cutting.

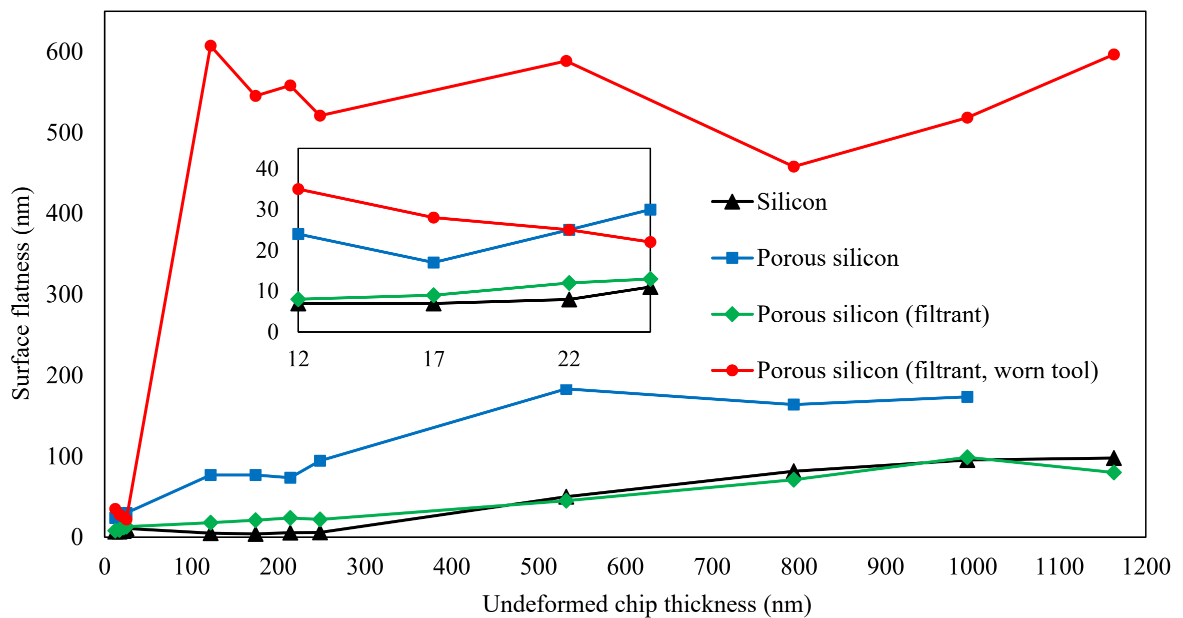

Figure 4-23: Flatness of machined surfaces

Figure 4-24 shows 3D surface topographies of porous silicon before and after diamond turning. By applying wax as infiltrant and using a small undeformed chip thickness ($h_{max} < 25$ nm), high surface flatness is achieved. The surface flatness of the as-received porous silicon was 42 nm, while the one after diamond turning was 13 nm.

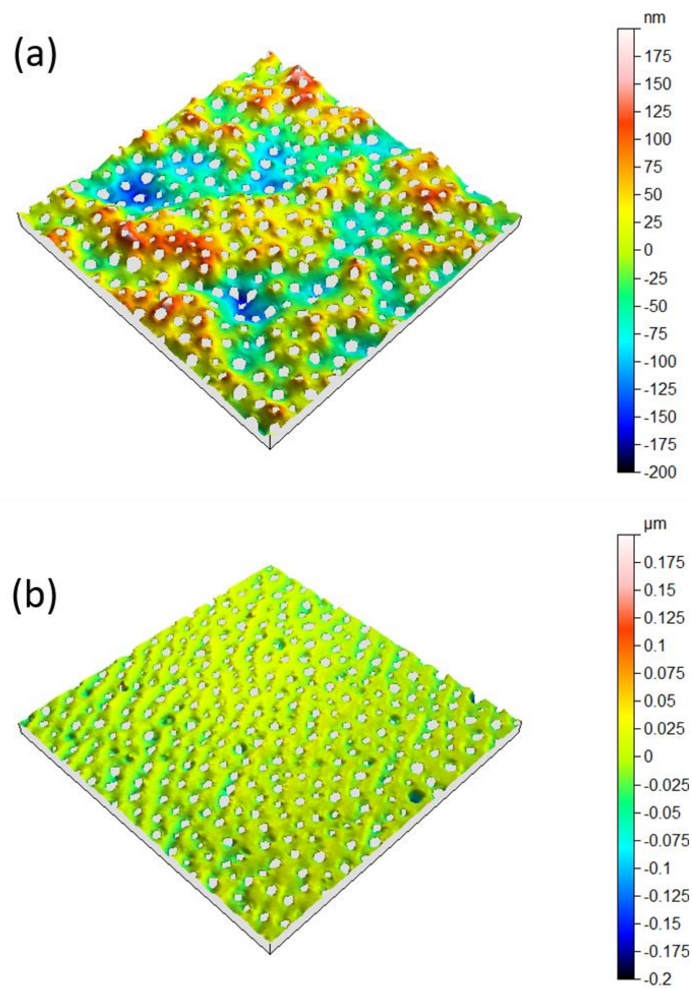

Figure 4-24: 3D surface topographies of (a) original porous silicon and (b) machined one

4.3 Conclusions

The fundamental material removal phenomena in diamond turning of porous silicon under various conditions were investigated experimentally. The following conclusions were drawn.

(1) The mechanism of cutting porous silicon is significantly different from that of bulk silicon due to the existence of pores. The hydrostatic pressure induced by the cutting tool is released near the edge of a pore, causing microfractures.

(2) The mechanism of material removal is strongly dependent on the direction of cutting with respect to the pore edge orientation. Three types of material removal behaviors were confirmed in various areas around a pore: severely fractured area, slightly fractured area, and ductile-cut area.

(3) Raman spectroscopy showed that the material structures of subsurface layers of the above three kinds of areas are crystalline, partially amorphous, and completely amorphous, respectively.

(4) Cutting porous silicon using wax as infiltrant not only prevents chips from entering pores but also shows significant improvement in surface quality in terms of decreasing brittle fractures.

(5) Micro-chippings of cutting edge occur, the number of size of which increases with total cutting distance. Tool chippings cause a significant increase in micro fractures of silicon around pores.

(6) The cutting force in machining of porous silicon is remarkably lower than that of bulk single-crystal silicon due to the brittle fractures around pores and the low density of porous silicon.

(7) The surface flatness of anodized porous silicon may be improved to the nanometer level by diamond turning.

The present study has demonstrated that by controlling cutting parameters and using wax as pore infiltrant, it is possible to obtain an extremely high surface flatness of porous silicon.

CHAPTER 5

Machining of porous titanium

Chapter 5 : Machining of porous titanium

5.1 Material and methods

5.1.1 Machining apparatus

Face turning was performed using a three-axis control ultraprecision machine, NACHI ASP-15 (NACHI-FUJIKOSHI CORP). A piezoelectric dynamometer (Kistler 9256C2) was mounted below the tool holder to measure cutting forces during the cutting tests. Figure 5-1 shows a schematic diagram of the experimental setup.

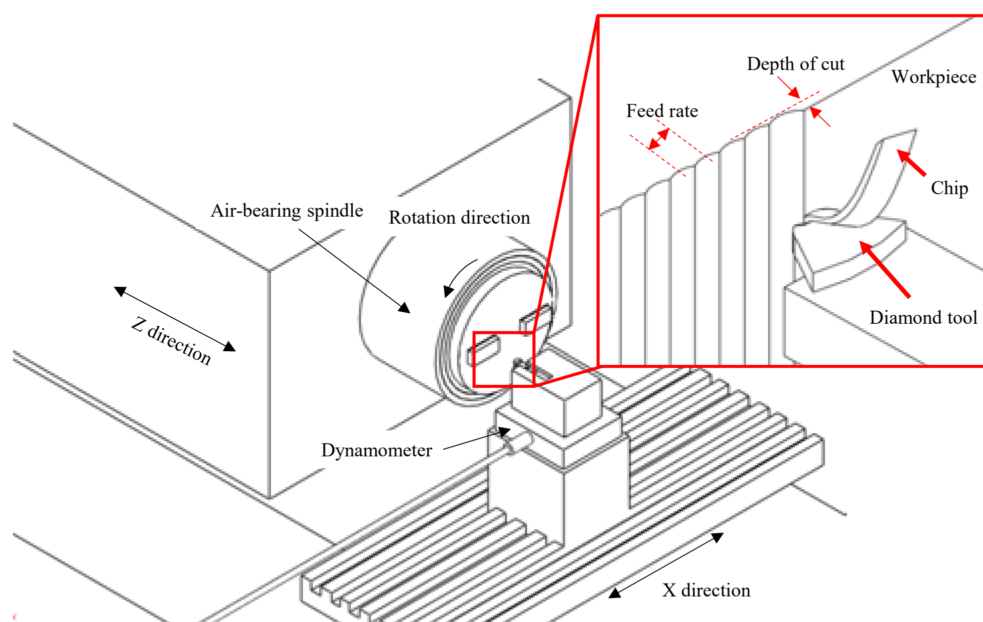

Figure 5-1: Schematic diagram of experimental setup

A workpiece holder was designed and fabricated to fix the workpiece to the spindle using a sliding mechanism to adjust the distance between the workpiece and the center of the spindle. The workpiece was fixed using three screws to the holder which is then vacuum chucked to the machine spindle. A metal piece was fixed on the opposite side of the workpiece to keep dynamic balance during spindle rotation. To guarantee the accuracy of results, all machining tests were repeated twice at the same conditions.

5.1.2 Diamond tool

In this study commercially available single-crystal diamond tools with a nose radius of 1.0 mm, tool edge radius of ~100 nm, rake and clearance angles of 0º and 8º, respectively, were used in these experiments. Figure 5-2 shows SEM images and contour profiling error of a single-crystal diamond tool. The tool faces and the edge are extremely smooth. The geometrical error over a window angle of 100˚ is ~380 nm, thus in the actually used range of tool edge, the profile accuracy of the tool is in the nanometer scale.

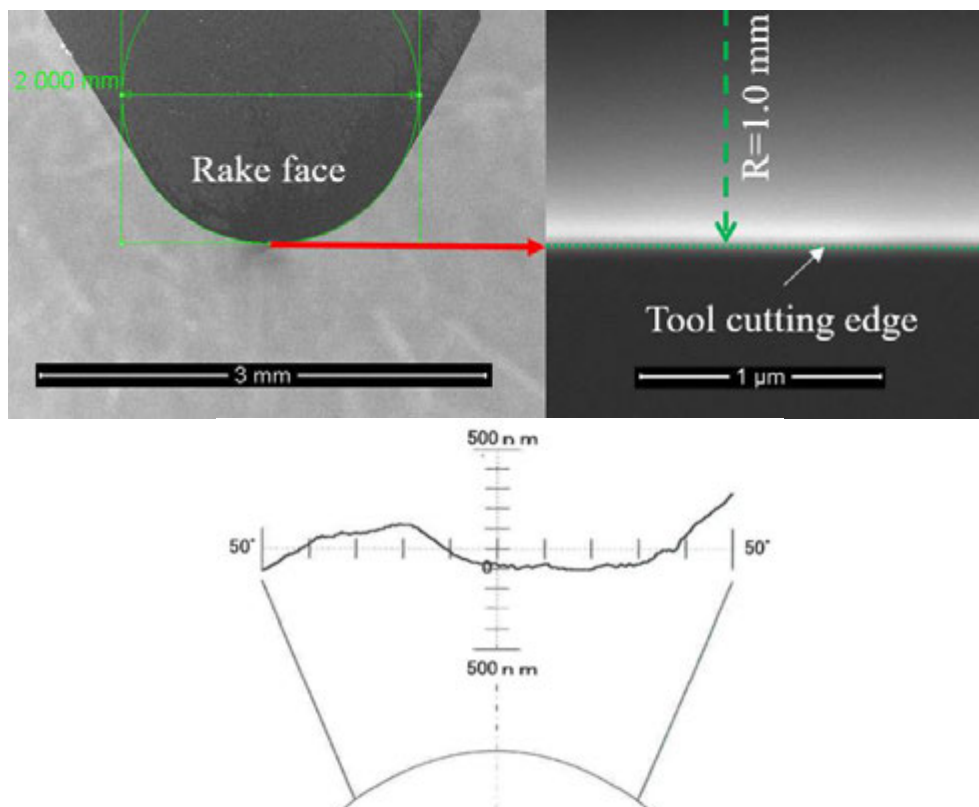

Figure 5-2: SEM micrograph and contour profile of a diamond tool edge

In ultraprecision diamond turning with a round-nosed tool, the maximum undeformed chip thickness (h_{max}) is an important parameter to evaluate the cutting performance. Figure 5-3 shows a schematic model for diamond turning with a round-nosed tool. $h_{\max}$ can be calculated from the tool nose radius R, depth of cut a and tool feed rate f, using Eq. (2).

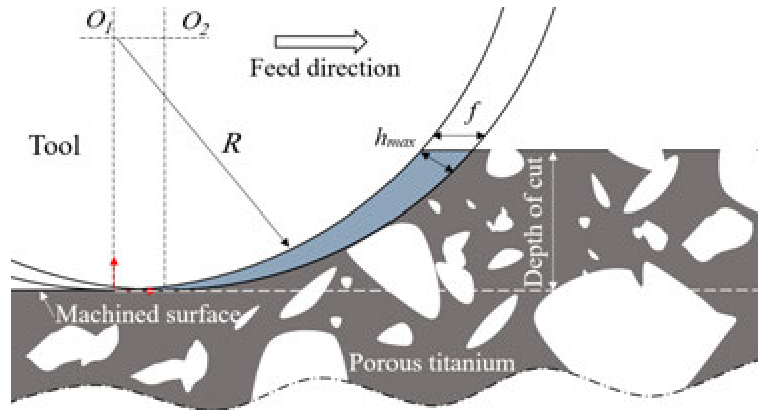

Figure 5-3: Cutting model for a round-nosed tool

5.1.3 Workpiece materials

Porous titanium blocks (sample size: 20.0 mm × 15.0 mm × 10.0 mm) with purity of 99.8% were used as workpieces. For comparison, pure titanium blocks with the same size were also machined. The chemical compositions of both pure titanium and porous titanium were the same, as shown in Table 5-1. The porosity of the porous titanium samples used in the experiments was ~30%, with pore size ranging from a few nanometers to ~100 microns. The titanium sample has ultimate tensile strength of 370 MPa, yield strength of 300 MPa and hardness of 145 HV.

Table 5-1: Chemical compositions of porous titanium

Purity%	Fe%	O%	C%	N%	H%
99.8	0.04-0.25	0.1-0.2	0.0-0.08	0.0-0.03	0.01-0.13

5.1.4 Machining conditions

Four feed rates and two depths of cut were used to cut concentric areas on each sample. Since the distance of each area from the spindle center is different, spindle rotation rate was adjusted for each area to get the same cutting speed in all tests. Table 5-2 shows the machining parameters of experiments. In addition, experiments were performed under dry cutting

conditions and wet conditions using a coolant, respectively. As coolant, CASTY-LUBE® B-905, a fatty acid ester, with a density of 0.8782 (15 ºC) g/cm^3 was used in the form of mist jet.

Table 5-2: Machining conditions

Depth of cut *(a)*	5, 15 μm
Feed rate *(f)*	1, 10, 50, 100 μm/rev
Cutting speed *(v)*	50 m/min
Spindle rotation *(n)*	252 ~ 176 rpm
Maximum undeformed chip thickness *(h_{max})*	99 ~12331 nm

5.1.5 Measurement apparatus

In order to evaluate the machined surface texture, a white light interferometer was used and the surface profile was analyzed by the Talymap software (Taylor Hobson Ltd.). A scanning electron microscope (SEM, Model Inspect S50) was used to observe the chips, the machined surfaces and tool wear. SEM images of the machined surface were then used for analyzing the surface porosity using the ImageJ software. To evaluate surface hardness variations, hardness measurements were performed using a micro Vickers hardness tester (Shimadzu HMV-G21S) by applying a load of 1 N for 10 s on selected specimens.

5.1.6 Finite element simulation

To assist understanding the material removal mechanism of porous titanium, the material deformation in the cutting area was simulated by using AdvantEdge, a finite element (FE) machining simulation program produced by Third Wave Systems USA. Two-dimensional simulations of orthogonal cutting were performed, thus, the undeformed chip thickness was the same as the depth of cut. The tool rake angle, relief angle and cutting speed used in the simulations were the same as those used in the experiments. Using a tool edge radius (*r*) smaller than 100 nm, as used in experiment, was extremely time-consuming in simulations, so an edge

radius of 400 nm was used. Accordingly, depth of cuts (a) were also enlarged in the simulation to keep the same proportion of depth of cut to edge radius as that in experiments. The coefficient of friction between rake face and chip used in the FE simulations was 0.7, which was obtained from experimental tests in micrometer scale cutting of titanium. For workpiece and tool meshing, the minimum element size was 0.0001 mm with 600000 maximum number of nodes, in which mesh refinement and coarsening factors are 2 and 6 respectively. The mechanical properties such as ultimate tensile strength, yield strength and hardness used in the simulations were the same as those of titanium sample. The modified power law constitutive model was used to establish the material property model for titanium.

In order to minimize boundary effects, the workpiece height should be at least five times of the depth of cut according to AdvantEdge guideline. In this work it is 1000 times bigger than depth of cut. In addition, the length of cut should be 20 times the depth of cut. The workpieces were constrained from displacement in the X and Y axis in the bottom plane. The right and top-most sides of the tool are fixed in the X and Y directions.

5.2 Results and discussion

5.2.1 Cutting force characteristics

Figure 5-4 shows the principal force (F_c), thrust force (F_t) and resultant force (F_r) during machining titanium (Ti) and porous titanium (PTi) at two depth of cuts. The figure indicates the decrease of resultant force as feed rate decreases. There is also an increase in cutting forces as depth of cut increases from 5 to 15 μm. Comparison of cutting forces between pure titanium and porous titanium shows that, although the magnitude of cutting forces of pure titanium is about 15% greater than that of porous titanium at a high feed rate (100 μm/rev) and depth of cut (15 μm), this percentage becomes zero at a low feed rate (1 μm/rev). The gap in cutting

force between pure titanium and porous titanium is caused by the pores which reduce the effective volume of deformed material.

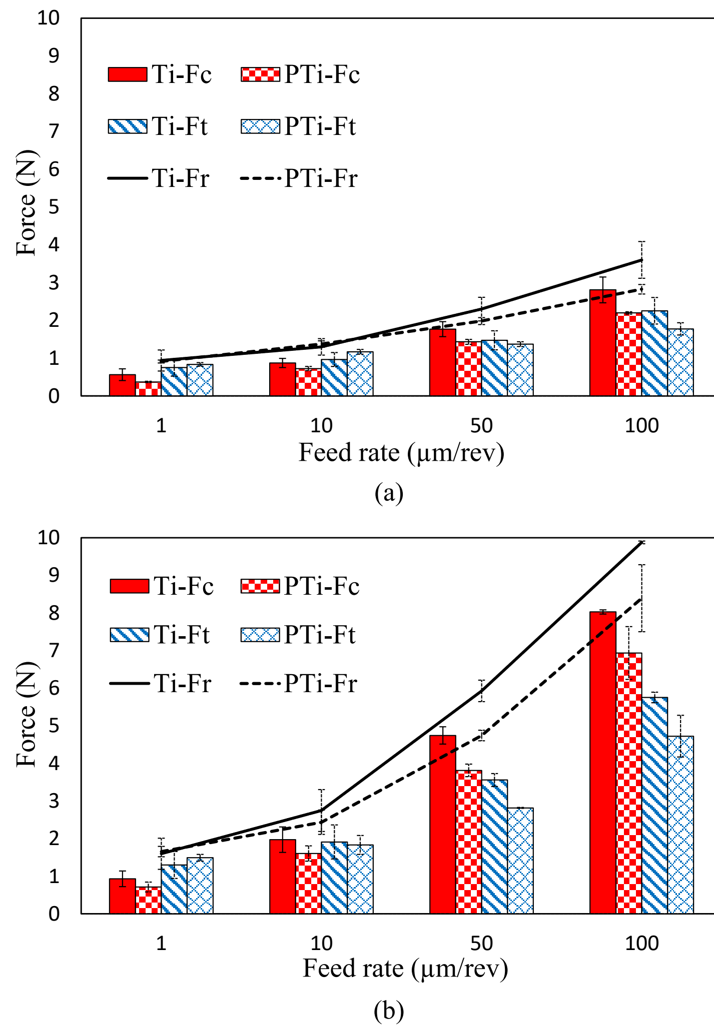

Figure 5-4: Cutting forces of pure titanium (Ti) and porous titanium (PTi) in dry condition at depth of cut (a) 5 µm and (b) 15 µm

5.2.2 *Shear angle*

Next, the shear angle φ, which is defined as the angle between the shear plane and the cutting direction, was derived from arctangent of the ratio (r_c) of undeformed chip thickness (h) to the chip thickness (l). Concerning the shear angle changes along the round edge of the tool, in this study, the shear angle was calculated based on maximum chip thickness measured using ImageJ software by analyzing the SEM images of chips, as shown in Figure 5-5.

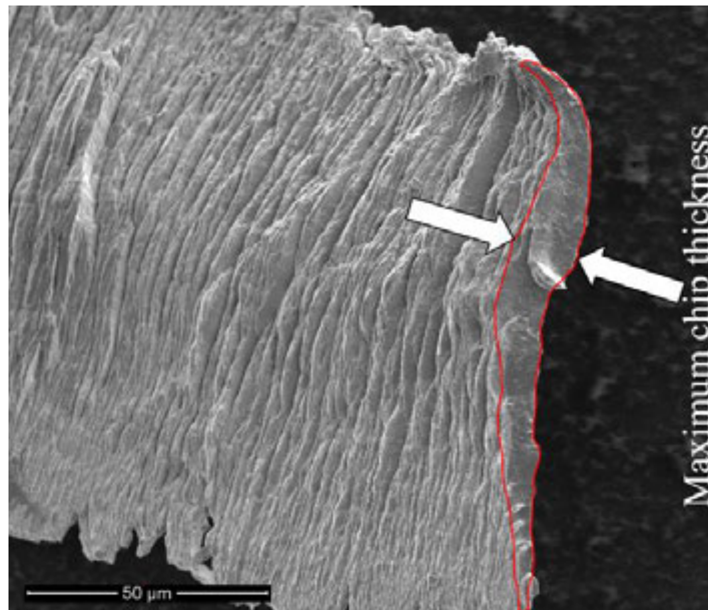

Figure 5-5: SEM micrograph of chip (f=100 µm/rev, a=5 µm) used for measuring chip thickness

Figure 5-6 shows shear angle results. Although the shear angle for porous titanium demonstrates a similar trend to that for pure titanium workpiece with respect to undeformed chip thickness, the shear angle of porous titanium is larger than that of pure titanium. The difference of shear angle is ~10º under the present conditions. The significant difference in shear angle between pure titanium and porous titanium is due to the presence of pores. This difference can be explained based on deformation process of pores in the shear zone (see section 5.2.3).

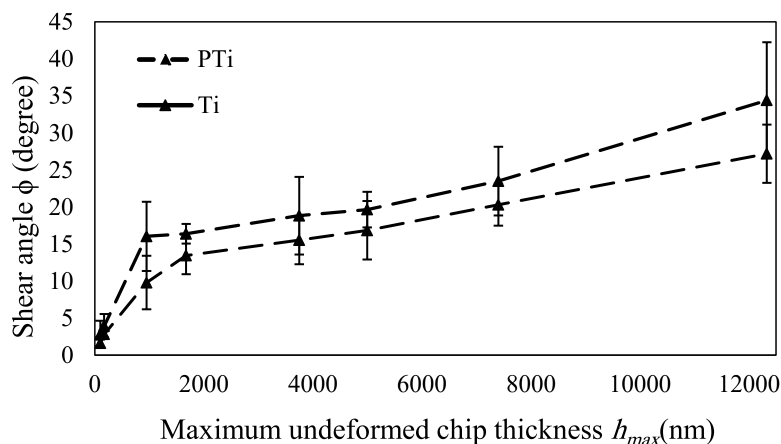

Figure 5-6: Changes of shear angle with h_{max}

FE modeling of cutting at different undeformed chip thicknesses also confirm that shear angle decreases as h_{max} decreases, as presented in Figure 5-7. The simulation results also proved that as undeformed chip thickness decreased, the narrow shear plane gradually converted to a broad shear zone.

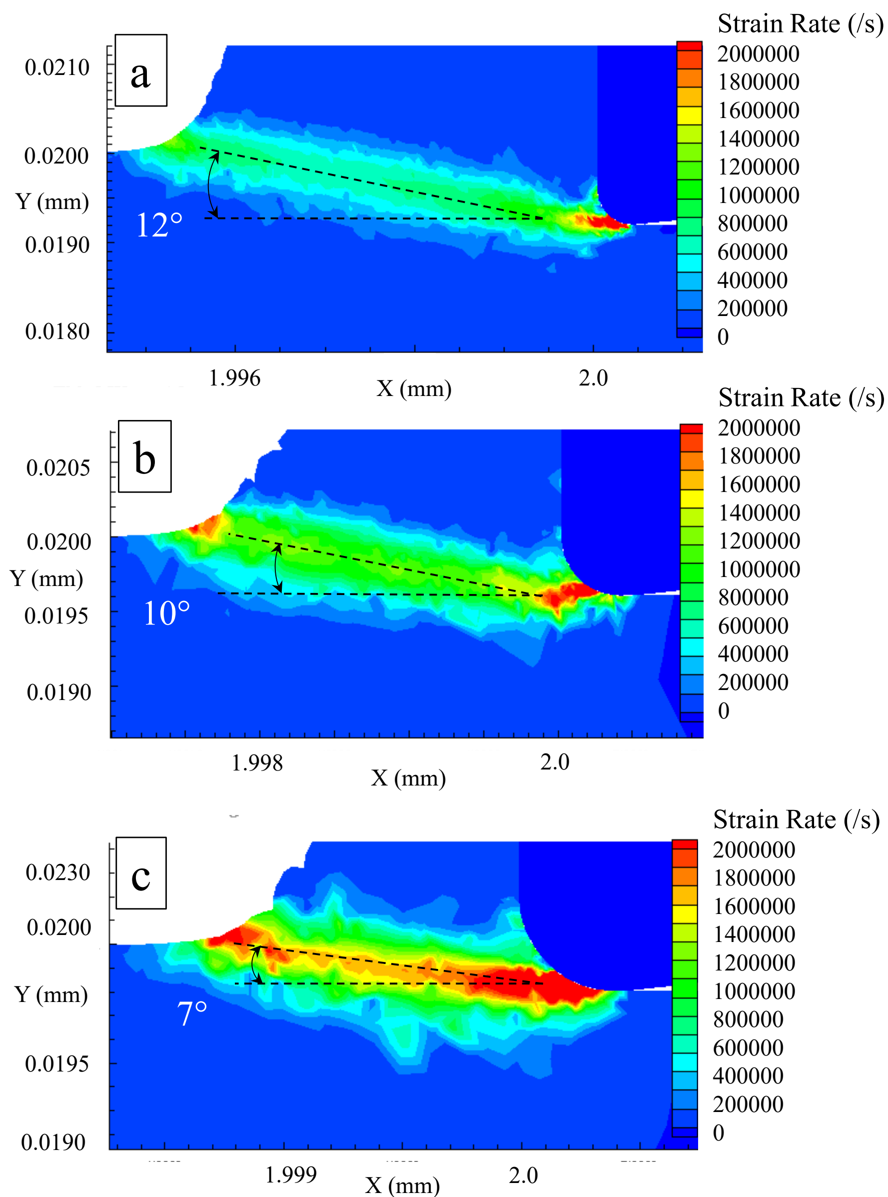

Figure 5-7: FE simulations of strain rate distribution at three different depth of cuts: (a) a=2.0×r (b) a=1.0×r (c) a=0.5×r

5.2.3 Chip morphology

Figure 5-8a, b, and c, d show the chips obtained at h_{max}=7405 nm and h_{max}=1679 nm, respectively. In the figure, chip edge tearing phenomenon is observed. The chip tearing is more significant in Figure 5-8a and c (left side of the chip) compared to Figure 5-8b and d (right side of the chip). This result demonstrated that a larger cutting width with smaller undeformed chip thickness caused more severe chip tearing. Apart from chip tearing, cracks were generated on the left side chip edge in Figure 5-8a and c.

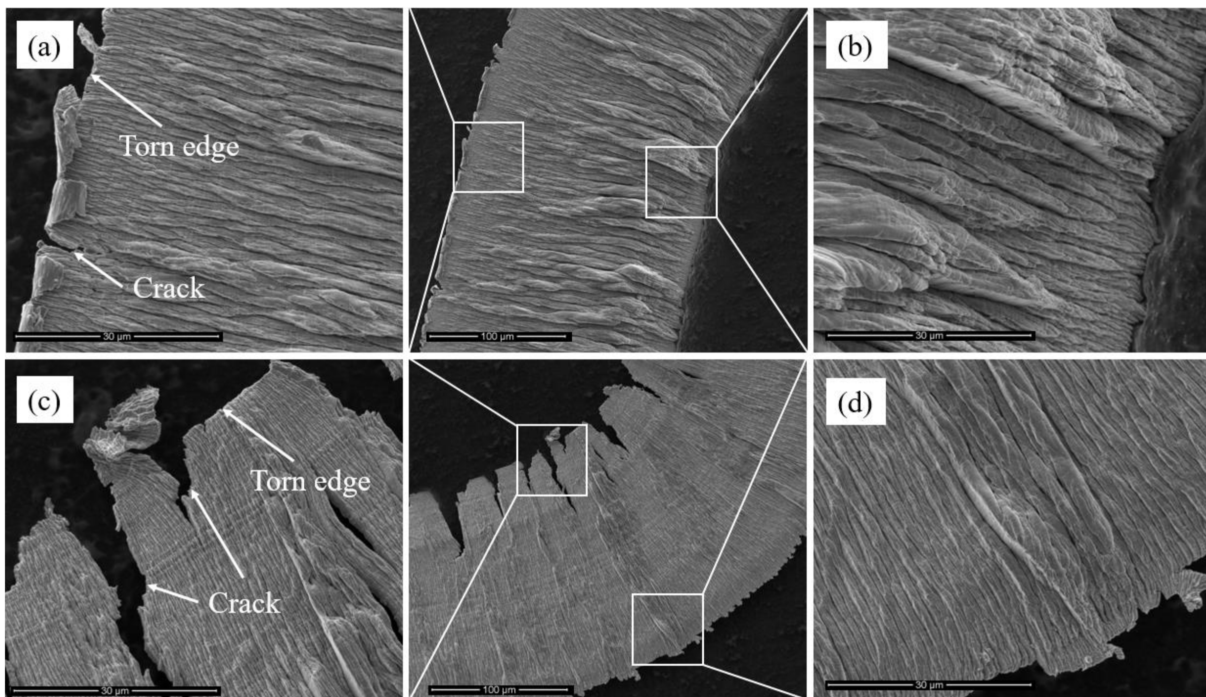

Figure 5-8: SEM micrographs of chip obtained at ((a) and (b)) h_{max} =7405 nm and ((c) and (d)) h_{max} =1679 nm

In order to understand the chip tearing phenomenon, the change in cutting force direction with undeformed chip thickness was calculated. Figure 5-9 shows the change of resultant force angle with h_{max}. As undeformed chip thickness decreases, resultant force angle (γ) increases from 36° at h_{max}=12331 nm to 57° at h_{max}=99 nm. Similarly, as undeformed chip thickness decreases from the uncut surface to the cut surface in Figure 5-3, the resultant force direction will change significantly.

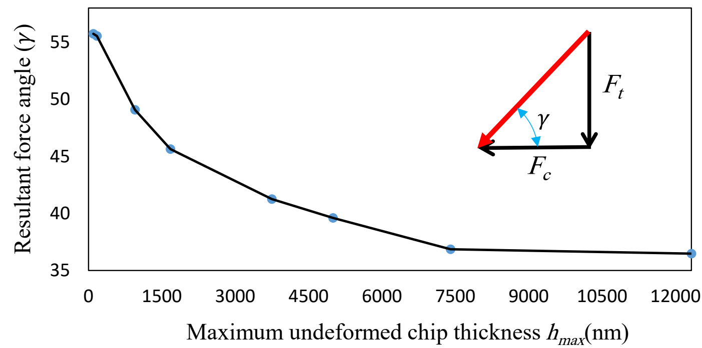

Figure 5-9: Change of resultant force angle with h_{max}

Figure 5-10 shows a schematic three-dimensional model for tool-workpiece contact area. While the area of the plane normal to principal force decreases from right side "II" to left side "I", the area of the plane normal to thrust force, which is determined by tool edge radius, remains constant along the tool edge. Thus, the resultant force in the region close to "II" is mostly parallel to cutting direction, while that around "I" is directed towards the workpiece surface.

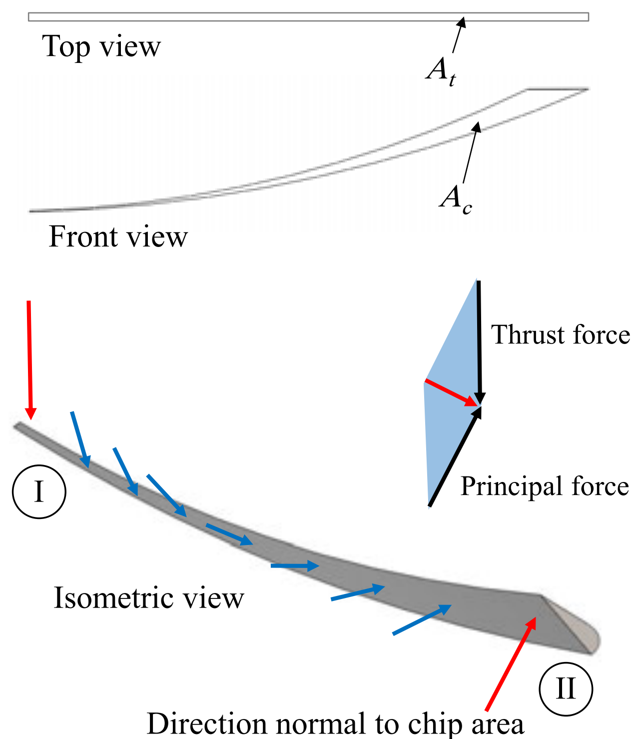

Figure 5-10: Schematic model for tool-workpiece contact area

The change of resultant force direction along the tool edge as shown in Figure 5-10 leads to different chip formation behaviors. The force component vertical to the workpiece surface near region "I" causes chip tearing (Figure 5-8a and c). However, the force component parallel to cutting direction near region "II" cause continuous chip flow (Figure 5-8b and d).

Next, the specific cutting force [116–118], i.e., the ratio of the resultant force to the tool-workpiece contact area projected on the plane normal to the resultant force (Figure 5-11), was calculated using following equations.

$$F_{Sp} = \frac{F_r}{A'_r} \tag{5}$$

$$F_r^2 = F_c^2 + F_t^2 \tag{6}$$

$$\tan\gamma = \frac{F_t}{F_C}, \ \tan\delta = \frac{A_t}{A_C}, \ A'_r = A_r\cos(\gamma - \delta) \tag{7}$$

$$A_t = r \times \left[2\pi R \left(\frac{\alpha+\beta}{360}\right)\right] \text{ (see Figure 5-15a)} \tag{8}$$

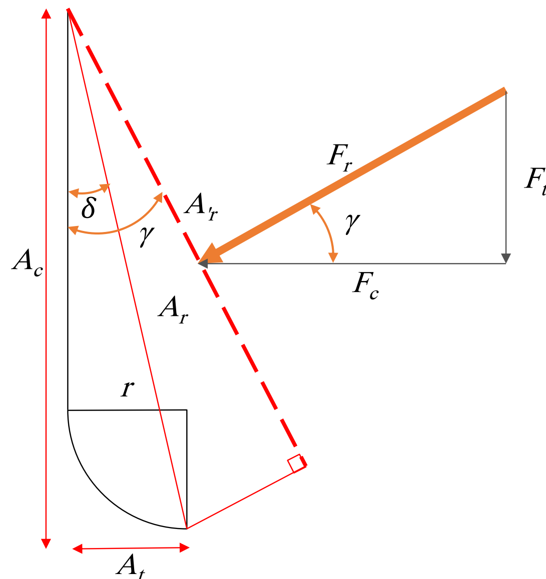

Figure 5-11: Model for calculating specific cutting force

Where F_{sp} is specific cutting force, F_r is resultant force, F_c is principal force, F_t is thrust force, A_c is area normal to principal force which can be calculated by Eq. (4), A_t is area normal

to thrust force and derived from multiplication of tool edge radius (r) in the width of chip, A_r is the resultant area of A_c and A_t, A'_r is area of A_r normal to resultant force, γ and δ are angles between A'_r and A_r and the vertical direction respectively, R is tool nose radius, α is angle between vertical direction and line connect the center of tool nose radius to desired depth of cut in undeformed chip profile, β is angle between vertical direction and line connect the center of tool nose radius to the end point of chips (see Figure 5-15a). It should be pointed out that as tool wears out the tool edge radius increases, and consequently, cutting force increases. To reduce the effects of tool wear on specific cutting force results, a new tool was used for a very short cutting distance (~75 m) for force measurement.

Figure 5-12 shows the results of specific cutting force with respect to h_{max}. As h_{max} decreases, the specific cutting force increases slightly at the micro level, and then sharply when h_{max} approaches the sub-micrometer level. As the ratio between the undeformed chip thickness and the tool edge radius decreases, the size effect in specific cutting force is predominant, as known in traditional metal cutting [65,119–125]. Decreasing this ratio also leads to increased fluctuation of specific cutting force, as shown in Figure 5-12, due to the pores and saw-toothed chip formation. The specific cutting force in porous titanium cutting is slightly lower than that in pure titanium cutting due to the existence of pores and the different disappear in the nanometer rage.

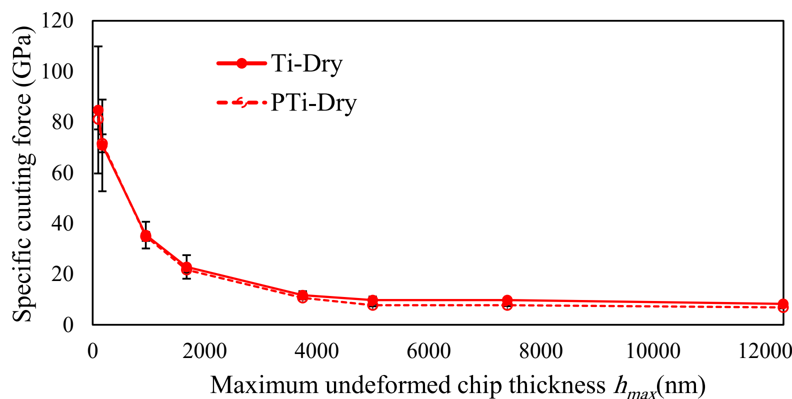

Figure 5-12: Changes of specific cutting force with h_{max}

The presence of pores causes the edge-induced stress to be released as it reaches a pore leading to decreasing specific cutting force down to 20% in micro-scale cutting. Decreasing specific cutting force is the main reason of increasing shear angle in porous titanium cutting (Figure 5-6) [126,127]. However, as undeformed chip thickness decreases to the nanometer scale, shear angle gap vanishes and specific cutting force increases due to the welding phenomenon (see more in section 5.6).

5.2.4 Chip tearing

For the "II" side of the chip, instead of chip tearing, chip edge wrinkle was observed at a small $h_{\max}$, when a worn tool was used. As shown in Figure 5-13a, chip wrinkle is found at the upper side edge of chips formed at $h_{\max}$ = 172 nm by a tool after a cutting distance of 250 m.

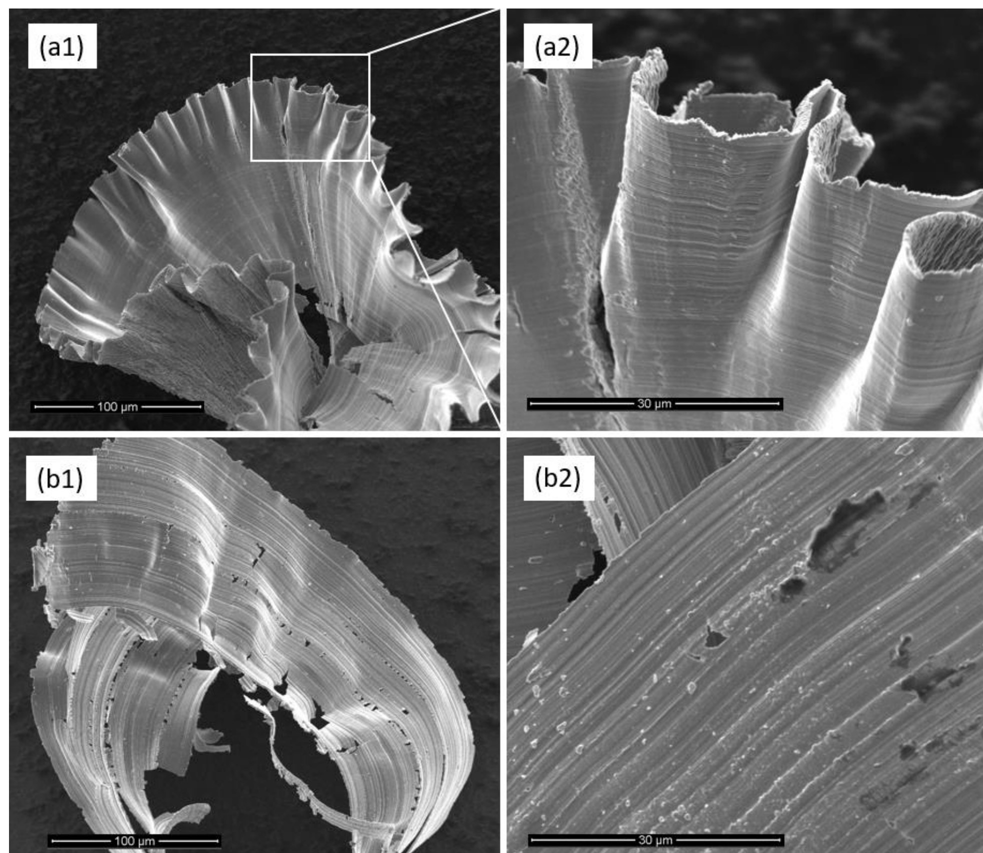

Figure 5-13: SEM micrographs of chips formed by a tool after a cutting distance of (a) 250 m, (b) 75 m at h_{max}=172 nm

By contrast, the chips generated by a tool after a cutting distance of 75 m has no edge wrinkles, as shown in Figure 5 13b. Chip wrinkling is a result of local elongation of a chip due to high strain squeezing, which is accelerated as the tool wears out. However, the high-strain band is very narrow compared with the "I" side, which is insufficient to cause chip tearing. After repetitive experiments and measurement of lengths of torn edge and chip widths as shown in Figure 5-14, it was found that chip tearing occurred only when the undeformed chip thickness is smaller than a critical value ~100 nm, which is approximately equal to the tool edge radius of a commercially available diamond tool.

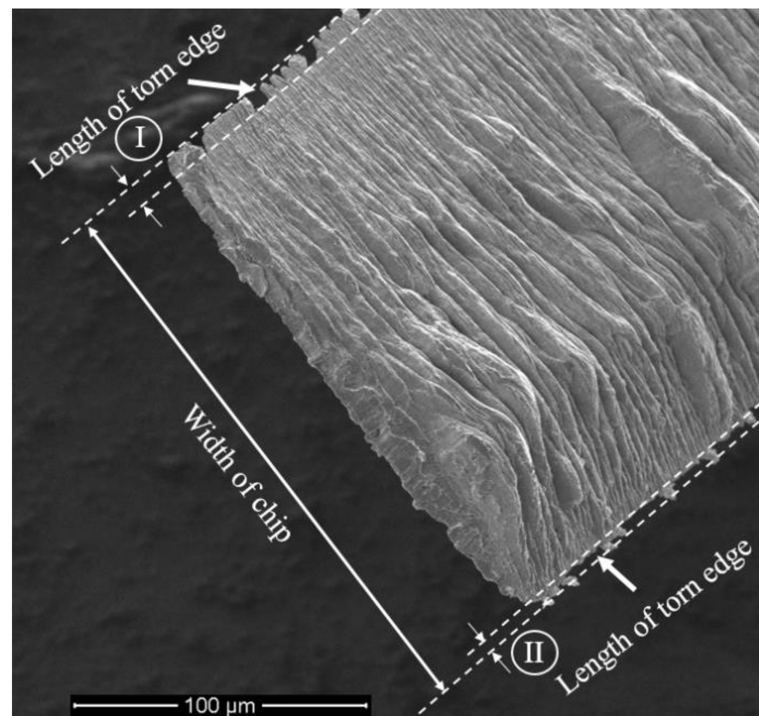

Figure 5-14: SEM micrograph of deformed chip profile (h_{max} =7405 nm)

Figure 5-15a and b show schematic illustration of undeformed chip area at two different feed rates. To calculate the length of chip edge (where the thickness is less than the desired value) on the "I" edge as shown in Figure 5-15a, first, using Eq. (2), depth of cut at which chip thickness equals the desired value can be obtained, then, this depth of cut can be applied in following equations to calculate the length of chip edge (L_1) in "I" side, as shown in Figure 5-15a.

$$L_1 = 2\pi R \times \left(\frac{\alpha + \beta}{360}\right) \tag{9}$$

$$\alpha = \arctan\left(\frac{\sqrt{2R - a^2}}{R - a}\right) \tag{10}$$

$$\beta = \arctan\left(\frac{\frac{f}{2}}{\sqrt{R^2 - (\frac{f}{2})^2}}\right) \tag{11}$$

Where *f* is feed rate, *a* is depth of cut, and *R* is tool nose radius.

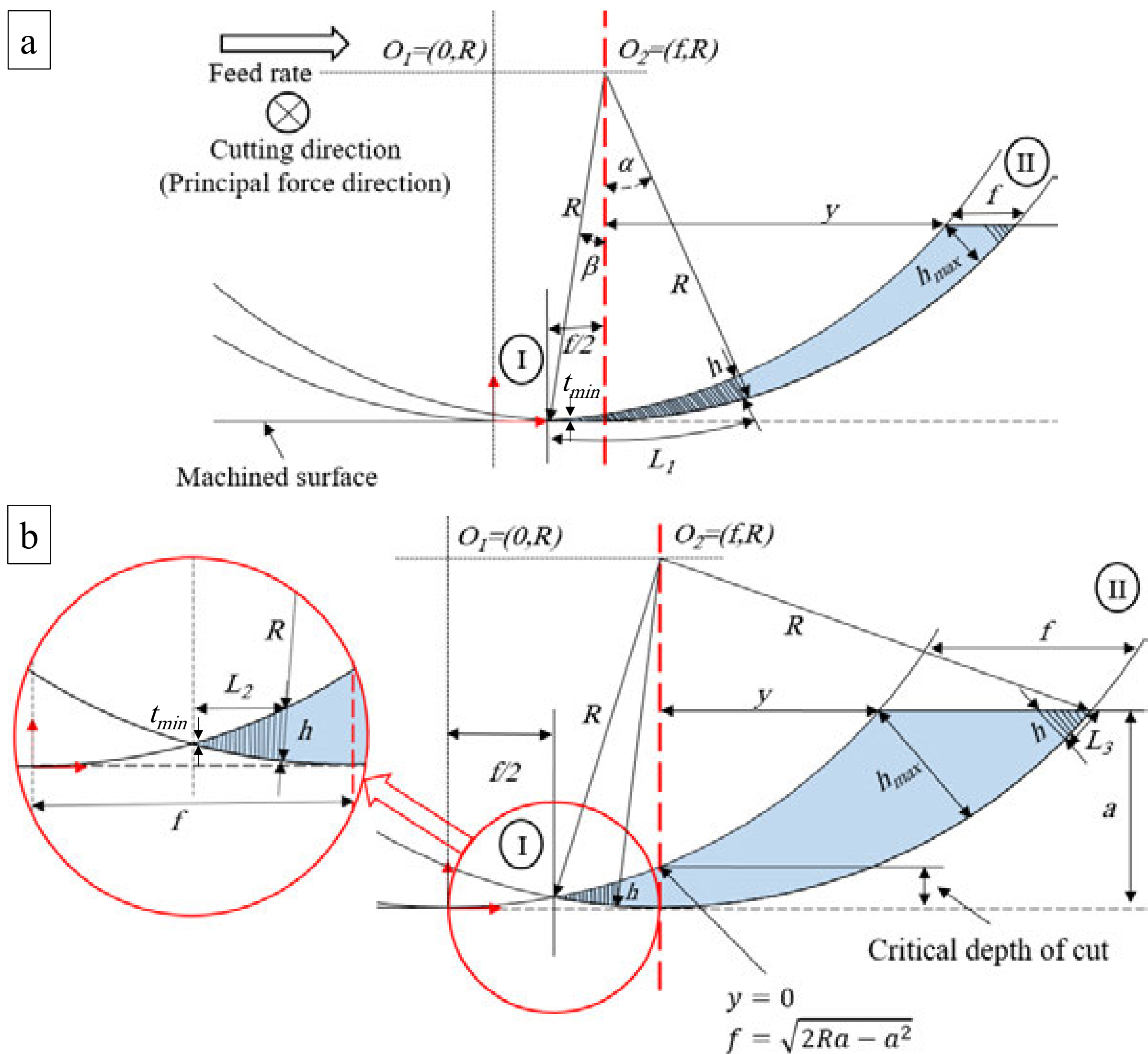

Figure 5-15: Schematic model for critical thickness on chip edges at two different feed rates

When the depth of cut calculated by Eq. (2) is less than a critical value, which is unique for every feed rate and tool nose radius, Eq. (9) is no longer valid. This critical value can be

calculated using $f = \sqrt{2Ra - a^2}$ which means y=0 and $h_{\max}$ is equal to the depth of cut (a) as shown in Figure 5-15b. This critical depth of cut at feed rate of 50 and 100 µm/rev is 1.25 and 5.0 µm, while thickness required is less than 100 nm. As a result, the starting point of edge tearing is somewhere in the left side of critical depth of cut (red dash line) as shown in Figure 5-15b. In this case length of chip edge (L_2) can be calculated using following equation.

$$L_2 = \sqrt{R^2 - (R-a)^2} - \frac{f}{2} \tag{12}$$

To calculate the length of chip edge (L_3) on the "II" following equation can be used at all feed rates:

$$L_3 = \sqrt{f^2 - h^2} \tag{13}$$

In order to calculate the total width of the chip, the target value can be set to be h_{max} in Eq. (2) and then using Eq. (9) the total width of the chip will be obtained. Under a feed rate of 1 µm/rev and a depth of cut of 5 µm, the maximum undeformed chip thickness was 99 nm, thus chip tearing occurred all over the tool edge, as shown in Figure 5-16.

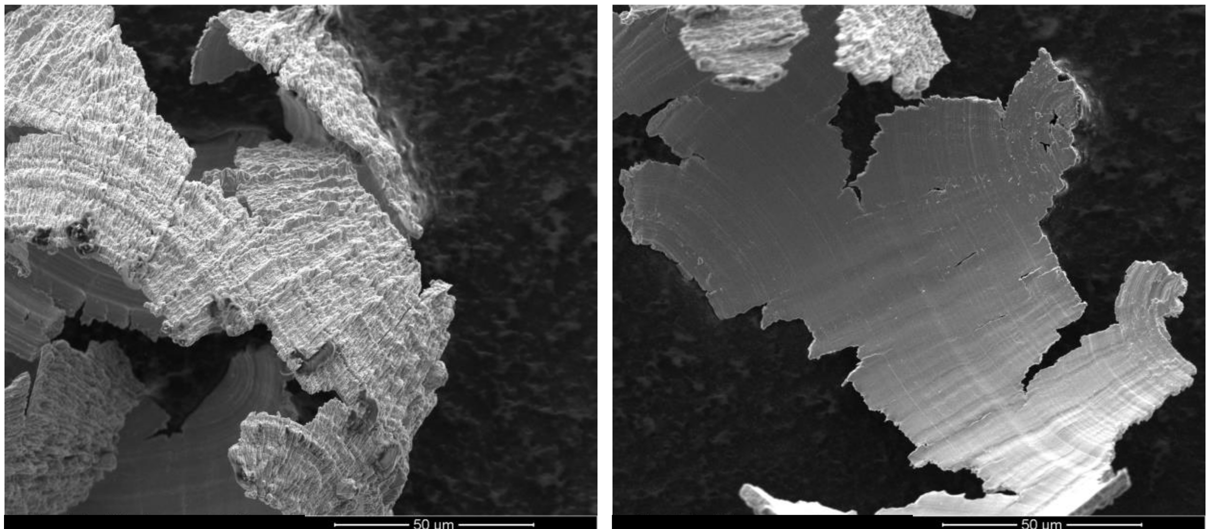

Figure 5-16: SEM micrographs of torn chip at h_{max}=99 nm

As undeformed chip thickness is further decreased below a minimum chip thickness (t_{min}), a kind of transition to plowing occurs and no chip formation takes place. To determine

the minimum uncut chip thickness experimentally, a set of experimental tests were carried out at a feed rate of 0.2 μm/rev and different depth of cuts ranging from 0.5 to 50 μm to produce a maximum undeformed chip thickness from 5 to 50 nm.

At a maximum undeformed chip thickness h_{max}=10 nm, small particles were generated, as shown in Figure 5-17a, while no continuous chips were found. As h_{max} increased to 30 nm, short continuous chips were generated lamella structure (Figure 5-17b). This result indicates that the minimum chip thickness (t_{min}) is between 10 nm and 30 nm. Longer continuous chips with regular lamella structures were observed at h_{max}=50 nm (Figure 5-17c). This indicates that when undeformed chip thickness is less than 50 nm, the workpiece material deformation is mainly plowing, where plastic deformation occurs in a broad zone rather than a shear plane. Thus, the stable formation of long and continuous chips becomes difficult, causing the aforementioned chip tearing phenomenon.

Many researchers have proposed theoretical models to determine the minimum uncut chip thickness [18,66,128–134]. Most of these models are derived on the basis of friction coefficient and tool edge radius. One of the widely used models, proposed by Son et al. [135] is shown in Eq. (14).

$$t_{min} = r \times \left(1 - \cos\left(\frac{\pi}{4} - \frac{\rho}{2}\right)\right) \tag{14}$$

Where t_{min} is the minimum chip thickness, r is the tool edge radius and ρ is the friction angle between the tool and the workpiece. The friction angle can be obtained by Eq. (15) [136]:

$$\rho = \alpha + \tan^{-1}\frac{F_t}{F_c} \tag{15}$$

Where α is rake angle (α=0 in this study); F_t and F_c are the two force components which are easily measured when the undeformed chip thickness is far larger than the tool edge radius. In this study, using the relationship of principal and thrust forces captured at h_{max}=12331 nm,

a minimum uncut chip thickness was calculated to be 10.71 nm, which is roughly in agreement with experimental results.

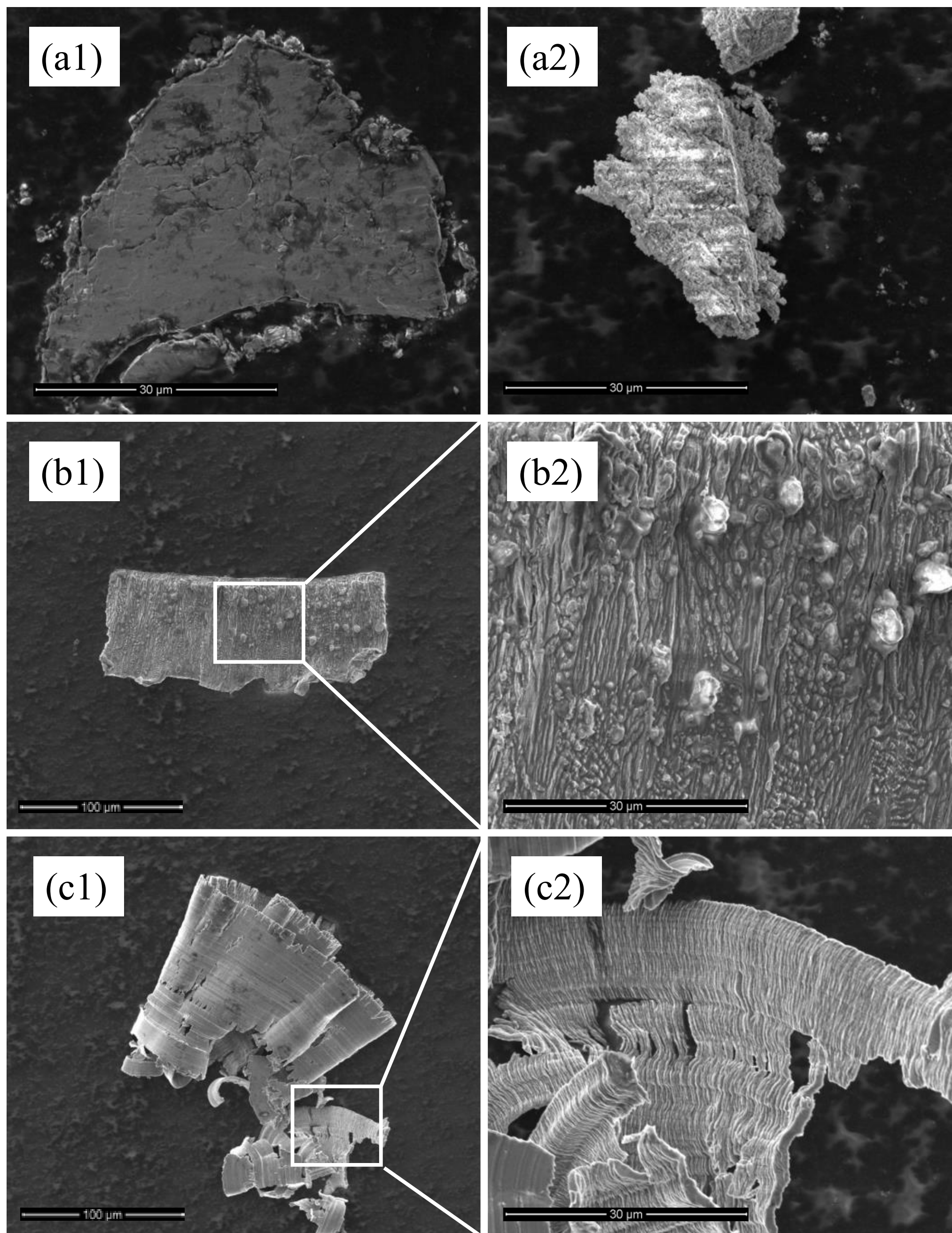

Figure 5-17: SEM micrographs of chips generated at h_{max}= (a) 10 nm, (b) 30 nm (c) 50 nm

Next, the chip tearing ratio (r_{ct}), which is the ratio of the torn parts of a chip formed under undeformed chip thickness of 100 nm to the total width of the chip, was calculated. Figure 5-18 presents the results of r_{ct} factor. The r_{ct} shows the same trend as that of specific cutting force shown in Figure 5-12, indicating the correlation between these two factors.

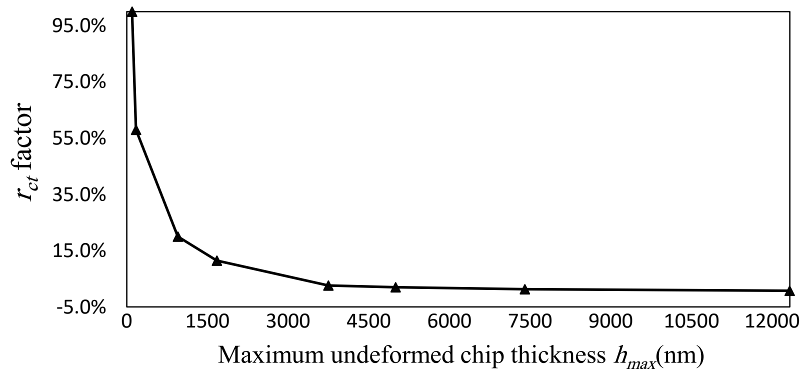

Figure 5-18: Change of r_{ct} with h_{max}

5.2.5 Pore deformation mechanism

The pores in porous titanium can be divided into two categories respecting to their sizes: pores smaller than undeformed chip thickness and pores bigger than undeformed chip thickness, the ratio of which decreases as undeformed chip thickness decreases.

Figure 5-19 is a schematic illustration of the deformation process of pores in porous titanium cutting. A square element is used to present a pore, which is deformed into a rhombus after passing through the shear plane. Figure 5-19a shows the deformation of a pore with size less than undeformed chip thickness. The pore remains inside the chip after deformation, and the ratio of *d' to d"*, which indicates pore close, decreases with the shear angle. Thus, the pores with size less than undeformed chip thickness tend to be closed due to shear deformation. The possibility of air entrainment in the chip is very low owing to the fact that most of the pores in porous titanium are interconnected. The effect of pores also depends on the depth of pore in the workpiece. Figure 5-19b illustrates two pores with the same size as that in Figure 5-19a but at two different locations. For the pore near the workpiece as indicated by "II", the pore remains in the chip as an opening on the chip surface; while for the deeper pore indicated by "III", the bottom part remains on machined surface leading to an open cavity on the surface, and the top part causes an opening on the back side of the chip. In addition to the effect of shear

deformation on deformation of the pore, the chip-tool friction has profound influences on the deformation of the pore, as indicated by pore "III". Interface friction in chip-tool contact zone causes the top part of pore "III" to be closed. Where a pore is very large, as indicated by pore "IV" in Figure 5-19c, the pore not only causes a big opening on the machined surface but also leads to chip segmentation.

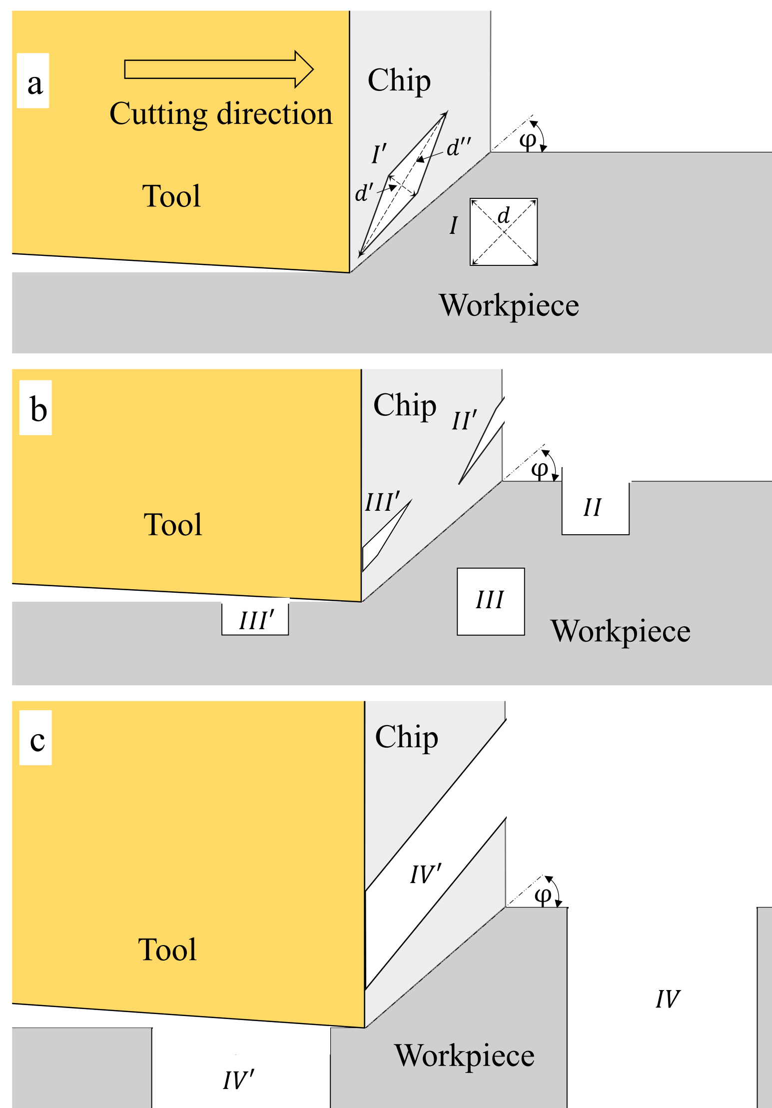

Figure 5-19: Schematic illustration of pore deformation in cutting porous titanium

Figure 5-20a and b show the back sides of chips generated in cutting of porous titanium in comparison with chips generated in cutting of pure titanium (Figure 5-20c and d). It is clear that the chips of pure titanium have very smooth surfaces, whereas those of porous titanium

are rougher and contain many opening pores and chip tearing phenomenon found in pure titanium cutting (Figure 5-20c) takes place at a small h_{max} for porous titanium too (Figure 5-20a). Compared to pure titanium chips (Figure 5-20c), the porous titanium chips are torn more significantly (Figure 5-20a), indicating that the presence of pores increases the possibility of chip tearing.

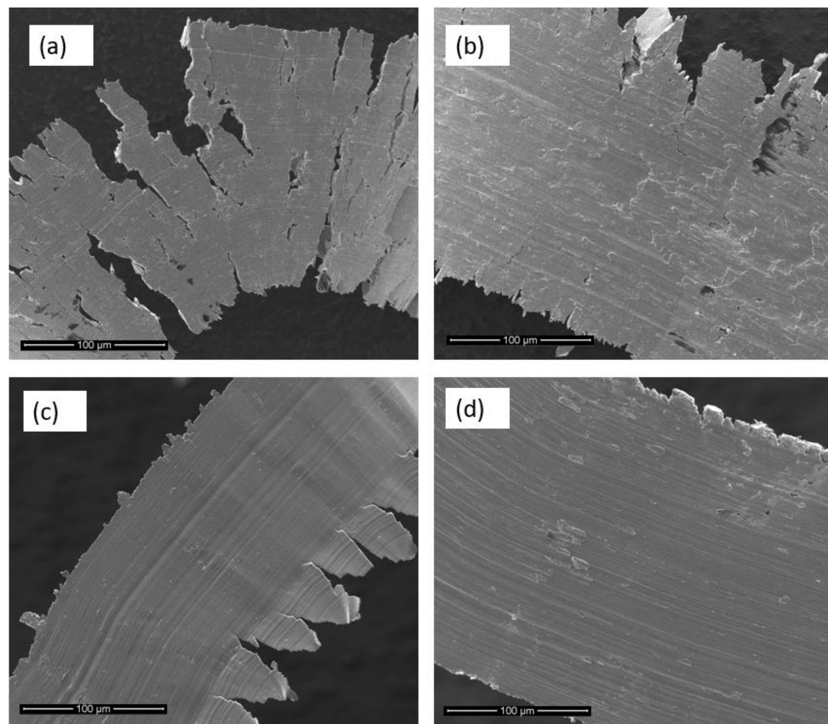

Figure 5-20: SEM micrographs of back sides of chips at (a) h_{max}=1676 nm, (b) h_{max}=12331 nm in cutting porous titanium, and (c) h_{max}=1676 nm, (d) h_{max}=12331 nm in cutting pure titanium

Differences were also confirmed on the front sides of the chips. As shown in Figure 5-21, the chips of porous titanium have sharp segments protruding from the surface. This kind of chip segmentation might have been caused by the big pores indicated by "IV" in Figure 5-19c. The pores induce big gaps inside chips which terminates shear deformation of the material. As a result, the chip will be segmented and the material will protrude out of the gap without shear deformation. Although, the segment protruding phenomenon does not occur on the back side of the chip due to chip-tool friction.

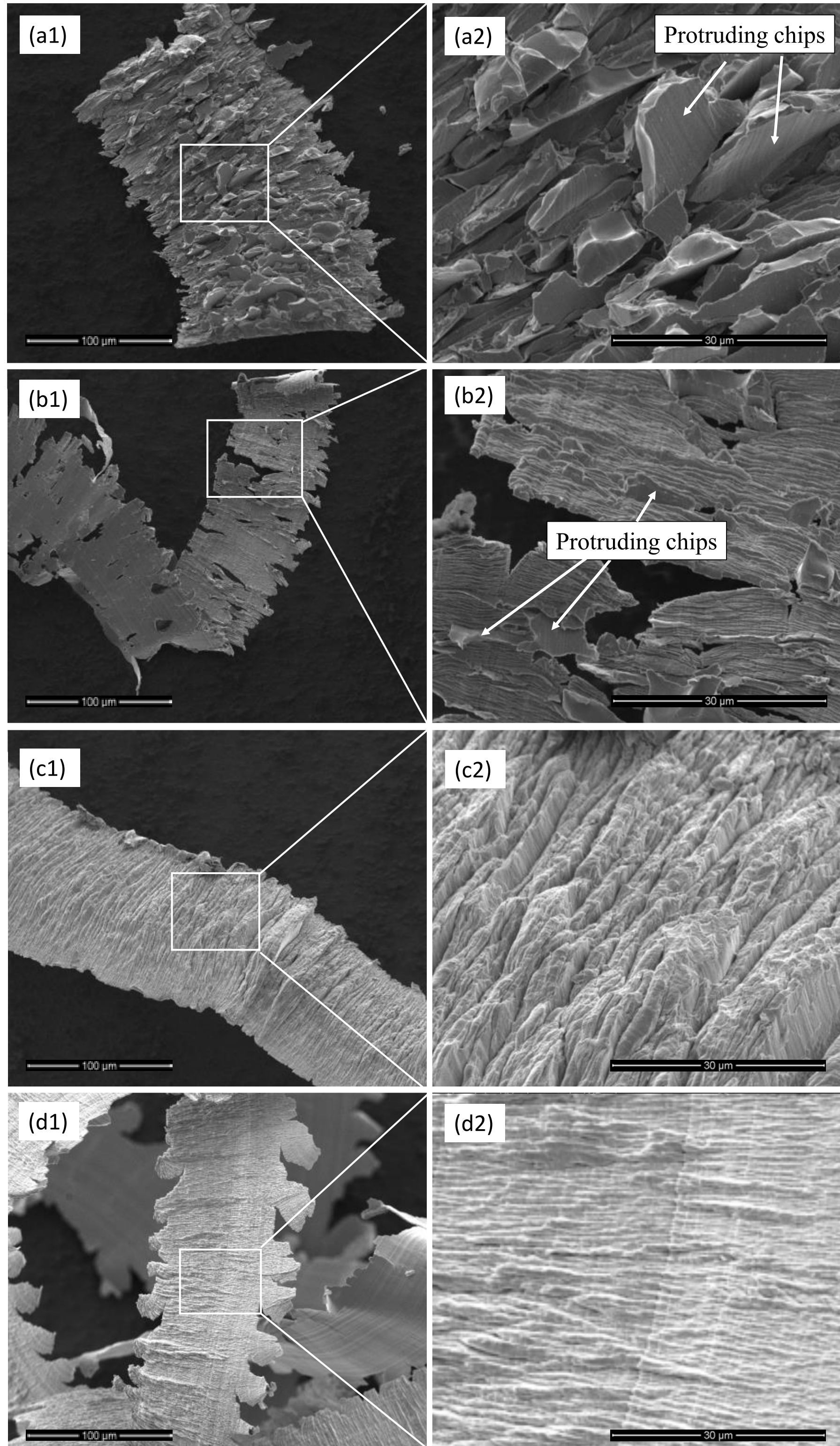

Figure 5-21: SEM micrographs of chips generated in porous titanium cutting at (a) h_{max}=4999 nm and (b) h_{max}=949 nm. For comparison, chips generated in pure titanium cutting at (c) h_{max}=4999 nm and (d) h_{max}=949 nm are also shown.

By comparing Figure 5-21a and b, it is seen that the chip segment protruding phenomenon becomes insignificant as undeformed chip thickness decreases. For pure titanium,

however, as shown in Figure 5-21c and d, the chips have regular lamella structure without segment protrusion.

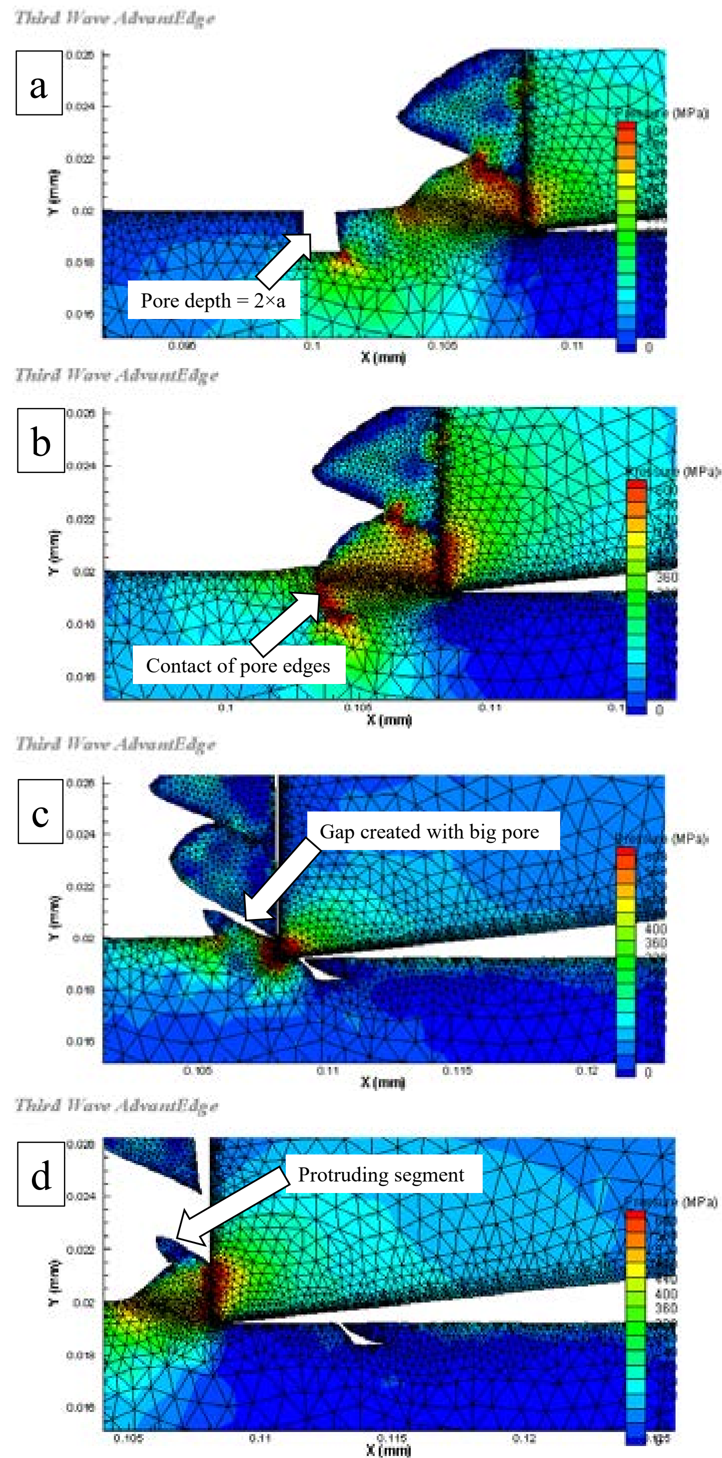

Figure 5-22: FE simulations of chip formation behavior near a pore (a=2.0×r)

Figure 5-22 shows FE simulation of cutting process near a pore the size of which is twice of the depth of cut. In the simulation, the formation of protruding chip segments can be

confirmed. As tool tip feeds toward pore, the deformation occurs on pore edge close to the tool, while another edge is not influenced (Figure 5-22a and b). This results in a kind of disorder in continuous chip generation and induces a big gap inside chips which terminates shear deformation of material leading to the protruding material out of the gap (Figure 5-22c and d).

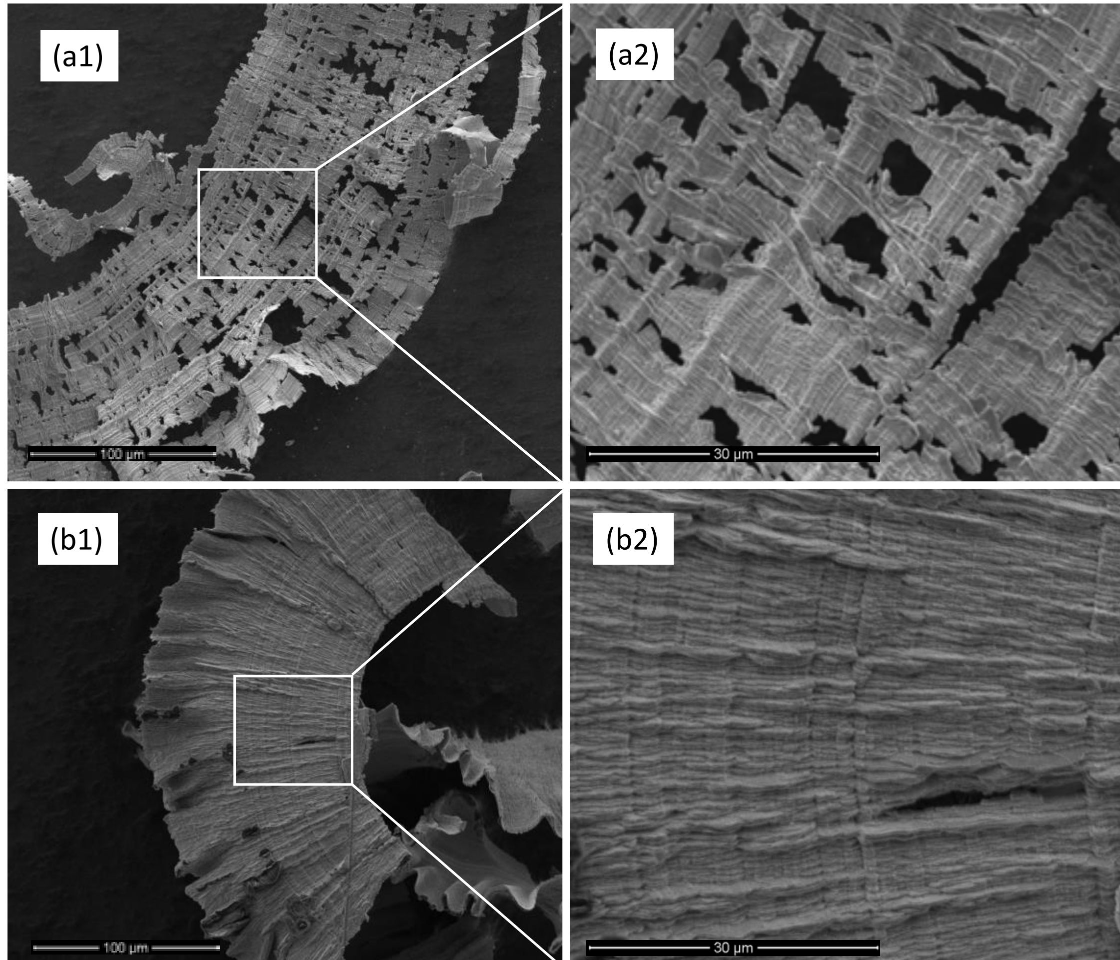

Figure 5-23: SEM micrographs of front sides of chips of (a) porous titanium and (b) pure titanium at the same undeformed chip thickness (h_{max}=172 nm)

As undeformed chip thickness decreases to the nanometer scale (h_{max}=172 nm), the effect of pores on chip formation has become more obvious, as shown in Figure 5-23a. Chip tearing in porous titanium cutting are more significant than those in the cutting of pure titanium. The pores might become sources for chip tearing. The chip tearing phenomenon has a remarkable impact on machined surface topography at extremely small h_{max}.

5.2.6 *Machined surface topography*

Surface roughness was measured in machined pure titanium in three-dimensional forms in which the average arithmetical deviation of the area (S_a) was calculated by using the TalyMap software. The S_a data recorded according to feed rate and depth of cut during experiments are presented in Figure 5-24. From this figure, it can be seen that S_a decreases as undeformed chip thickness decreases. A surface roughness of 47 nm was obtained at a feed rate of 10µm/rev. However, an inverse trend is observed at a feed rate lower than 10 µm/rev.

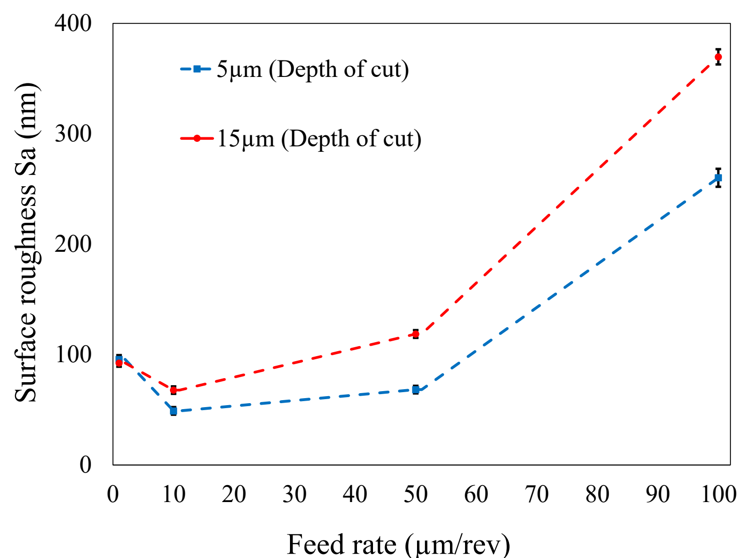

Figure 5-24: Surface roughness (Sa) of machined surface at different feed rates and depth of cuts

In order to find out the reasons for the changes in S_a, SEM observations and three-dimensional topography measurements of machined surfaces were performed for each cutting condition. Figure 5-25 shows SEM micrographs and three-dimensional topographies of machined surfaces at three different feed rates. At high feed rate (100 µm/rev), the surface roughness is attributed to the feed marks. When the tool feed rate is smaller than 10 µm/rev, however, no tool feed marks are seen. The surface roughness is due to non-periodical unevenness and surface protrusions.

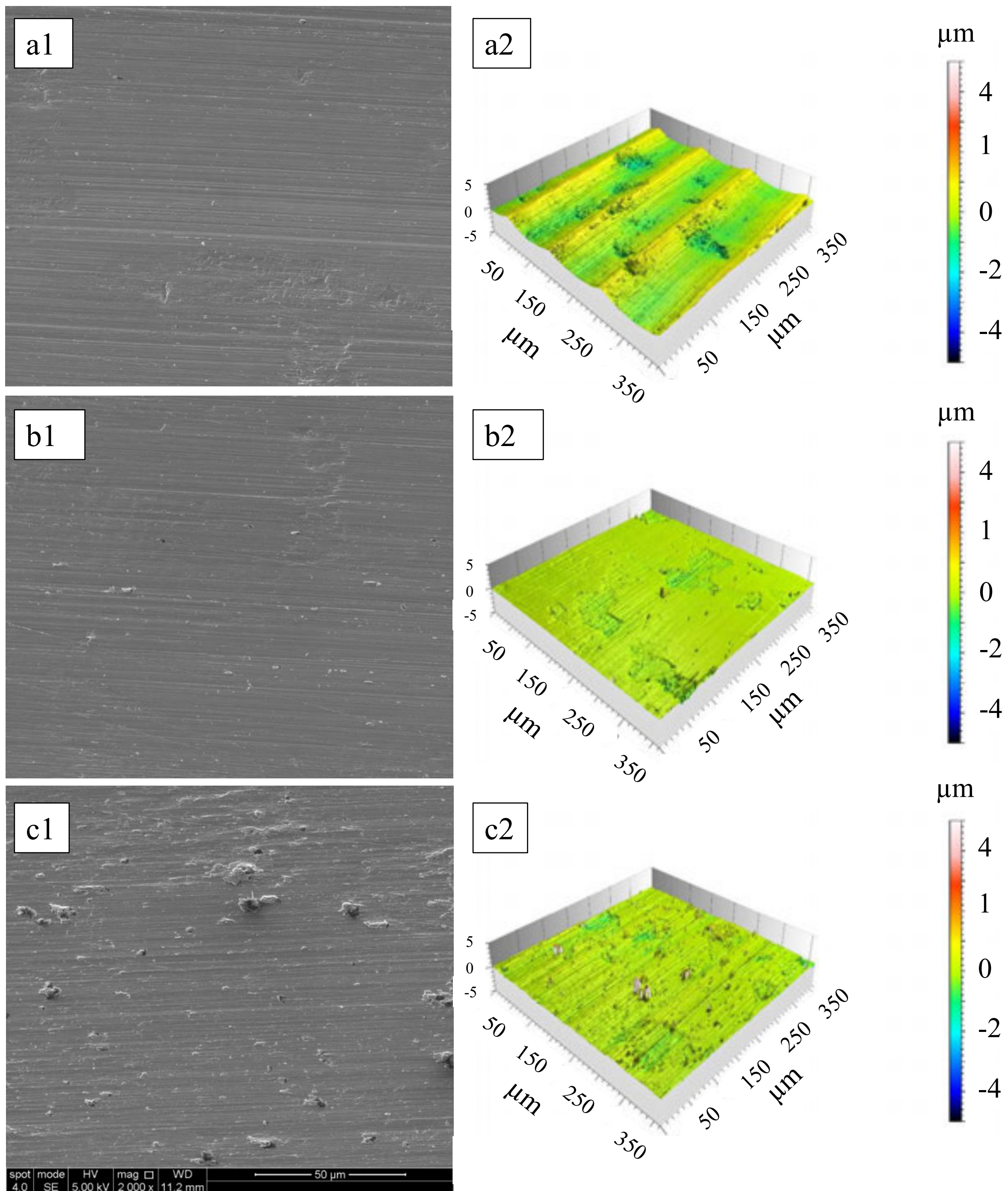

Figure 5-25: SEM micrographs and three-dimensional surface topographies of machined surfaces at ((a1) and (a2)) f=100 µm/rev (h_{max}=12331 nm); ((b1) and (b2)) f=10 µm/rev (h_{max}=1676 nm); ((c1) and (c2)) f=1 µm/rev (h_{max}=172 nm)

Further examinations of machined surface samples show that apart from tool feed marks, there are other types of features influencing surface roughness, including material plucking from workpiece surface, debris, scratches, and adhered chips. As shown in Figure 5-25, extremely small debris and scratches are observed under all different feed rates.

Plucking of material from a surface is observed at a higher feed rate (Figure 5-26a), whereas chip adhesion was observed remarkably on machined surface at lower tool feed rate (Figure 5-26b).

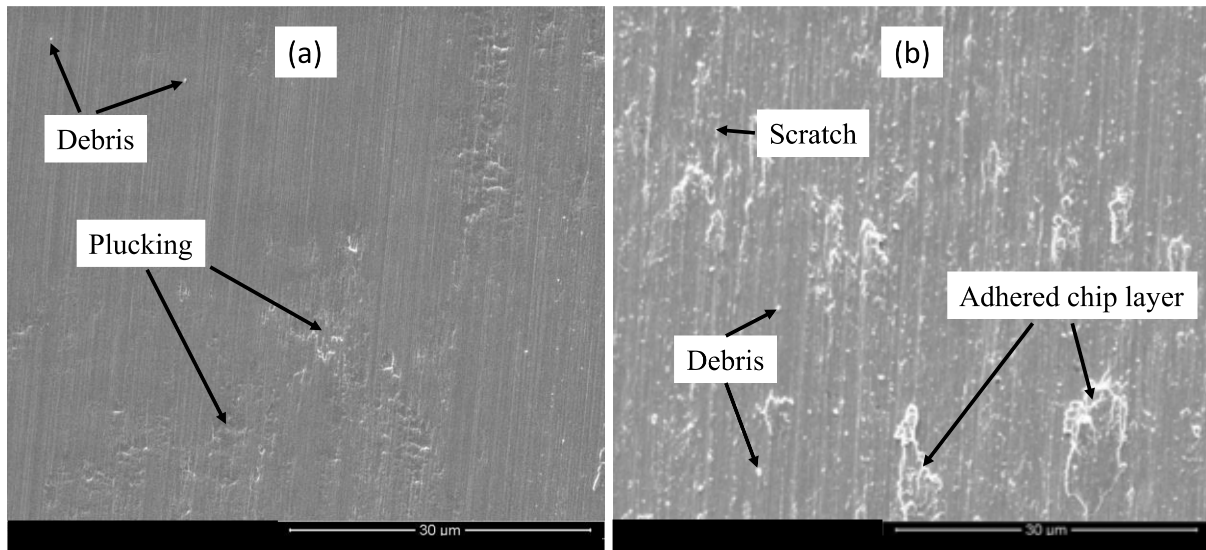

Figure 5-26: SEM micrographs of machined surfaces at (a) h_{max}=12331 nm and (b) h_{max}=172 nm

There might be two reasons for plucking. First, a small part of workpiece material was peeled off from its original surface by the flank face of the tool. Second, built-up edges were formed which produces unstable cutting and deep material removal [54]. Scratches might be a result of replication of the micro-chippings on the tool edge. The adhered chips on the machined surface are presumably due to the chip tearing phenomenon, as described in Section 5.2.4. Due to the high pressure toward the workpiece surface at an extremely small undeformed chip thickness, a part of material cannot be completely removed as a chip, and instead, remained on the surface as material adhesion. In addition, debris on the machined surface might also be a part of material separated from torn chips.

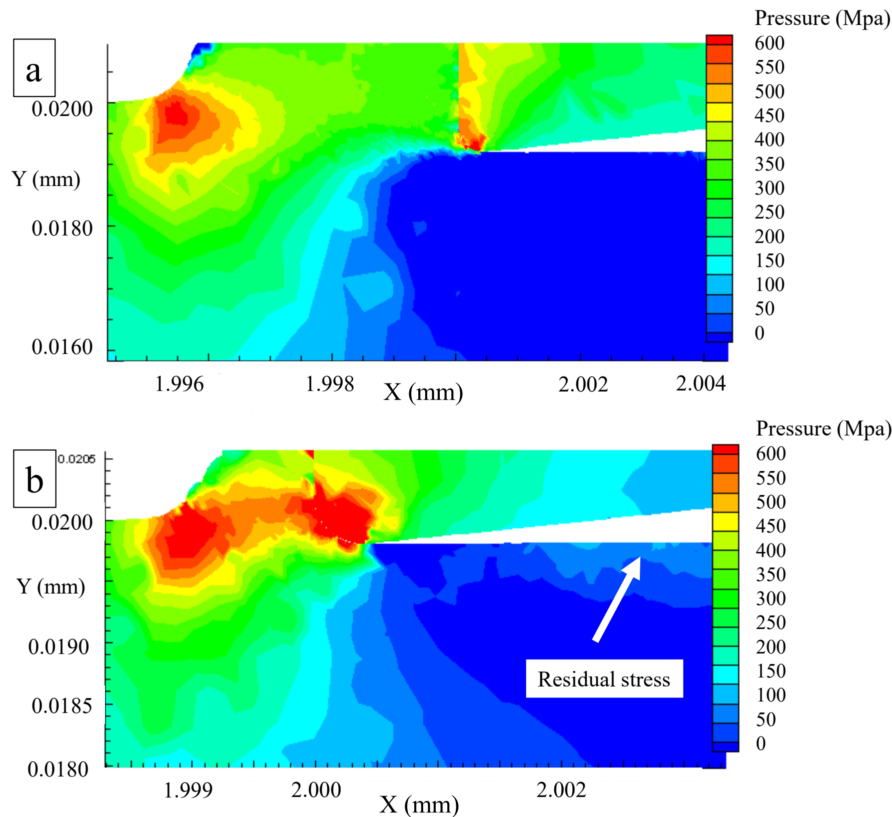

Figure 5-27: FE simulation of pressure distributions at (a) a=2.0r and (b) a=0.5r

To illustrate the effect of high pressure on the deposition of torn chips on the machined surface, FE modeling were performed at two different depth of cuts. At a large depth of cut (Figure 5-27a), the high pressure only exists in small regions of the chip. At a small depth of cut (Figure 5-27b), however, cutting pressure affects all chip thickness. Such a high pressure acting at very fine chip thickness provides a condition for some parts of chips to stick on the surface.

Figure 5-28 shows the back side of a chip formed at h_{max}=172 nm. Some parts of the chip have been detached, leaving holes on the chip. The detached parts of chips might become debris or chip adhesion onto the machined surface.

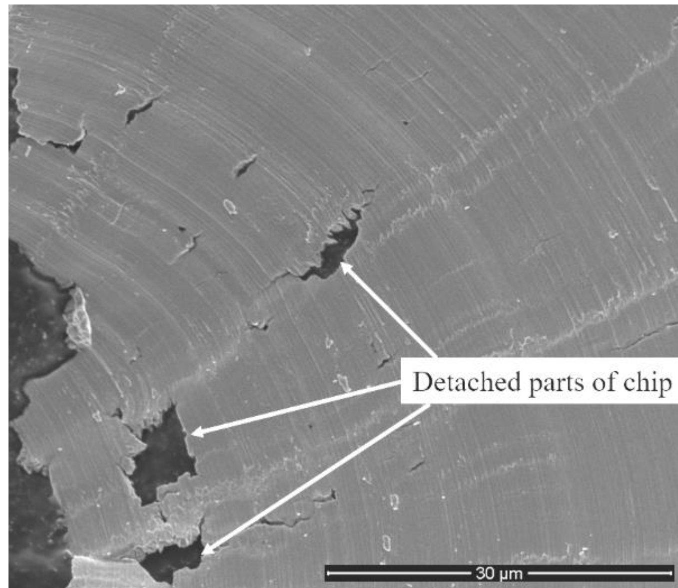

Figure 5-28: SEM micrograph of the detached parts of a chip

Figure 5-29 shows SEM micrographs of the machined surface of porous titanium. It is seen that as h_{max} decreases, more pores are closed. At an extremely small h_{max} (172 nm), almost no open pores are observed on the machined surface (Figure 5-29c). Analyzing the SEM images using ImageJ software indicates a surface porosity of ~29% at $h_{\max}$ =12331nm. Figure 5-30 shows an example of SEM image processed to calculate the area ratio of surface pores by the ImageJ software. However, the surface porosity decreases to ~1% at $h_{\max}$ =172 nm as shown in Figure 5-31.

Two factors might have affected the phenomenon of pore closing: the high shear stress induced by tool edge, and chips embedding into the pores. The tool-induced high shear stress causes the extensive plastic flow of material beneath the tool edge, leading to pore closing (Figure 5-27). The detached parts of chips might enter the pores and embedded after tool pass, causing pore closing.

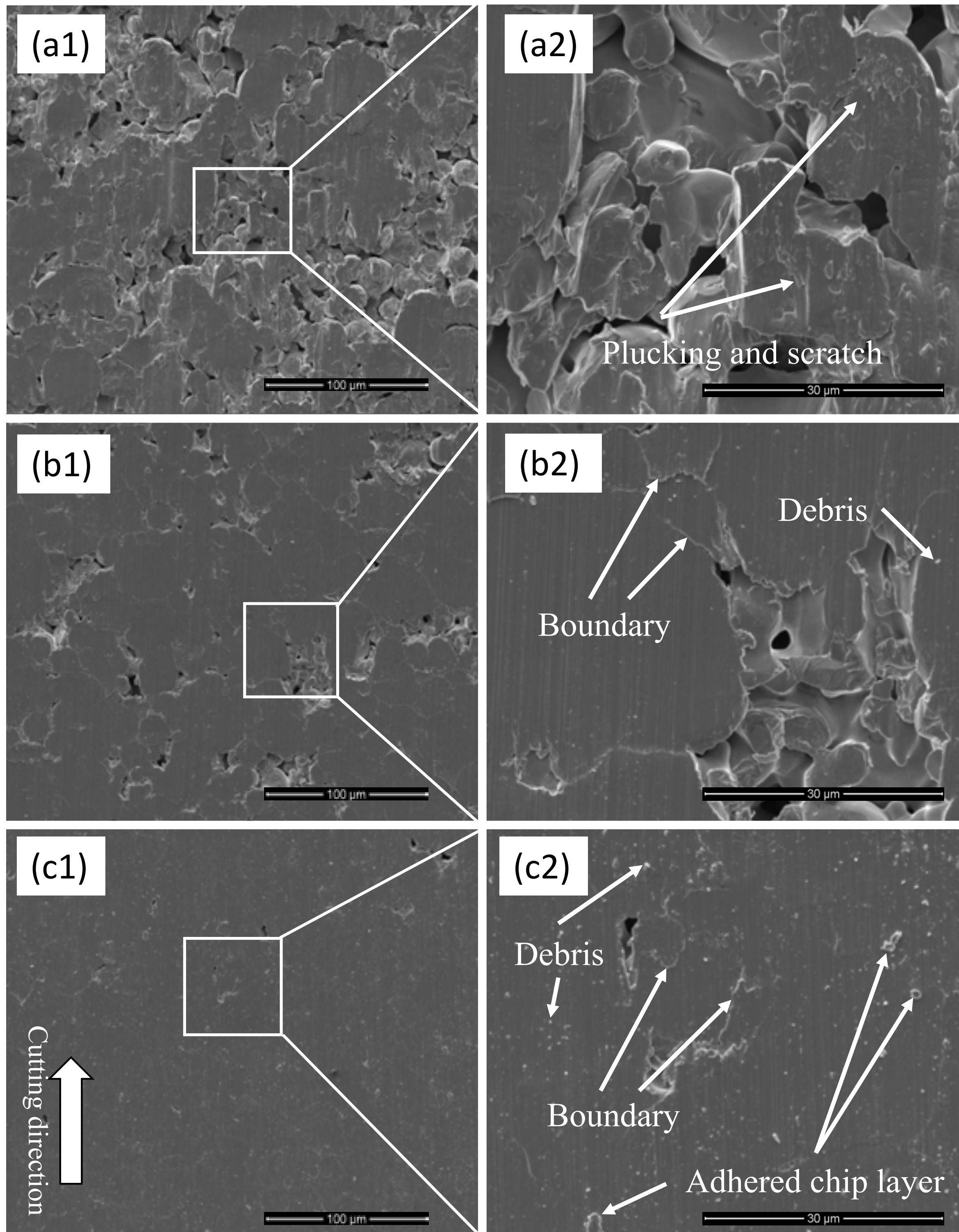

Figure 5-29: SEM micrographs of machined surface of porous titanium at (a) h_{max}=12331 nm, (b) h_{max}=1676 nm, and (c) h_{max}=172 nm

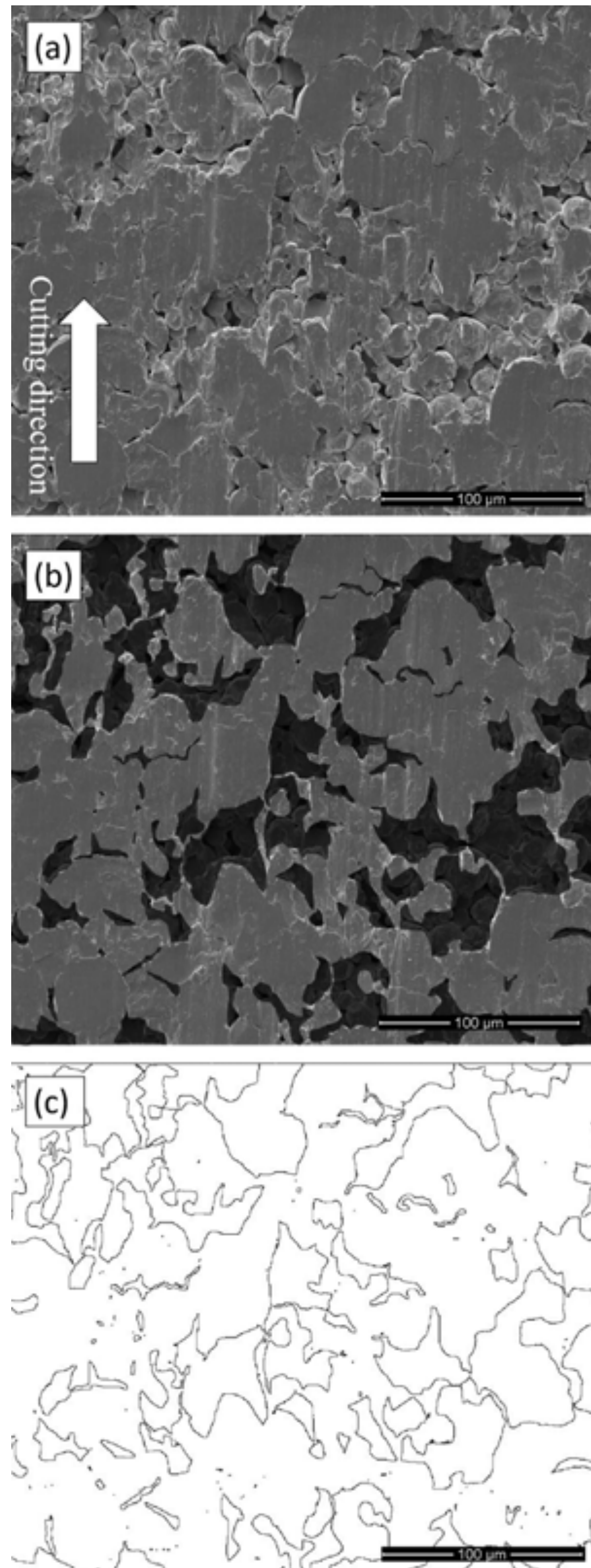

Figure 5-30: Image-processed results for calculating surface porosity on the machined surface of porous titanium at h_{max} =12331 nm

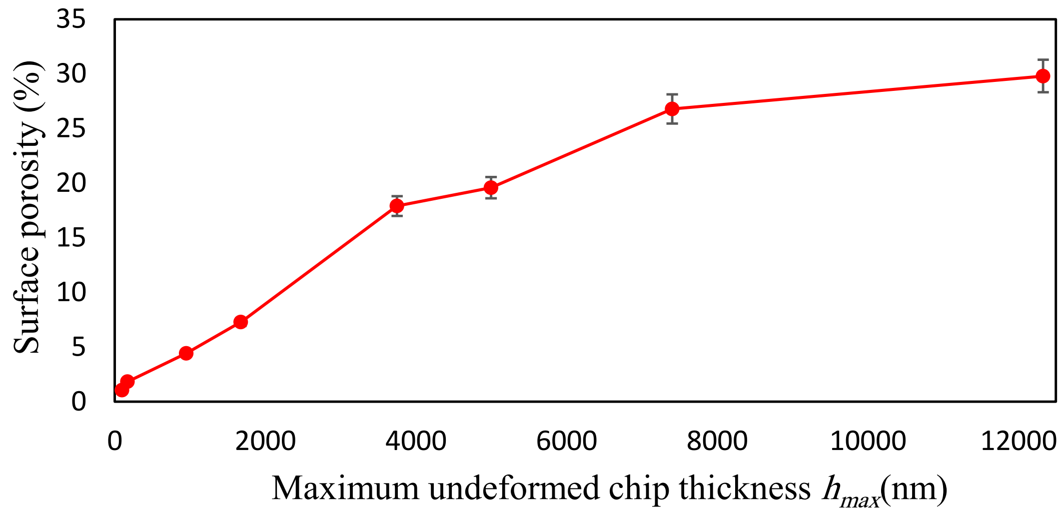

Figure 5-31: Change of porosity percentage with h_{max}

Figure 5-32 shows FE simulations of cutting behavior around a square-shape pore at two different depths of cuts (a). In this case, the pore is 5 times bigger than the tool edge radius (*r*). When the tool tip feeds toward an edge of a pore at extremely small undeformed chip thickness (Figure 5-32a), the tool-induced high pressure pushes the chip to reach the other side of the pore where interfacial welding phenomenon occurs, which agrees with the experimental results (Figure 5-29b2 and c2). The torn chip accelerates the process entering chip into pores and welding phenomenon. At higher undeformed chip thickness, however, welding phenomenon does not occur due to the fact that chip generated is more uniform and stress is not concentrated compared to low undeformed chip thickness, thus pores remain open, as shown in Figure 5-32b. The welding phenomenon occurring in cutting porous titanium may justify the reason why there is no significant difference in cutting forces between pure titanium and porous titanium at extremely fine undeformed chip thickness (Figure 5-4).

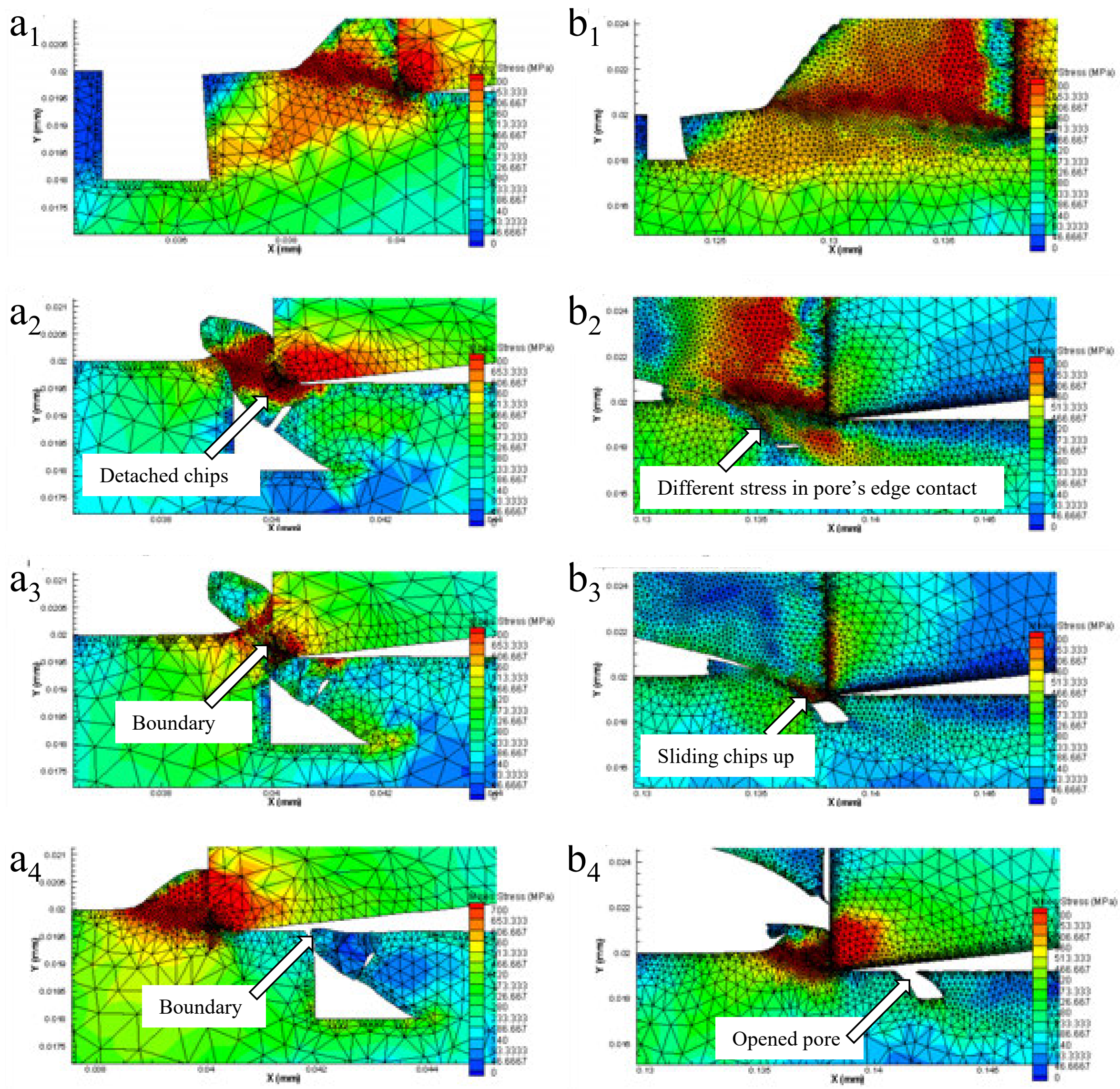

Figure 5-32: FE simulations of cutting behavior near pores at (a) $a=r$ and (b) $a=2r$

5.2.7 *Coolant effects*

Figure 5-33 shows the results of cutting force measurements during machining of both pure titanium and porous titanium in wet cutting using coolant. Compared with dry cutting (Figure 5-4), wet cutting decreases cutting force slightly.

The use of coolant might have two double-face effects on cutting force. One is the lubrication effect, i.e., the coolant can penetrate the pores and lubricate both the tool-workpiece interface and the shear deformation zone along the shear plane, and in turn, decreases cutting

forces. The other is the cooling effect on work hardening, which increases cutting forces. Large-strain deformation enhances strength and hardness in machining titanium [137]. This work hardening process will be affected by temperature, so that resulting surface hardness will change with temperature. Using coolant causes rapid cooling and enhances the work hardening effect. Figure 5-34 shows a schematic model for coolant effects on cutting process.

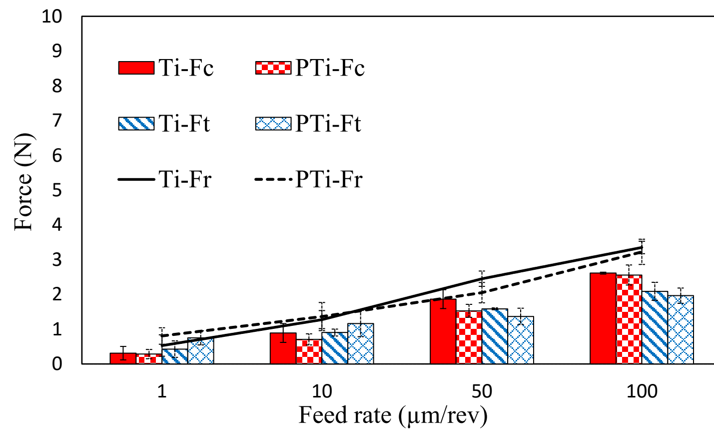

(a)

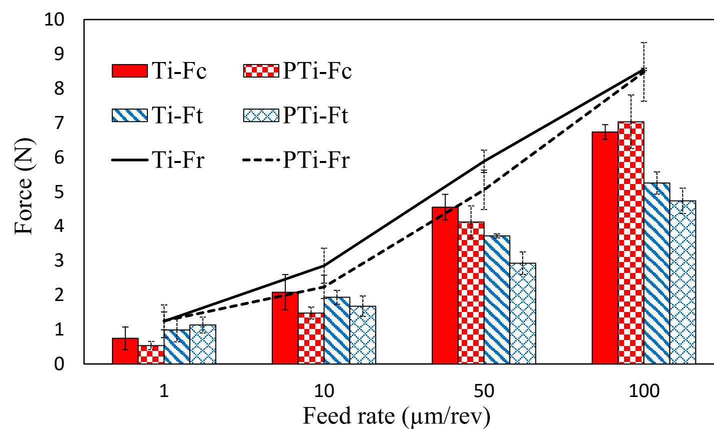

(b)

Figure 5-33: Cutting forces of pure titanium (Ti) and porous titanium (PTi) in wet condition at depth of cut (a) 5 μm and (b) 15 μm

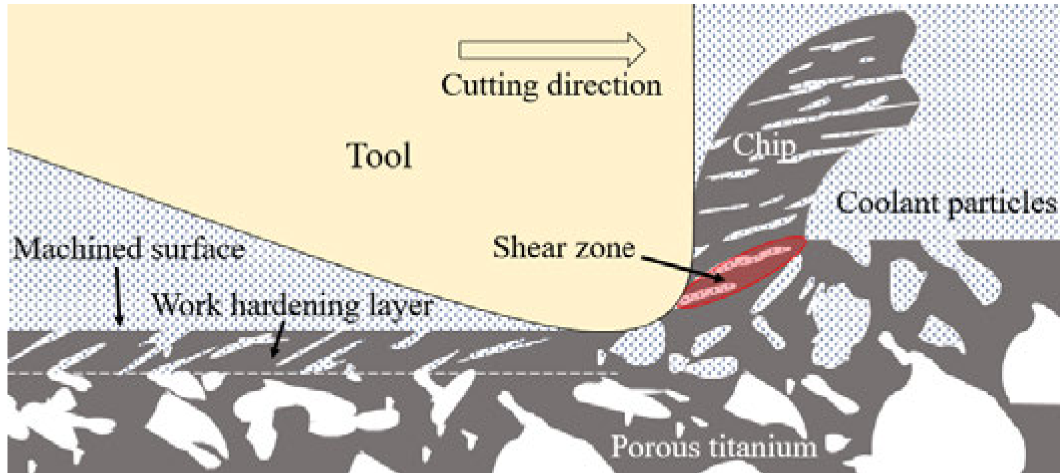

Figure 5-34: Schematic illustration of coolant effects

Table 5-3 shows the results of micro Vickers hardness for the machined surface of pure titanium at different depths of cuts. The results show that cutting process at low undeformed chip thickness has great influences on the subsurface microstructure of workpiece. As shown in Figure 5-27b, decreasing depth of cut will increase residual stress on a machined surface. As shown in Table 5-3, the Vickers hardness exhibits a 15% to 30% increase after machining compared to that before machining.

Table 5-3: Vicker hardness (HV) of machined surface

	a \ f	1 μm/rev	10 μm/rev	50 μm/rev	100 μm/rev
Ti-Dry	15 μm	173.1	181.1	181.2	189.4
Ti-Coolant		175.8	191.1	197.2	191.1
Increase%		1.6	5.5	8.8	0.9
Ti-Dry	5 μm	182.2	192	185.3	189.1
Ti-Coolant		183.4	193.5	192.9	190.9
Increase%		0.7	0.8	4.1	1.0

In addition, the results demonstrate that up to 8.8% increase in surface hardness occurs after wet machining. This phenomenon might be explained by the effect of coolant on cooling rate of the machined surface. Kitagawa et al. (1997) recorded a temperature between 800 to 900°C in cutting area during continuous cutting of titanium alloys at a cutting speed of 50

m/min. After tool passes, the coolant penetrates the fresh surface and increases the cooling rate that may increases surface hardness.

5.2.8 *Tool wear and material adhesion*

Figure 5-35 shows SEM micrographs of the tool after cutting of titanium for a cutting distance of 75 m and 250 m. The h_{max} was changed from 99 nm to 12331 nm during this cutting distance, 96% of the cutting distance was performed at a maximum undeformed chip thickness of less than 500 nm. As shown in Figure 5-35a, after just 75 m cutting, chips were welded to the tool rake face. In nanometer-scale ultraprecision machining, pressure significantly increases compared to traditional machining, which promotes material adhesion on the tool. As the cutting distance increases (Figure 5-35b), both the rake and flank faces are covered by titanium adhesion, although the appearances of adhesion are different. At the same time, built-up edges are found on the rake face side. Small flank wear lands and a few micro chippings are also observed around the tool edge. As tool wear increases, tool edge geometry will change, leading to change in chip morphology, as shown in Figure 5-13.

Figure 5-35b1 further shows that the width of flank wear land increases from the right side to left side. As shown in Figure 5-10, the left side of tool corresponds to the small undeformed chip thickness area ("I" in Figure 5-10), where flank face wear is significant. For the right side corresponding to "II" in Figure 5-10, material adhesion on rake face is more significant. With increasing tool wear, the tool-workpiece contact area is increased due to reduced clearance angle, which creates more rubbing of the workpiece surface [52]. The built-up layer that is formed on the tool flank face can push the tool off from its original route to increase the surface roughness [139].

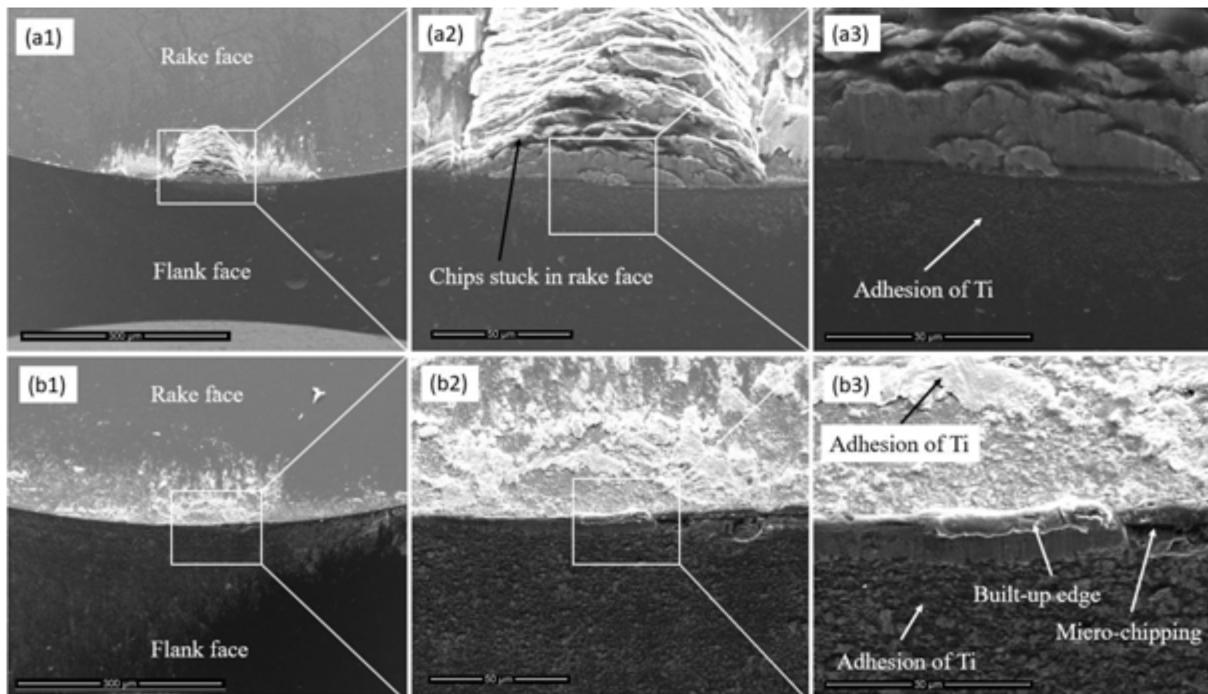

Figure 5-35: SEM micrographs of tool after a cutting distance of (a1~3) 75 m and (b1~3) 250 m

Figure 5-36 is the SEM micrographs of the tool edges after cutting of porous titanium for a cutting distance of 100 m. As shown in Figure 5-36a, material adhesion on tool face in porous titanium cutting is lower than those in pure titanium cutting. This might be due to the lower density of porous structure and the lower contact pressure at the tool-workpiece interface. Using a coolant helps to lubricate the interfaces between rake face and chips, flank face and machined surface, and thus decreases the quantity of material adhesion on these tool faces, as shown in Figure 5-36b. Nevertheless, the coolant cannot penetrate into the tool tip region during the cutting process due to the high cutting speed, thus the material adhesion near the cutting edge (tool tip) is almost the same.

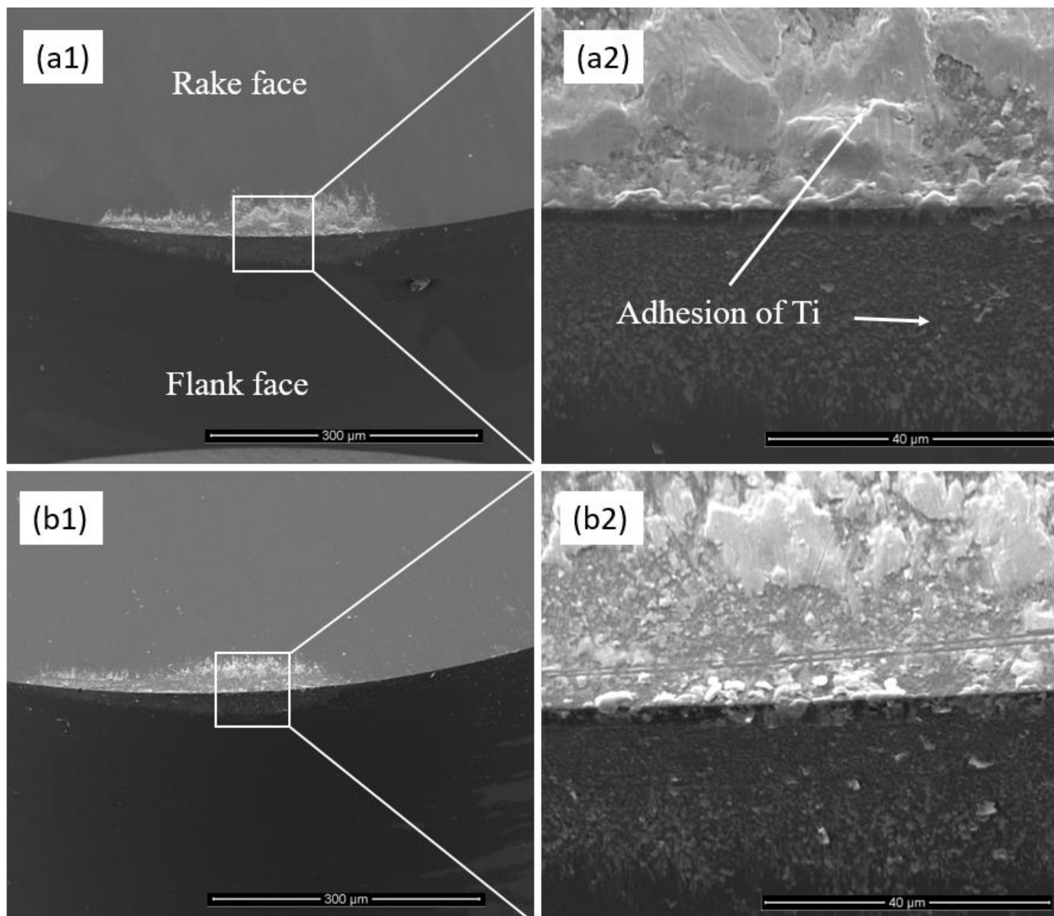

Figure 5-36: SEM micrographs of tool tip in cutting of porous titanium for a cutting distance of 100 m at (a) dry (b) wet conditions

In order to investigate tool wear characteristics in porous titanium cutting, the tools were observed for different cutting distances. Before observation, in addition to washing in alcohol, tools were cleaned using an ultrasonic cleaning with acetone to remove any adhering debris.

As shown in Figure 5-37a, a micro chipping was observed after a cutting distance of 1 km in dry cutting. The cutting distance for micro chipping occurrence is longer than that of pure titanium cutting in the same condition (Figure 5-35b). Next, experimental tests were repeated in a wet condition by applying the coolant. Observations showed that material adhesion on tool faces sharply decreased compared to dry cutting (Figure 5-37b).

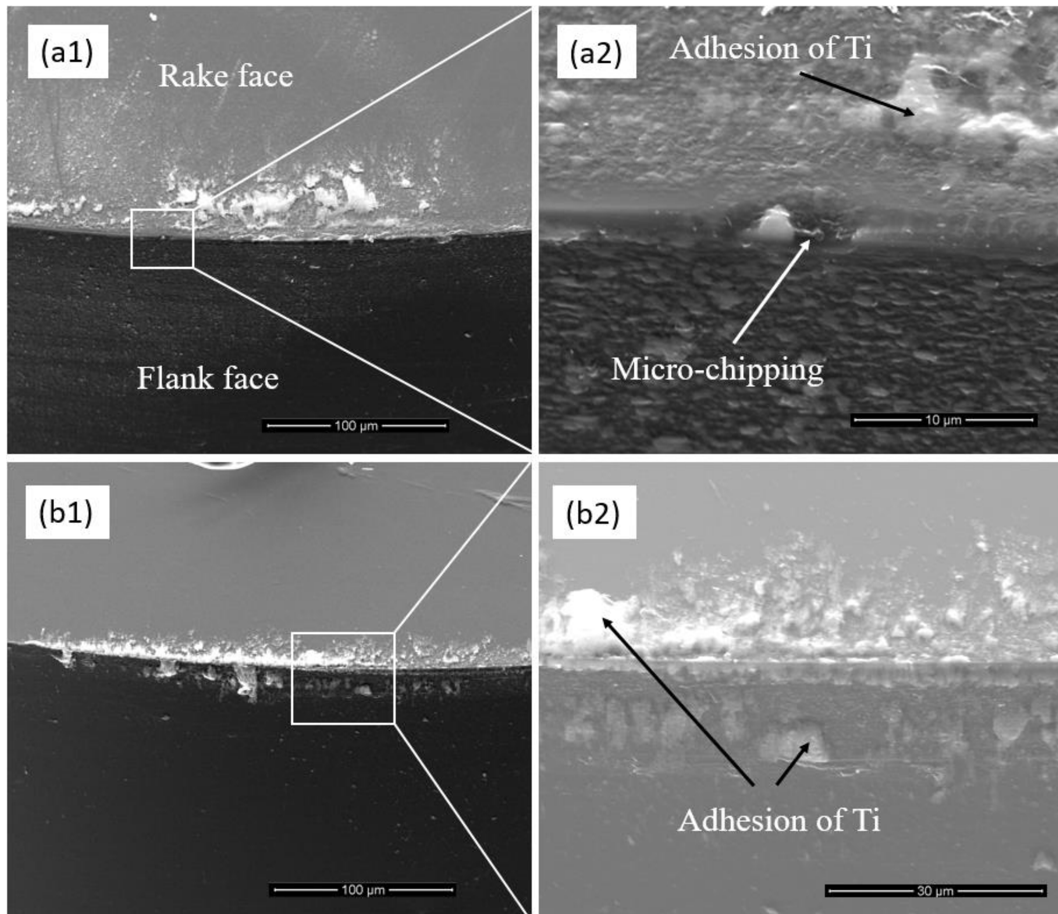

Figure 5-37: SEM micrographs of tool tip in cutting of porous titanium for a cutting distance of 1 km at (a) dry (b) wet conditions

As cutting distance increases to 2 km (Figure 5-38), the process of forming built-up-edge led to extensive micro chippings and premature failure of the tool. That means the more pores were closed due to higher pressure induced by the dull tool tip during the cutting process. Moreover, the debris adhesion also increased.

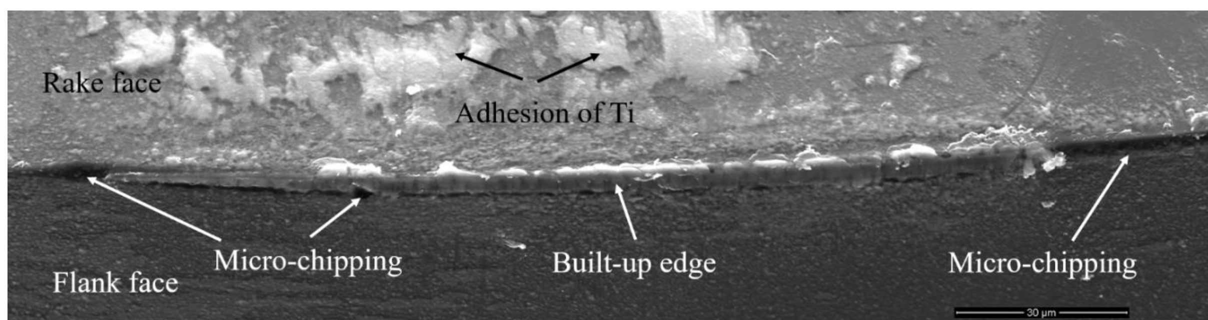

Figure 5-38: SEM micrographs of tool tip in cutting of porous titanium for a cutting distance of 2 km at dry condition

The results demonstrate that the tool wear in nanometer-scale cutting is concentrated to tool edge, which is different from micrometer-scale cutting where flank wear land and crater wear on rake face are dominant [66,140,141].

Yang and Richard [40] indicated the high stress generated in machining titanium is one of the main reasons for the rapid wear of tools. Zlatin and Field [142] have found that titanium chips have a strong tendency to weld to the cutting edge, particularly after the tool starts to wear. A localized region of high pressure at the tool-workpiece interface also increases the reactivity of titanium. The wear of a diamond tool is attributed to graphitization of diamond [46,55,143,144]. Qian et al. [145] proved that contact pressure is an important parameter for diamond-graphite transformation. Liu et al. [146] reported that TiC synthesis occurs when titanium and graphite are interacted under high temperature and pressure.

5.3 Conclusions

The mechanism of cutting and surface integrity in the ultraprecision diamond turning of both pure and porous titanium were investigated by both experiments and FE simulation under various conditions. The following conclusions were obtained:

(1) There are remarkable changes in shear angle (around 90% decrease) and specific cutting force (about 300% increase) as undeformed chip thickness decreases from the micrometer scale to the nanometer scale.

(2) As unformed chip thickness decreases down to a critical value (~100 nm), chip edge tearing becomes significant. The ratio of chip tearing shows the same trend as the specific cutting force.

(3) At an extremely small undeformed chip thickness, tool feed marks is no longer a major factor of surface roughness. Instead, material plucking from workpiece surface,

debris, scratches and chip adhesion become important factors. Chip tearing is the main reason for debris generation and chip adhesion.

(4) The Vickers hardness of workpiece surface exhibits a 15% to 30% increase after machining compared to that before machining.

(5) The presence of pores significantly changes mechanism of cutting in porous titanium compared to pure titanium. The chip morphology and surface topography depend on pore size and location.

(6) At an extremely small undeformed chip thickness, pores smaller than undeformed chip thickness will be closed due to the shear deformation inside chips, while larger pores cause segmentation of chips and protruding lamella. Pores also act as sources for chip tearing and crack propagation.

(7) As undeformed chip thickness decreases, most pores will be closed on the machined surface due to the welding phenomenon, leading to an average porosity drop from ~30% to 1%. Larger pores, however, will remain open on machined surface at a larger undeformed chip thickness.

(8) The use of coolant has two double-face effects on cutting force. Coolant penetrates the pores and lubricates the tool-workpiece interface and the shear deformation, and in turn, decreases cutting forces. Using coolant also causes rapid cooling, enhances the work hardening effect and increase machined surface hardness.

(9) Flank wear, micro chipping and material adhesion on tool surfaces are significant when cutting distance increases, and the significance of each depends on the position on the tool edge. Tool wear in cutting porous titanium is suppressed compared with that of pure titanium, especially in wet cutting.

CHAPTER 6

General modelling

(For porous material machining)

Chapter 6 : General modelling

6.1 Introduction

Three types of porous materials have been investigated in this study to cover two different material removal mechanisms in the porous materials machining process. Although it is difficult to present a general model for machining of all porous materials due to feature diversity, cutting mechanisms and surface integrity can be classified based on two main factors; base-material properties of porous structure and pore characteristics. The next step is selecting the optimal level of machining parameters with respect to these porous material characteristics.

In this chapter, first, the effects of base-material properties and the pore characteristics on the cutting mechanism of porous structure are discussed. Afterwards, cutting parameters have been considered to find their impacts on final product quality. Finally, the optimal condition to achieve the high quality of machined surface has been discussed.

6.2 Porous material characteristics

6.2.1 Base-material properties

It is not easy to define the material machinability without the help of the original material's properties. The property of a material governs the ease or difficulty with which a material can be machined using a cutting tool. Machinability can be defined based on three factors including tool life, cutting energy and machined surface quality each of which is strongly dependent on workpiece material's properties. Materials with good machinability require little power to remove material, easily obtain a good finish and do not cause tool wear

[147–151]. The most influential properties of the material in machinability are hardness, yield strength, toughness and thermal conductivity.

Hardness is closely related to strength. It is the ability of a material to resist a localized deformation from indentation, scratching, penetration bending, abrasion, and wear. A harder material is thought to be less machinable. Low hardness values make a material easier to machining. However, low hardness is a disadvantage if it is associated with high ductility.

Yield strength is defined as the stress at which a material begins to deform plastically. The high yield strength of the material gives an indication to poor machinability due to the rise of the specific cutting energy and, hence, cutting forces and power consumption.

The capacity of a material to absorb energy without fracture is called toughness. Fracture is a separation of an object or a material into two, or more, pieces under the action of stress which is an indicator of the stress amount required to propagate preexisting defects as there is no perfect material in nature.

Temperature rises at the tool–work interface, varied with the thermal conductivity of the work material and is directly affecting the cutting tool performance. Temperature distribution at the tool–work interface is determined by changes in microhardness or microstructure in the heat-affected regions of work material.

Table 6-1 shows the properties of three base-materials of porous structures used in this research work. The wide gap between mechanical properties such as fracture toughness and hardness causes base-materials to be categorized into two main sections: brittle porous materials including porous carbon and porous silicon and ductile porous materials including porous titanium.

Table 6-1: Material properties of porous materials workpieces

	Hardness (MPa)	Yield strength (tensile) (MPa)	Fracture toughness (MPa√m)	Thermal conductivity (W/m.°C)
Silicon	13000	5900	1.28	159
Carbon	300	150	2.4	114
Titanium	1422	300	80	14

As mentioned earlier, decreasing cutting scale to the nanometer level leads brittle materials like silicon to be cut in ductile mode because of hydrostatic pressure existing in the vicinity of cutting edge. In the case of single crystal silicon, it is generally accepted that a structural change from diamond cubic (Si-I) to a metallic state β-Sn (Si-II) occurs under this high hydrostatic pressure. The material around the tool cutting edge would then become ductile enough to sustain plastic flow. In contrast, in ductile materials like titanium ductile cutting mode occurs in a wide range of micro to nanometers level based on an intense shear generated between the tool tip engaged in the material and the workpiece. This strain in the chip is confined to narrow bands between the segments called shear zone with very little deformation within these segments. Figure 6-1a shows the mechanism of deformation in silicon where high-pressure area exists around cutting edge compared to Figure 6-1b in which deformation takes place in a shear zone in titanium cutting.

Brittle materials are very sensitive to tensile stress due to the fact that tensile stress produces microcracks. Tensile stress is the main reason why brittle materials are cut in a brittle mode. Consequently, the selection of failure criteria for brittle materials is also different from those of ductile materials. The original Mohr hypothesis, constructed with tensile, compression, and torsion tests, with a curved failure locus, is presented as the best hypothesis for brittle materials. However, the difficulty of applying it without a computer leads engineers to choose

modifications namely, Coulomb Mohr or modified Mohr [152]. All these fracture hypotheses show that brittle materials are more sensitive to tensile stress.

Unlike brittle materials, there is not a significant difference between yield compressive and tensile stress in ductile materials. As a result, they are not sensitive to tensile stress as brittle materials. For ductile behavior, the preferred criterion is the distortion-energy theory, although some designers also apply the maximum-shear-stress theory because of its simplicity and conservative nature.

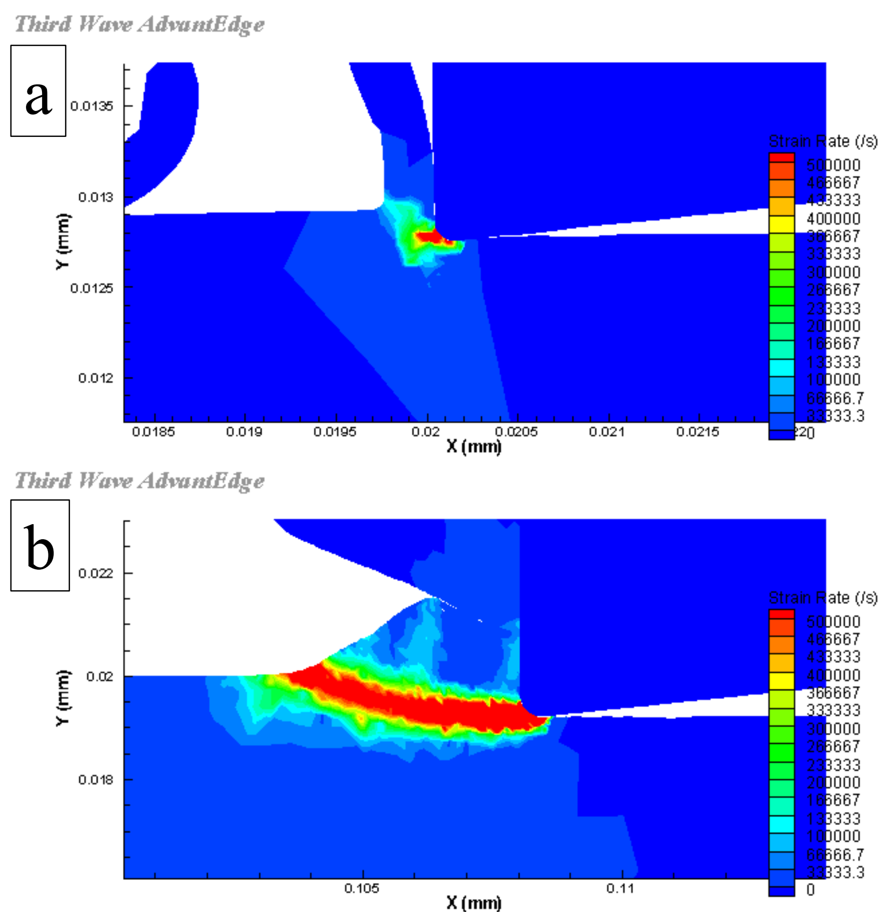

Figure 6-1: Mechanisms of cutting in (a) brittle and (b) ductile materials (a=2r)

The difference between brittle and ductile materials can be more significant when it comes to porous structure workpieces. In case of a brittle porous material, hydrostatic pressure state which is an essential for cutting brittle materials in ductile mode cannot be maintained around a pore resulting in brittle fracture around pore edges (Figure 6-2a). As the tool reaches

the pore edge a very large tensile stress area is formed beneath the tool tip and extending towards the pore (Figure 4-16a). This kind of tensile stress induces a microcrack propagation and results in brittle fractures. In contrast, high level of plastic deformation in materials with high toughness (ductile materials) shows different behavior on pore edge as shown in Figure 6-2b.

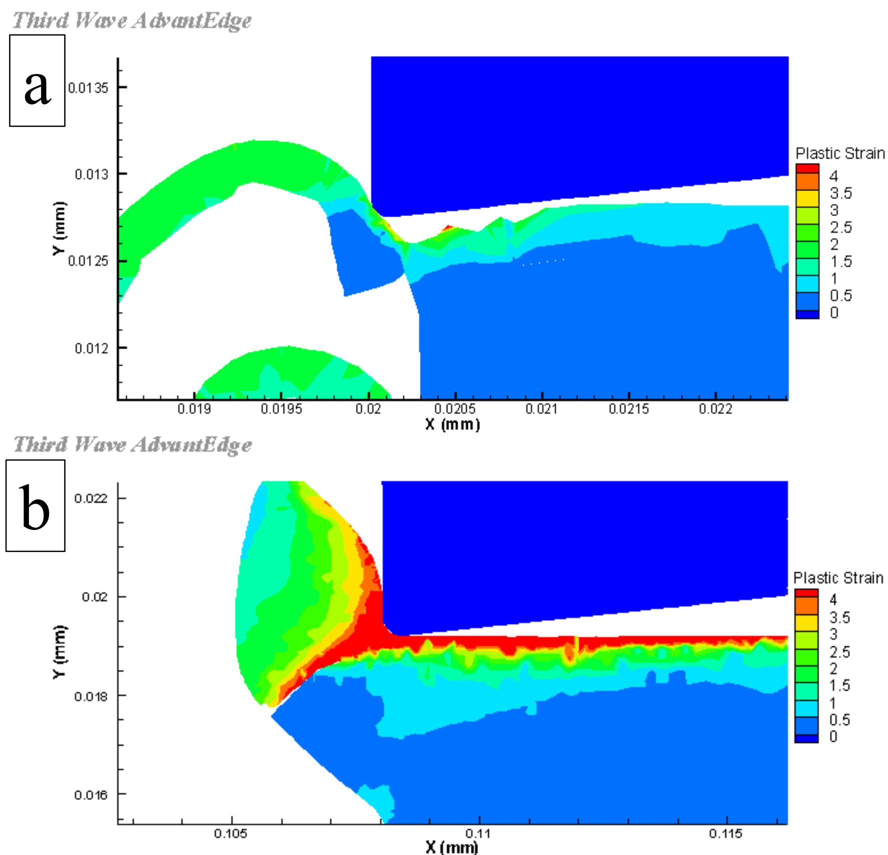

Figure 6-2: Mechanisms of cutting on pore edge in (a) brittle and (b) ductile materials (a=2r)

The comparison between the principal force of brittle materials and ductile materials also shows a difference due to their mechanical properties. As shown in Figure 6-3 the principal force required to cut pure titanium is more than 3 times than that of silicon at the almost same undeformed chip thickness: notwithstanding, silicon has higher hardness compared to pure titanium. These results indicate that the fracture toughness significantly influences cutting energy in the machining process. It should be mentioned that in this experiment silicon was cut in partially brittle mode.

However, the notable difference is a wide gap between forces in porous structures compared to those of dense structures in both ductile and brittle materials. The porosity percentage of both porous titanium and porous silicon is about 30% which reduces the effective volume of deformed material, thus what was expected that there might be a 30% decrease in forces in both cases. Nevertheless, this reduction is only 23% in porous titanium, while there is a sharp decrease of 72% in porous silicon compared to pure titanium and silicon respectively. The lower reduction in principal force in porous titanium can be justified based on welding phenomenon which occurs in ductile materials. Whereas, it is presumable that the significant reduction of principal force in porous silicon cutting was caused by high level of brittle fractures occurring all over machined surface due to the presence of the pores because the brittle material removal results in lower cutting forces.

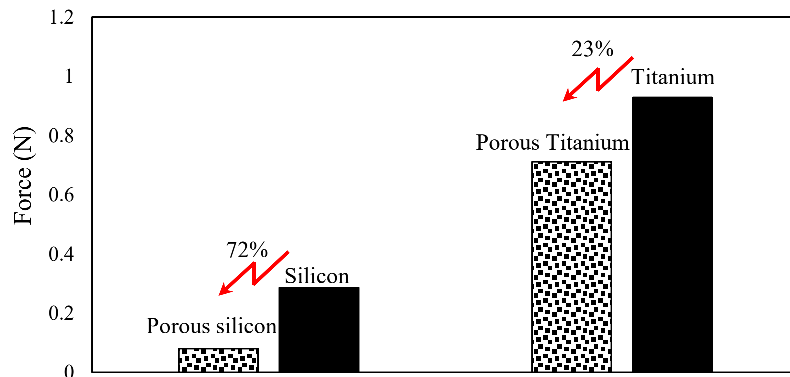

Figure 6-3: Principal force comparison in ductile and brittle workpiece cutting

6.2.2 Pore characteristics

Another factor that should be taken into account in the investigation of porous structure cutting is pore characteristics. Pore characteristics can be divided into three main parameters: pore size, pore shape, and pore location (distribution).

Generally, decreasing pore size increases the chance of the pore being closed during machining. This is more significant when machining of ductile materials because of high plastic deformation existing during the machining of this materials. The smaller pores will be closed owing to the plastic flow as shown in Figure 6-4a. On the other hand, in brittle porous materials, the length of the free edge (pore edge) on the workpiece surface is more important because increasing free edge increases the brittle fracture area on the machined surface that increases surface roughness in brittle porous structure.

Moreover, the ratio of average pore size to undeformed chip thickness also plays important role in chip formation and machined surface topography. As undeformed chip thickness decreases to the nanometer scale (h_{max}=99 nm), the ratio of pores bigger than undeformed chip thickness increases. As a result, the effect of pores on chip formation has become more significant and chip tearing in porous ductile material cutting are more obvious compared to those of dense material cutting (Figure 5-21). Increasing the chip tearing in the cutting process has a notable impact on machined surface topography at extremely small h_{max}.

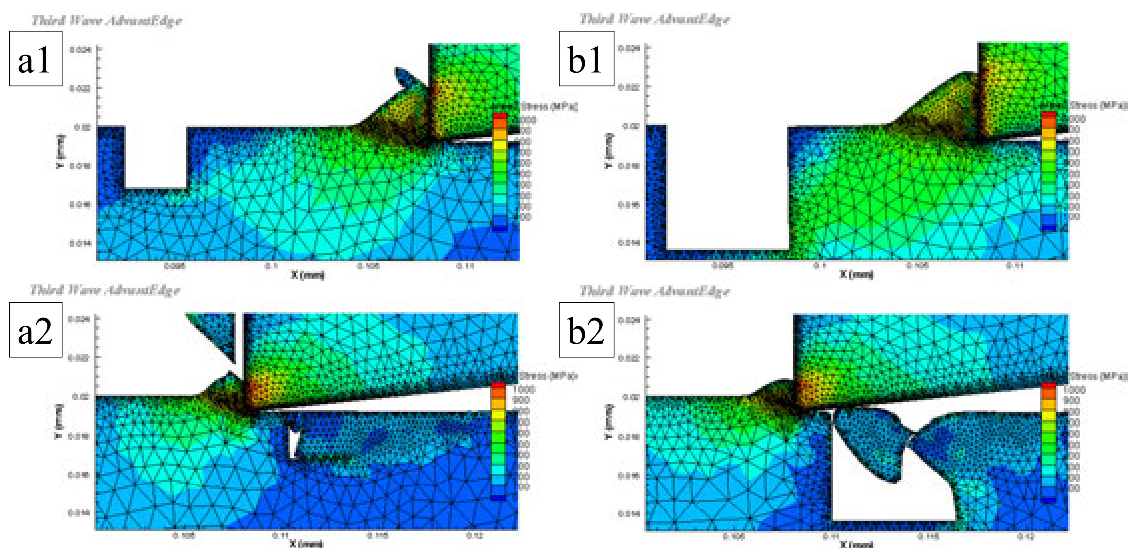

Figure 6-4: Pore size effects on cutting deformation ((a1) and (a2)) small pore and ((b1) and (b2)) big pore

Although most porous materials are produced through powder metallurgy or methods where pore shape is random and undefined, some porous materials like porous silicon

fabricated by anodic oxidation of single-crystal silicon wafers have pores with same defined pattern and shape. The mechanism of material removal is strongly dependent on the direction of cutting with respect to the pore edge orientation in brittle porous materials such as porous silicon. The shapes and position of edges to the cutting direction have a significant impact on brittle fracture on those edges. In general, it can be said that there are three types of material removal behaviors in various areas around a pore: severely fractured area, slightly fractured area, and ductile-cut area.

Figure 6-5 shows the schematic illustration of four areas of pore edges at triangular, circle and rectangular-shape pores. In cutting direction condition, indicated by "A" in all three shapes, the areas indicated by "I" are cut in severe brittle mode, the areas indicated by "II" and "III" are cut in partially brittle mode and the areas indicated by "IV" are cut in ductile mode at fine undeformed chip thickness, but the magnitude of different modes are depended on shape.

Although in some shape like circle pore the cutting direction is not important, in triangular and rectangular shape pore cutting direction is a significant factor e.g. changing cutting direction from "A" to "B" can change the magnitude of cutting mode in four areas.

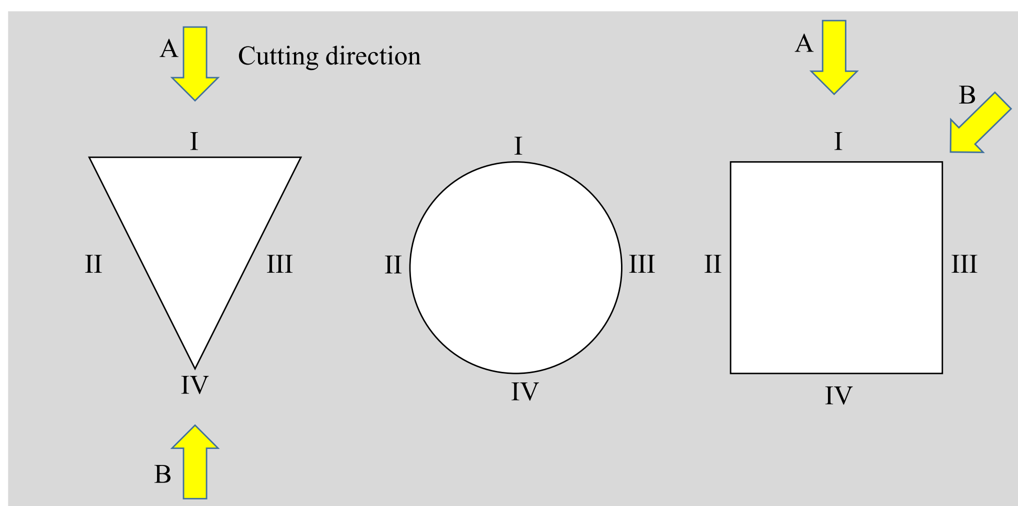

Figure 6-5: Pore shape effects on cutting deformation

The third important pore characteristic is pore location. The chip morphology and surface topography are influenced by pore location. The location of pores toward undeformed chip area may lead to an opening on the chip surface or machined surface or both. For example, the pore near the uncut workpiece surface remains as an opening on the chip surface; while for the deeper pore located between undeformed chip and machined surface, the bottom part remains on machined surface leading to an open cavity on the surface, and the top part causes an opening on the back side of the chip. Nevertheless, due to the nature of porous materials fabricated through powder metallurgy, it is difficult to control this parameter.

6.3 Cutting parameters and conditions

In a machining operation of porous materials, it is an important task to select cutting parameters with respect to workpiece properties for securing a high quality of the product. Usually, there are lots of handbooks that can be used to determine the desired cutting parameters for bulk materials, however, there is no reference and handbook for machining of porous materials. To select the cutting parameters properly, the porous materials characteristics should be considered simultaneously. Three cutting parameters including feed rate, depth of cut, cutting speed and tool nose radius play a remarkable role in cutting mechanism in face turning process. In addition, machining in dry or wet condition and the use of infiltrant can change the quality of machined surface depended on porous material properties.

Unlike conventional machining in which depth of cut, feed rate, and tool nose radius can be considered individually, in ultraprecision machining, the combination of these three parameters leads to a unique undeformed chip profile in which maximum undeformed chip thickness (h_{max}) is an important parameter to evaluate the cutting performance (Eq. (2)). With decreasing the both of feed rate and depth of cut, h_{max} decreases having different impacts on the mechanism of cutting respecting base-material properties of workpiece e.g. in brittle porous

materials fine undeformed chip thickness causes the workpiece to be cut in a ductile mode which improves the flatness of product. In contrast, in ductile porous material as undeformed chip thickness decreases, most pores will be closed on the machined surface due to high plastic flow and chip tearing phenomenon. The effects of cutting speed on machining process can be discussed based on its influence on temperature produced during the cutting process. Although increasing temperature can have desired impact on the ductile cutting mode in a brittle material, it may increase plastic flow in a ductile material cutting which is undesirable in this cutting scale. In such a case, utilizing coolant during the process can decrease temperature effects on the cutting mechanism.

Moreover, although, decreasing undeformed chip thickness improves the machined surface of porous brittle materials, chips entering into pores during process remains a big problem to produce a machined surface with high porosity percentage. In such a case, using wax as infiltrant not only prevents chips from entering pores but also shows significant improvement in surface quality in terms of decreasing brittle fractures.

6.4 Conclusions

Regarding the aforementioned parameters, porous materials can be categorized based on base-material property or pore characteristics into different subsections. Figure 6-6 shows the flowchart of subsections. Therefore, in the investigation of material removal mechanism and surface integrity in the porous material workpiece, all these parameters might be considered. Accordingly, the challenges ahead and the strategy toward improving machining process in these materials are also different.

In brittle porous materials cutting, the main challenge is brittle fracture around pores as well as filling pores during machining by chips. There are two methods to decrease brittle

fracture around pore in brittle structures: First, decreasing undeformed chip thickness to less than the critical value, and second using infiltrant such as wax that prevents chips from getting into pores, and helps to resist hydrostatic pressure around the pore to some extent, preventing the propagation of cracks. In the porous silicon case, controlling h_{max} under 25 nm and using wax as infiltrant, the high level of flatness (10 nm) with high level opened pores (~100% opened pores) can be achieved.

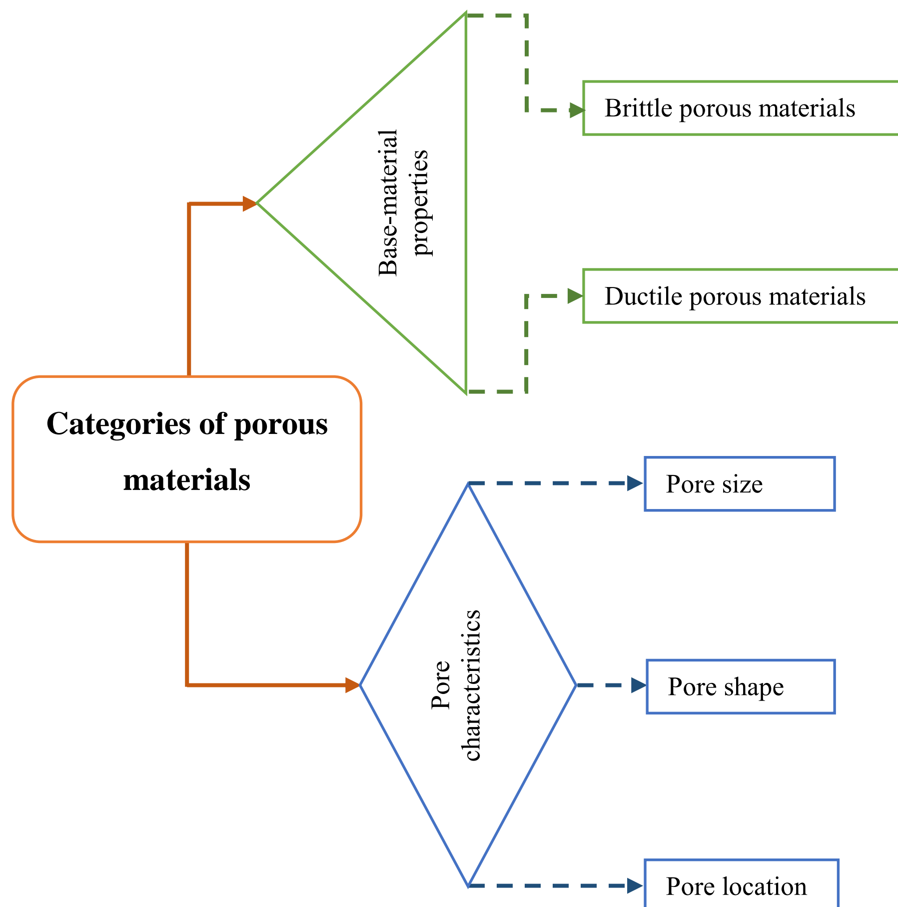

Figure 6-6: Flowchart of porous material categories

In ductile porous material cutting, the main challenge is the high level of plastic deformation leading the pores to be closed during machining. The cutting of ductile porous materials in nanometer scale not only increases the plastic deformation resulting in a sharp decrease in porosity percentage but also degrades surface roughness because of chip tearing phenomenon. Therefore, the machining parameters specially undeformed chip thickness

should be controlled within micrometer scale (depending on material properties) to achieve desired surface roughness and porosity percentage. In the porous titanium case, depending on desirable quality; the level of opened pores or surface flatness, h_{max} can be ranged from a thousand micrometers to just a micrometer. As there is an inverse relationship between flatness and machined surface porosity percentage, applying coolant and decreasing cutting speed can be helpful to decrease plastic flow during the cutting process. The results of porous titanium cutting show that the high level of opened pores can be achieved at about h_{max}= 12 µm in dry cutting condition.

In pore characteristic factors, although it is difficult to control pore location, the choice of an appropriate pore shape and simultaneously cutting direction have a significant influence on brittle fracture level on machined surface and as result surface roughness, e.g. using direction indicated by "B" in triangular shape can decrease overall fracture area around pore. However, further research work is required to be carried out in pore characteristic parameters to find optimum condition. Figure 6-7 shows a guideline flowchart to select proper machining conditions in diamond turning of porous materials with different properties.

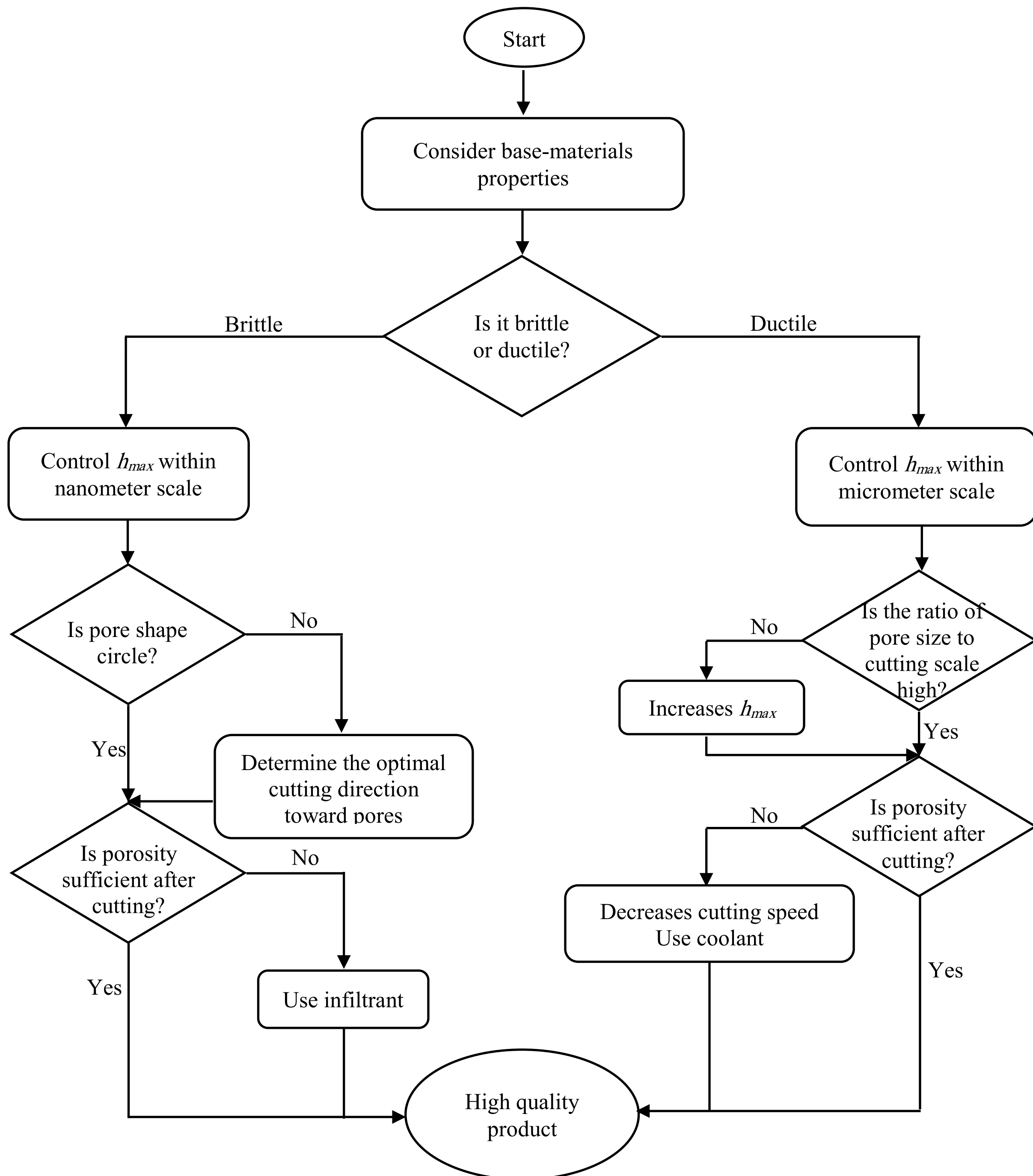

Figure 6-7: The guideline to produce high quality surface in porous material cutting

CHAPTER 7

Conclusion

Chapter 7 : Conclusions and future work

7.1 Conclusions

This research work attempts to present a comprehensive investigation on ultraprecision machining of a new class of engineering materials called porous materials. Three types of porous materials were selected based on different characteristics they exhibit during the cutting process. The mechanism of cutting and surface integrity in the ultraprecision diamond turning of porous materials compared to dense materials were studied by both experiments and FE simulation under various conditions. Based on the results presented in this thesis, the main conclusions and achievements are detailed below.

The mechanism of porous materials cutting is significantly different from those of dense materials due to the existence of pores. These differences can be seen in cutting force characteristics, chip morphology and machined surface topography.

The greatest challenge of ductile porous material cutting is the high level of plastic deformation leading the pores to be closed during machining, while, brittle fracture around pores, filled pores by chips, and grain rotation are main problems in brittle and hard porous material cutting. Thus, the strategy to address the challenges should be different.

The role undeformed chip thickness plays on material removal mechanism of both brittle and ductile porous materials was presented. The results showed that by controlling this parameter and in some cases using infiltrant, the desired machined surface with open pores were achievable.

Unlike brittle porous materials, decreasing cutting scale to nanometer level when cutting ductile porous materials can degrade surface quality due to chip tearing phenomenon which is the main reason for debris generation and chip adhesion. In addition, the cutting

process at low undeformed chip thickness has great influences on the subsurface microstructure of workpiece. This subsurface layer characteristics can be changed by applying coolant during the cutting process.

Tool wear characteristics in the cutting of porous materials are dependent on mechanical properties of base-material of the porous structure and significantly different from those of dense materials.

7.2 Future work

Research towards machining of porous materials has just begun, and it will most likely take some time before a comprehensive understanding about machining of this class of materials emerges. Several recommendations are proposed for the future work of machining of porous materials. The recommendations are as follows:

An important step can be to evaluate the applicability of findings from the present study to machining of other porous materials e.g. investigating undeformed chip thickness effects for a variety of porosities and pore sizes of porous materials with different base-material properties in which either high surface porosity or low surface roughness is a major concern. The next step would be developing new methods and techniques to maintain surface porosity of machined surface during machining process and enhancing surface quality e.g. using different infiltrant with various hardness. While in this work the subsurface microstructure changes induced by machining process in both brittle and ductile porous materials have been studied and documented, relatively little work has been done to assess all changes taken place in mechanical properties of machined surfaces. Commonly used characterization techniques such as XRD residual stress measurement and phase transformation provide some insight into the difference between the machined surfaces and subsurface compared to those of dense materials.

References

[1] H.K. Chae, D.Y. Siberio-Pérez, J. Kim, Y. Go, M. Eddaoudi, A.J. Matzger, M. O'Keeffe, O.M. Yaghi, A route to high surface area, porosity and inclusion of large molecules in crystals, Nature. 427 (2004) 523–527. doi:10.1038/nature02311.

[2] O.R. Tutunea-Fatan, M.A. Fakhri, E. V Bordatchev, Porosity and cutting forces: from macroscale to microscale machining correlations, Proc. Inst. Mech. Eng. Part B J. Eng. Manuf. 225 (2011) 619–630. doi:10.1177/2041297510394057.

[3] L.-P.L.P. Lefebvre, J. Banhart, D.C. Dunand, Porous metals and metallic foams: Current status and recent developments, Adv. Eng. Mater. 10 (2008) 775–787. doi:10.1002/adem.200800241.

[4] P.S. Liu, G.F. Chen, Porous Materials Processing and Applications, Butterworth-Heinemann, Oxford, 2014.

[5] M. Thakur, M. Isaacson, S.L. Sinsabaugh, M.S. Wong, S.L. Biswal, Gold-coated porous silicon films as anodes for lithium ion batteries, J. Power Sources. 205 (2012) 426–432. doi:10.1016/j.jpowsour.2012.01.058.

[6] S.R. Gowda, V. Pushparaj, S. Herle, G. Girishkumar, J.G. Gordon, H. Gullapalli, X. Zhan, P.M. Ajayan, A.L.M. Reddy, Three-dimensionally engineered porous silicon electrodes for Li ion batteries., Nano Lett. 12 (2012) 6060–5. doi:10.1021/nl302114j.

[7] V. Pacebutas, K. Grigoras, A. Krotkus, Porous silicon applications in solar cell technology, Phys. Scr. T69 (1997) 255–258. doi:10.1088/0031-8949/1997/T69/053.

[8] L.T. Canham, Silicon quantum wire array fabrication by electrochemical and chemical dissolution of wafers, Appl. Phys. Lett. 57 (1990) 1046. doi:10.1063/1.103561.

[9] R.S. Dubey, Electrochemical Fabrication of Porous Silicon Structures for Solar Cells, Nanosci. Nanoeng. 1 (2013) 36–40. doi:10.13189/nn.2013.010105.

[10] M. Abolghasemi Fakhri, E. V. Bordatchev, O.R. Tutunea-Fatan, An image-based methodology to establish correlations between porosity and cutting force in micromilling of porous titanium foams, Int. J. Adv. Manuf. Technol. 60 (2012) 841–851. doi:10.1007/s00170-011-3647-1.

[11] S. Roy, D. Panda, N. Khutia, A.R. Chowdhury, Pore Geometry Optimization of Titanium (Ti6Al4V) Alloy, for Its Application in the Fabrication of Customized Hip Implants, Int. J. Biomater. 2014 (2014) 1–12. doi:10.1155/2014/313975.

[12] M. Gauthier, L.P. Lefebvre, Y. Thomas, M.N. Bureau, Production of metallic foams having open porosity using a powder metallurgy approach, Mater. Manuf. Process. 19 (2004) 793–811. doi:10.1081/Lmmp-20030539.

[13] E. Brinksmeier, W. Preuss, Micro-machining, Philos. Trans. R. Soc. A Math. Phys. Eng. Sci. 370 (2012) 3973–3992. doi:10.1098/rsta.2011.0056.

[14] S.J. Zhang, S. To, S.J. Wang, Z.W. Zhu, A review of surface roughness generation in ultra-precision machining, Int. J. Mach. Tools Manuf. 91 (2015) 76–95. doi:10.1016/j.ijmachtools.2015.02.001.

[15] N. Taniguchi, On the basic concept of “nano-technology,” Part II, Japan Soc. of Precision Eng. (1974).

[16] N. Taniguchi, Current Status in, and Future Trends of, Ultraprecision Machining and Ultrafine Materials Processing, CIRP Ann. - Manuf. Technol. 32 (1983) 573–582. doi:10.1016/S0007-8506(07)60185-1.

[17] P. Shore, P. Morantz, Ultra-precision: enabling our future, Philos. Trans. R. Soc. A Math. Phys. Eng. Sci. 370 (2012) 3993–4014. doi:10.1098/rsta.2011.0638.

[18] X. Liu, R.E. DeVor, S.G. Kapoor, K.F. Ehmann, The Mechanics of Machining at the Microscale: Assessment of the Current State of the Science, J. Manuf. Sci. Eng. 126 (2004) 666. doi:10.1115/1.1813469.

[19] S. Goel, X. Luo, A. Agrawal, R.L. Reuben, Diamond machining of silicon : A review of advances in molecular dynamics simulation, Int. J. Mach. Tools Manuf. 88 (2015) 131–164. doi:10.1016/j.ijmachtools.2014.09.013.

[20] S. Goel, X. Luo, P. Comley, R.L. Reuben, A. Cox, Brittle-ductile transition during diamond turning of single crystal silicon carbide, Int. J. Mach. Tools Manuf. 65 (2013) 15–21. doi:10.1016/j.ijmachtools.2012.09.001.

[21] I.D. Marinescu, H.K. Tonshoff, I. Inasaki, eds., Handbook of Ceramic Grinding and Polishing, NOYES, Elsevier, Norwich, NY, 2000. http://linkinghub.elsevier.com/retrieve/pii/S0301679X00001109.

[22] M. Yoshino, T. Aoki, T. Sugishima, T. Shirakashi, Scratching test on hard-brittle materials under high hydrostatic pressure, Seimitsu Kogaku Kaishi/Journal Japan Soc. Precis. Eng. 65 (1999) 1481–1485. doi:10.1115/1.1347035.

[23] P.W. Bridgman, I. Šimon, Effects of Very High Pressures on Glass, J. Appl. Phys. 24 (1953) 405–413. doi:10.1063/1.1721294.

[24] P.N. Blake, R.O. Scattergood, Ductile-Regime Machining of Germanium and Silicon, J. Am. Ceram. Soc. 73 (1990) 949–957. doi:10.1111/j.1151-2916.1990.tb05142.x.

[25] T. Nakasuji, S. Kodera, S. Hara, H. Matsunaga, N. Ikawa, S. Shimada, Diamond Turning of Brittle Materials for Optical Components, CIRP Ann. - Manuf. Technol. 39 (1990) 89–92. doi:10.1016/S0007-8506(07)61009-9.

[26] K.E. Puttick, M.R. Rudman, K.J. Smith, A. Franks, K. Lindsey, Single-Point Diamond Machining of Glasses, Proc. R. Soc. A Math. Phys. Eng. Sci. 426 (1989) 19–30. doi:10.1098/rspa.1989.0116.

[27] T.. Leung, W.. Lee, X.. Lu, Diamond turning of silicon substrates in ductile-regime, J. Mater. Process. Technol. 73 (1998) 42–48. doi:10.1016/S0924-0136(97)00210-0.

[28] J. Yan, M. Yoshino, T. Kuriagawa, T. Shirakashi, K. Syoji, R. Komanduri, On the ductile machining of silicon for micro electro-mechanical systems (MEMS), opto-electronic and optical applications, Mater. Sci. Eng. A. 297 (2001) 230–234. doi:10.1016/S0921-5093(00)01031-5.

[29] J. Patten, H. Cherukuri, J. Yan, Ductile-regime machining of semiconductors and ceramics, in: Y. Gogotsi, V. Domnich (Eds.), High Press. Surf. Sci. Eng., Taylor & Francis, 2003: pp. 543–632. doi:10.1201/9781420034134.sec6.

[30] J. Yan, K. Syoji, T. Kuriyagawa, H. Suzuki, Ductile regime turning at large tool feed, J. Mater. Process. Technol. 121 (2002) 363–372. doi:10.1016/S0924-0136(01)01218-3.

[31] M. Yoshino, T. Aoki, T. Shirakashi, R. Komanduri, Some experiments on the scratching of silicon:In situ scratching inside an SEM and scratching under high external hydrostatic pressures, Int. J. Mech. Sci. 43 (2001) 335–347. doi:10.1016/S0020-7403(00)00019-9.

[32] I. V. Gridneva, Y. V. Milman, V.I. Trefilov, Phase transition in diamond-structure crystals during hardness measurements, Phys. Status Solidi. 14 (1972) 177–182.

doi:10.1002/pssa.2210140121.

[33] D.R. Clarke, M.C. Kroll, P.D. Kirchner, R.F. Cook, B.J. Hockey, Amorphization and Conductivity of Silicon and Germanium Induced by Indentation, Phys. Rev. Lett. 60 (1988) 2156–2159. doi:10.1103/PhysRevLett.60.2156.

[34] J. Yan, T. Asami, H. Harada, T. Kuriyagawa, Fundamental investigation of subsurface damage in single crystalline silicon caused by diamond machining, Precis. Eng. 33 (2009) 378–386. doi:10.1016/j.precisioneng.2008.10.008.

[35] R. Boyer, G. Welsch, E.W. Collings, Materials properties handbook: titanium alloys, ASM international, 1993.

[36] J.P. Davim, ed., Machining of Titanium Alloys, Springer Berlin Heidelberg, Berlin, Heidelberg, 2014. doi:10.1007/978-3-662-43902-9.

[37] E.O. Ezugwu, Z.M. Wang, Titanium alloys and their machinability—a review, J. Mater. Process. Technol. 68 (1997) 262–274. doi:10.1016/S0924-0136(96)00030-1.

[38] A.R. Machado, J. Wallbank, Machining of titanium and its alloys-a review, Proc. Inst. Mech. Eng. Part B J. Eng. Manuf. 204 (1990) 53–60. doi:10.1243/PIME_PROC_1990_204_047_02.

[39] J. Matthew, J. Donachie, Titanium a technical guide, 2nd ed., InTech, 2012. doi:10.5772/1844.

[40] X. Yang, C. Richard Liu, Machining titanium and its alloys, Mach. Sci. Technol. 3 (1999) 107–139. doi:10.1080/10940349908945686.

[41] S. Sun, M. Brandt, M.S. Dargusch, Characteristics of cutting forces and chip formation in machining of titanium alloys, Int. J. Mach. Tools Manuf. 49 (2009) 561–568. doi:10.1016/j.ijmachtools.2009.02.008.

[42] M. Calamaz, D. Coupard, F. Girot, A new material model for 2D numerical simulation of serrated chip formation when machining titanium alloy Ti–6Al–4V, Int. J. Mach. Tools Manuf. 48 (2008) 275–288. doi:10.1016/j.ijmachtools.2007.10.014.

[43] A. Molinari, X. Soldani, M.H. Miguelez, Adiabatic shear banding and scaling laws in chip formation with application to cutting of Ti-6Al-4V, J. Mech. Phys. Solids. 61 (2013) 2331–2359. doi:10.1016/j.jmps.2013.05.006.

[44] R. Komanduri, B.F. Von Turkovich, New observations on the mechanism of chip formation when machining titanium alloys, Wear. 69 (1981) 179–188. doi:10.1016/0043-1648(81)90242-8.

[45] R. Komanduri, Some clarifications on the mechanics of chip formation when machining titanium alloys, Wear. 76 (1982) 15–34. doi:10.1016/0043-1648(82)90113-2.

[46] E.O. Ezugwu, J. Bonney, Y. Yamane, An overview of the machinability of aeroengine alloys, J. Mater. Process. Technol. 134 (2003) 233–253. doi:10.1016/S0924-0136(02)01042-7.

[47] A. Hasçalik, U. Çaydaş, Optimization of turning parameters for surface roughness and tool life based on the Taguchi method, Int. J. Adv. Manuf. Technol. 38 (2008) 896–903. doi:10.1007/s00170-007-1147-0.

[48] S. Ramesh, L. Karunamoorthy, K. Palanikumar, Fuzzy modeling and analysis of machining parameters in machining titanium alloy, Mater. Manuf. Process. 23 (2008) 439–447. doi:10.1080/10426910801976676.

[49] S.R. Chauhan, K. Dass, Optimization of machining parameters in turning of Titanium (grade-5) alloy using response surface methodology, Mater. Manuf. Process. 27 (2012) 531–537. doi:10.1080/10426914.2011.593236.

[50] M. V. Ribeiro, M.R. V. Moreira, J.R. Ferreira, Optimization of titanium alloy (6Al-4V) machining, J. Mater. Process. Technol. 143–144 (2003) 458–463. doi:10.1016/S0924-0136(03)00457-6.

[51] C.H. Che-Haron, Tool life and surface integrity in turning titanium alloy, J. Mater. Process. Technol. 118 (2001) 231–237. doi:10.1016/S0924-0136(01)00926-8.

[52] D. Ulutan, T. Ozel, Machining induced surface integrity in titanium and nickel alloys: A review, Int. J. Mach. Tools Manuf. 51 (2011) 250–280. doi:10.1016/j.ijmachtools.2010.11.003.

[53] C.H. Che-Haron, A. Jawaid, The effect of machining on surface integrity of titanium alloy Ti-6% Al-4% V, J. Mater. Process. Technol. 166 (2005) 188–192. doi:10.1016/j.jmatprotec.2004.08.012.

[54] A. Ginting, M. Nouari, Surface integrity of dry machined titanium alloys, Int. J. Mach. Tools Manuf. 49 (2009) 325–332. doi:10.1016/j.ijmachtools.2008.10.011.

[55] A.R. Zareena, S.C. Veldhuis, Tool wear mechanisms and tool life enhancement in ultraprecision machining of titanium, J. Mater. Process. Technol. 212 (2012) 560–570. doi:10.1016/j.jmatprotec.2011.10.014.

[56] F. Schneider, R. Lohkamp, F.J.P. Sousa, R. Müller, J.C. Aurich, Analysis of the Surface Integrity in Ultraprecision Cutting of Cp-titanium by Investigating the Chip Formation, Procedia CIRP. 13 (2014) 55–60. doi:10.1016/j.procir.2014.04.010.

[57] F. Schneider, R. Bischof, B. Kirsch, C. Kuhn, R. Müller, J.C. Aurich, Investigation of Chip Formation and Surface Integrity when Micro-cutting cp-Titanium with Ultra-fine Grain Cemented Carbide, Procedia CIRP. 45 (2016) 115–118. doi:10.1016/j.procir.2016.02.257.

[58] X. Ruibin, H. Wu, Study on cutting mechanism of Ti6Al4V in ultraprecision machining, Int. J. Adv. Manuf. Technol. 86 (2016) 1311–1317. doi:10.1007/s00170-015-8304-7.

[59] J.P. Colafemina, R.G. Jasinevicius, J.G. Duduch, Surface integrity of ultraprecision diamond turned Ti (commercially pure) and Ti alloy (Ti-6Al-4V), Proc. Inst. Mech. Eng. Part B J. Eng. Manuf. 221 (2007) 999–1006. doi:10.1243/09544054JEM798.

[60] M. Nouari, H. Makich, On the Physics of Machining Titanium Alloys: Interactions between Cutting Parameters, Microstructure and Tool Wear, Metals (Basel). 4 (2014) 335–358. doi:10.3390/met4030335.

[61] A.. Shahan, A. karimi Taheri, Adiabatic shear bands in titanium and titanium alloys: a critical review, Mater. Des. 14 (1993) 243–250. doi:10.1016/0261-3069(93)90078-A.

[62] V. Piispanen, Theory of Formation of Metal Chips, J. Appl. Phys. 19 (1948) 876–881. doi:10.1063/1.1697893.

[63] V.P. Astakhov, Geometry of Single-point Turning Tools and Drills, Springer London, London, 2010. doi:10.1007/978-1-84996-053-3.

[64] S. Kalpakjian, S.R. Schmid, Manufacturing engineering and technology, Sixth, Pearson, New York, 2009.

[65] K. Nakayama, K. Tamura, Size Effect in Metal-Cutting Force, J. Eng. Ind. (1968) 119–126. doi:10.1115/1.3604585.

[66] F. Klocke, Manufacturing Processes 1: cutting, Springer, Berlin, 2011. doi:10.1007/978-

3-642-11979-8.

[67] J. Klett, R. Hardy, E. Romine, C. Walls, T. Burchell, High-thermal-conductivity, mesophase-pitch-derived carbon foams: effect of precursor on structure and properties, Carbon N. Y. 38 (2000) 953–973. doi:10.1016/S0008-6223(99)00190-6.

[68] N.C. Gallego, J.W. Klett, Carbon foams for thermal management, Carbon N. Y. 41 (2003) 1461–1466. doi:10.1016/S0008-6223(03)00091-5.

[69] M. Wei, J. Wang, A novel acetylcholinesterase biosensor based on ionic liquids-AuNPs-porous carbon composite matrix for detection of organophosphate pesticides, Sensors Actuators B Chem. 211 (2015) 290–296. doi:10.1016/j.snb.2015.01.112.

[70] C. Fan, V. Nguyen, Y. Zeng, P. Phadungbut, T. Horikawa, D.D. Do, D. Nicholson, Novel approach to the characterization of the pore structure and surface chemistry of porous carbon with Ar, N2, H2O and CH3OH adsorption, Microporous Mesoporous Mater. 209 (2015) 79–89. doi:10.1016/j.micromeso.2015.01.013.

[71] K.D. Hirschman, L. Tsybeskov, S.P. Duttagupta, P.M. Fauchet, Silicon-based visible light-emitting devices integrated into microelectronic circuits, Nature. 384 (1996) 338–341. doi:10.1038/384338a0.

[72] C.C. Striemer, P.M. Fauchet, Dynamic etching of silicon for broadband antireflection applications, Appl. Phys. Lett. 81 (2002) 2980–2982. doi:10.1063/1.1514832.

[73] V.S.-Y. Lin, K. Motesharei, K.-P.S. Dancil, M.J. Sailor, M.R. Ghadiri, A Porous Silicon-Based Optical Interferometric Biosensor, Science (80-.). 278 (1997) 840 LP-843. doi:10.1126/science.278.5339.840.

[74] E.X. Pérez, Design, fabrication and characterization of porous silicon multilayer optical devices, Universitat Rovira i Virgili, 2007. http://www.tdx.cat/handle/10803/8458.

[75] S. Chan, P.M. Fauchet, Y. Li, L.J. Rothberg, B.L. Miller, Porous silicon microcavities for biosensing applications, Phys. Status Solidi Appl. Res. 182 (2000) 541–546. doi:10.1002/1521-396X(200011)182:1<541::AID-PSSA541>3.0.CO;2-#.

[76] H. Föll, M. Christophersen, J. Carstensen, G. Hasse, Formation and application of porous silicon, Mater. Sci. Eng. R Reports. 39 (2002) 93–141. doi:http://ac.els-cdn.com/S0927796X02000906/1-s2.0-S0927796X02000906-main.pdf?_tid=cfe36b7e-9747-11e6-8558-

00000aacb35f&acdnat=1477024716_ab49a3eb263f596a72a13506794ec643.

[77] M. Bram, C. Kempmann, A. Laptev, D. Stöver, K. Weinert, Investigations on the machining of sintered titanium foams utilizing face milling and peripheral grinding, Adv. Eng. Mater. 5 (2003) 441–447. doi:10.1002/adem.200300356.

[78] A. Braem, L. Van Mellaert, D. Hofmans, E. De Waelheyns, J. Anné, J. Schrooten, J. Vleugels, Bacterial colonisation of porous titanium coatings for orthopaedic implant applications – effect of surface roughness and porosity, Powder Metall. 56 (2013) 267–271. doi:10.1179/0032589913Z.000000000124.

[79] V. Fröjd, L. Chávez de Paz, M. Andersson, A. Wennerberg, J.R. Davies, G. Svensäter, In situ analysis of multispecies biofilm formation on customized titanium surfaces, Mol. Oral Microbiol. 26 (2011) 241–252. doi:10.1111/j.2041-1014.2011.00610.x.

[80] V. Shapovalov, Porous Metals, Mrs Bulletin, 19 (1994) 24–28.

[81] E. Alizadeh, Factors influencing the machinability of sintered steels, Powder Metall. Met. Ceram. 47 (2008) 304–315. doi:10.1007/s11106-008-9021-7.

[82] H.C.S. ASM International, ASM Handbook, Volume 07, Powder Metal Technologies and Applications, ASM International, 1998. doi:10.1017/CBO9781107415324.004.

[83] M. Hamiuddin, Q. Murtaza, Machinability of phosphorous containing sintered steels, Mater. Chem. Phys. 67 (2001) 78–84. doi:10.1016/S0254-0584(00)00423-5.

[84] S. Andrej, S. Marcela, V. Karol, D. Herbert, Face turning of pm steels: effect of porosity and carbon level, Int. J. Powder Metall. 44 (2008) 49–61. http://cat.inist.fr/?aModele=afficheN&cpsidt=20375219 (accessed September 16, 2017).

[85] S. Chen, D. Head, I.S. Jawahir, An investigation of machining performance for controlled surface quality requirements in porous tungsten [for dispenser cathodes], in: Fifth IEEE Int. Vac. Electron. Conf. (IEEE Cat. No.04EX786), IEEE, 2005: pp. 358–359. doi:10.1109/IVELEC.2004.1316360.

[86] J.O. Tarter, M. Effgen, F. Pusavec, I.S. Jawahir, Cryogenic machining of porous tungsten for dispenser cathode applications, 2008 IEEE Int. Vac. Electron. Conf. IVEC with 9th IEEE Int. Vac. Electron Sources Conf. IVESC. (2008) 293–294. doi:10.1109/IVELEC.2008.4556349.

[87] F. Pusavec, a. Deshpande, J. Tarter, M. Effgen, J. O.W. Dillon, J. Kopac, I.S. Jawahir, Optimization of Machining Performance in Finish Turning of Porous Tungsten Under Cryogenic Conditions, 2nd Int. Conf. « Innov. Cut. Process. Smart Mach. ». (2008) 1–8.

[88] F. Pusavec, Porous tungsten machining under cryogenic conditions, Int. J. Refract. Met. Hard Mater. 35 (2012) 84–89. doi:10.1016/j.ijrmhm.2012.04.009.

[89] J. Schoop, M. Effgen, T.J. Balk, I.S. Jawahir, The Effects of Depth of Cut and Pre-cooling on Surface Porosity in Cryogenic Machining of Porous Tungsten, Procedia CIRP. 8 (2013) 357–362. doi:10.1016/j.procir.2013.06.116.

[90] J. Schoop, F. Ambrosy, F. Zanger, V. Schulze, T.J. Balk, I.S. Jawahir, Cryogenic machining of porous tungsten for enhanced surface integrity, J. Mater. Process. Technol. 229 (2016) 614–621. doi:10.1016/j.jmatprotec.2015.10.002.

[91] J.M. Schoop, Engineered Surface Properties of Porous Tungsten from Cryogenic Machining, University of Kentucky, 2015. http://uknowledge.uky.edu/cgi/viewcontent.cgi?article=1049&context=cme_etds.

[92] G. Em Totten, L. Xie, K. Funatani, Handbook of Mechanical Alloy Design, CRC Press, New York, 2003. doi:10.1201/9780203913307.

[93] H. Mohammadi, H.B. Poyraz, D. Ravindra, J.A. Patten, Surface finish improvement of an unpolished silicon wafer using micro-laser assisted machining, Int. J. Abras. Technol. 7 (2015) 107. doi:10.1504/IJAT.2015.073805.

[94] M.R. Reddy, Effect of Feed Rate on the Generation of Surface Roughness in Turning, Int. J. Eng. Sci. Technol. 3 (2011) 8099–8105.

[95] P. Dahlman, F. Gunnberg, M. Jacobson, The influence of rake angle, cutting feed and cutting depth on residual stresses in hard turning, J. Mater. Process. Technol. 147 (2004) 181–184. doi:10.1016/j.jmatprotec.2003.12.014.

[96] M.A. Davinci, N.L.L. Parthasarathi, U. Borah, S.K. Albert, M. Arvinth Davinci, N.L.L. Parthasarathi, U. Borah, S.K. Albert, Effect of the tracing speed and span on roughness parameters determined by stylus type equipment, Measurement. 48 (2014) 368–377. doi:10.1016/j.measurement.2013.11.023.

[97] E.S. Gadelmawla, M.M. Koura, T.M.A. Maksoud, I.M. Elewa, H.H. Soliman,

Roughness parameters, J. Mater. Process. Technol. 123 (2002) 133–145. doi:10.1016/S0924-0136(02)00060-2.

[98] D.C. Montgomery, G. Runger, Applied Statistics and Probability for Engineers, Third, John Wiley & Sons, 2003. doi:10.1198/tech.2007.s499.

[99] Michigan Metrology 3D Surface Roughness Measurement and Wear Measurement, Analysis and Inspection, (n.d.). http://www.michmet.com/ (accessed July 6, 2015).

[100] J.D.B. De Mello, Influence of surface topography on the surface durability of steam oxidised sintered iron, Mater. Res. 8 (2005) 135–141. doi:10.1590/S1516-14392005000200007.

[101] T.H. Panzera, J. Carlos, C. Rubio, A survey on ceramic composites for application in porous bearing, in: 18th Int. Congr. Mech. Eng., Ouro Preto, MG, 2005. http://www.abcm.org.br/anais/cobem/2005/PDF/COBEM2005-0942.pdf.

[102] J. Yan, Z. Zhang, T. Kuriyagawa, Mechanism for material removal in diamond turning of reaction-bonded silicon carbide, Int. J. Mach. Tools Manuf. 49 (2009) 366–374. doi:10.1016/j.ijmachtools.2008.12.007.

[103] K. Liu, X.P. Li, M. Rahman, K.S. Neo, X.D. Liu, A study of the effect of tool cutting edge radius on ductile cutting of silicon wafers, Int. J. Adv. Manuf. Technol. 32 (2007) 631–637. doi:10.1007/s00170-005-0364-7.

[104] S.K. Ajjarapu, J.A. Patten, H. Cherukuri, C. Brand, Numerical simulations of ductile regime machining of silicon nitride using the Drucker-Prager material model, Proc. Inst. Mech. Eng. Part C-Journal Mech. Eng. Sci. 218 (2004) 577–582. doi:10.1243/095440604774202204.

[105] J.A. Patten, J. Jacob, B. Bhattacharya, A. Grevstad, N. Fang, E.R. Marsh, Numerical simulations and cutting experiments on single point diamond machining of semiconductors and ceramics, in: J. Yan, J. Patten (Eds.), Semicond. Mach. Micro-Nano Scale, Transworld Research Network, Kerala, India, 2007. doi:10.1243/095440604774202204.

[106] J.A. Patten, J. Jacob, Comparison between numerical simulations and experiments for single-point diamond turning of single-crystal silicon carbide, J. Manuf. Process. 10 (2008) 28–33. doi:10.1016/j.jmapro.2008.08.001.

[107] T. Shibata, S. Fujii, E. Makino, M. Ikeda, Ductile-regime turning mechanism of single-crystal silicon, Precis. Eng. 18 (1996) 129–137. doi:10.1016/0141-6359(95)00054-2.

[108] J. Yan, T. Asami, H. Harada, T. Kuriyagawa, Crystallographic effect on subsurface damage formation in silicon microcutting, CIRP Ann. - Manuf. Technol. 61 (2012) 131–134. doi:10.1016/j.cirp.2012.03.070.

[109] J. Yan, Laser micro-Raman spectroscopy of single-point diamond machined silicon substrates, J. Appl. Phys. 95 (2004) 2094–2101. doi:http://dx.doi.org/10.1063/1.1639953.

[110] Y.G. Gogotsi, C. Baek, F. Kirscht, Raman microspectroscopy study of processing-induced phase transformations and residual stress in silicon, Semicond. Sci. Technol. 14 (1999) 936–944. doi:10.1088/0268-1242/14/11/501.

[111] Y. Yang, K. De Munck, R.C. Teixeira, B. Swinnen, B. Verlinden, I. De Wolf, Process induced sub-surface damage in mechanically ground silicon wafers, Semicond. Sci. Technol. 23 (2008) 75038. doi:10.1088/0268-1242/23/7/075038.

[112] T. Boukharouba, M. Elboujdaini, G. Pluvinage, eds., Damage and Fracture Mechanics, Springer Netherlands, Dordrecht, 2009. http://link.springer.com/10.1007/978-90-481-2669-9.

[113] J. Yan, K. Syoji, J. Tamaki, Some observations on the wear of diamond tools in ultra-precision cutting of single-crystal silicon, Wear. 255 (2003) 1380–1387. doi:10.1016/S0043-1648(03)00076-0.

[114] R. Wada, H. Kodama, K. Nakamura, Y. Mizutani, Y. Shimura, Wear Characteristics of Single Crystal Diamond Tool, CIRP Ann. - Manuf. Technol. 29 (1980) 47–52. doi:10.1016/S0007-8506(07)61293-1.

[115] C.J. Wong, Fracture and Wear of Diamond Cutting Tools, J. Eng. Mater. Technol. 103 (1981) 341–345. http://dx.doi.org/10.1115/1.3225025.

[116] D.I. Lalwani, N.K. Mehta, P.K. Jain, Experimental investigations of cutting parameters influence on cutting forces and surface roughness in finish hard turning of MDN250 steel, J. Mater. Process. Technol. 206 (2008) 167–179. doi:10.1016/j.jmatprotec.2007.12.018.

[117] F.B. de Oliveira, A.R. Rodrigues, R.T. Coelho, A.F. de Souza, Size effect and minimum

chip thickness in micromilling, Int. J. Mach. Tools Manuf. 89 (2015) 39–54. doi:10.1016/j.ijmachtools.2014.11.001.

[118] B.C. Rao, Y.C. Shin, A comprehensive dynamic cutting force model for chatter prediction in turning, Int. J. Mach. Tools Manuf. 39 (1999) 1631–1654. doi:10.1016/S0890-6955(99)00007-3.

[119] S.S. Joshi, S.N. Melkote, An Explanation for the Size-Effect in Machining Using Strain Gradient Plasticity, J. Manuf. Sci. Eng. 126 (2004) 679. doi:10.1115/1.1688375.

[120] M.C. Shaw, A Quantized Theory of Strain Hardening as Applied to the Cutting of Metals, J. Appl. Phys. 21 (1950) 599–606. doi:10.1063/1.1699714.

[121] M.C. Shaw, The size effect in metal cutting, Sadhana. 28 (2003) 875–896. doi:10.1007/BF02703319.

[122] M.R. Lovell, P. Cohen, P.L. Menezes, R. Shankar, Tribological Characterization of Machining at Very Small Contact Areas, J. Tribol. 131 (2009) 42201–42207. http://dx.doi.org/10.1115/1.3195038.

[123] S. Subbiah, Some investigations of scaling effects in micro-cutting, Georgia Institute of Technology, 2006.

[124] a. J. Mian, N. Driver, P.T. Mativenga, Identification of factors that dominate size effect in micro-machining, Int. J. Mach. Tools Manuf. 51 (2011) 383–394. doi:10.1016/j.ijmachtools.2011.01.004.

[125] I.H. Ahn, S.K. Moon, J. Hwang, An efficient way of investigating the intrinsic size effect in machining, Proc. Inst. Mech. Eng. Part B J. Eng. Manuf. 230 (2016) 1622–1629. doi:10.1177/0954405415612378.

[126] C. Wlesner, Residual stresses after orthogonal machining of AISI 304: numerical calculation of the thermal component and comparison with experimental results, Metall. Trans. A. 23A (1992) 989–996.

[127] M. Weber, T. Hochrainer, P. Gumbsch, H. Autenrieth, L. Delonnoy, V. Schulze, D. Löhe, J. Kotschenreuther, J. Fleischer, Investigation of size-effects in machining with geometrically defined cutting edges, Mach. Sci. Technol. 11 (2007) 447–473. doi:10.1080/10910340701697086.

[128] J. Chae, S.S. Park, T. Freiheit, Investigation of micro-cutting operations, Int. J. Mach. Tools Manuf. 46 (2006) 313–332. doi:10.1016/j.ijmachtools.2005.05.015.

[129] W. Grzesik, Advanced machining processes of metallic materials : theory, modelling and applications, Elsevier, 2008. http://www.sciencedirect.com/science/book/9780080445342.

[130] N. Ikawa, S. Shimada, H. Tanaka, Minimum thickness of cut in micromachining, Nanotechnology. 3 (1992) 6–9. doi:10.1088/0957-4484/3/1/002.

[131] X. Lai, H. Li, C. Li, Z. Lin, J. Ni, Modelling and analysis of micro scale milling considering size effect, micro cutter edge radius and minimum chip thickness, Int. J. Mach. Tools Manuf. 48 (2008) 1–14. doi:10.1016/j.ijmachtools.2007.08.011.

[132] M. Malekian, M.G. Mostofa, S.S. Park, M.B.G. Jun, Modeling of minimum uncut chip thickness in micro machining of aluminum, J. Mater. Process. Technol. 212 (2012) 553–559. doi:10.1016/j.jmatprotec.2011.05.022.

[133] L. Zhanqiang, S. Zhenyu, W. Yi, Definition and determination of the minimum uncut chip thickness of microcutting, Int. J. Adv. Manuf. Technol. 69 (2013) 1219–1232. doi:10.1007/s00170-013-5109-4.

[134] A. Elkaseer, S. Dimov, D. Pham, K. Popov, L. Olejnik, A. Rosochowski, Material microstructure effects in micro-endmilling of Cu99.9E, Proc. Inst. Mech. Eng. Part B J. Eng. Manuf. (2016). doi:10.1177/0954405416666898.

[135] S.M. Son, H.S. Lim, J.H. Ahn, Effects of the friction coefficient on the minimum cutting thickness in micro cutting, Int. J. Mach. Tools Manuf. 45 (2005) 529–535. doi:10.1016/j.ijmachtools.2004.09.001.

[136] Y. Altintas, Manufacturing Automation: Metal Cutting Mechanics, Machine Tool Vibrations, and CNC Design, Second, Cambridge University Press, New York, 2012. http://www.automationworld.com/print/14018.

[137] M.R. Shankar, B.C. Rao, S. Lee, S. Chandrasekar, A.H. King, W.D. Compton, Severe plastic deformation (SPD) of titanium at near-ambient temperature, Acta Mater. 54 (2006) 3691–3700. doi:10.1016/j.actamat.2006.03.056.

[138] T. Kitagawa, A. Kubo, K. Maekawa, Temperature and wear of cutting tools in high-speed machining of Inconel 718 and Ti-6Al-6V-2Sn, Wear. 202 (1997) 142–148.

doi:10.1016/S0043-1648(96)07255-9.

[139] A.L. Mantle, D.K. Aspinwall, Surface integrity and fatigue life of turned gamma titanium aluminide, J. Mater. Process. Technol. 72 (1997) 413–420. doi:10.1016/S0924-0136(97)00204-5.

[140] A. Jawaid, C.H. Che-Haron, A. Abdullah, Tool wear characteristics in turning of titanium alloy Ti-6246, J. Mater. Process. Technol. 92–93 (1999) 329–334. doi:10.1016/S0924-0136(99)00246-0.

[141] R.B. Da Silva, Á.R. Machado, E.O. Ezugwu, J. Bonney, W.F. Sales, Tool life and wear mechanisms in high speed machining of Ti–6Al–4V alloy with PCD tools under various coolant pressures, J. Mater. Process. Technol. 213 (2013) 1459–1464. doi:10.1016/j.jmatprotec.2013.03.008.

[142] N. Zlatin, M. Field, Procedures and Precautions in Machining Titanium Alloys, in: R.I. Jaffee, H.M. Burte (Eds.), Titan. Sci. Technol., Springer US, Boston, MA, 1973: pp. 489–504. doi:10.1007/978-1-4757-1346-6_37.

[143] A.G. Thornton, J. Wilks, Tool wear and solid state reactions during machining, Wear. 53 (1979) 165–187. doi:10.1016/0043-1648(79)90226-6.

[144] J. Kohlscheen, H.-R. Stock, P. Mayr, Tailoring of diamond machinable coating materials, Precis. Eng. 26 (2002) 175–182. doi:10.1016/S0141-6359(01)00109-X.

[145] J. Qian, C. Pantea, G. Voronin, T.W. Zerda, Partial graphitization of diamond crystals under high-pressure and high-temperature conditions, J. Appl. Phys. 90 (2001) 1632–1637. doi:10.1063/1.1382832.

[146] H. Liu, L. Wang, A. Wang, T. Lou, B. Ding, Z. Hu, Preparation of nanometer size TiC particulate reinforcements in Ti matrix composites under high pressure, Nanostructured Mater. 9 (1997) 177–180. doi:10.1016/S0965-9773(97)00047-0.

[147] B. Mills, A.H. Redford, Machinability of Engineering Materials, Springer Netherlands, Dordrecht, 1983. doi:10.1007/978-94-009-6631-4.

[148] I.D. Marinescu, M. Hitchiner, E. Uhlmann, W.B. Rowe, I. Inasaki, Handbook of machining with grinding wheels, CRC press, Taylor & Francis Group, 2007. doi:10.1007/s13398-014-0173-72.

[149] H.C.S. ASM International, ASM Handbook, Volume 16, Machining, ASM International, 1989.

[150] H. Abdel - Gawad El - Hofy, Fundamentals of Machining Processes: Conventional and Nonconventional Processes, Second, CRC Press, Taylor & Francis Group, 2014.

[151] M. Sekulić, Z. Jurković, M. Hadžistević, M. Gostimirović, the Influence of Mechanical Properties of Workpiece Material, Metalurgija. 49 (2010) 339–342.

[152] R.G. Budynas, J.K. Nisbett, Shigley’s Mechanical Engineering Design, Ninth, McGraw-Hill, New York, NY, 2008. doi:10.1007/s13398-014-0173-7.2.

List of achievements

Articles in periodicals (related to thesis)

Heidari, M. and Yan, J., 2017, Ultraprecision surface flattening of porous silicon by diamond turning*, Precision Engineering,* 49, pp.262–277.

Heidari, M. and Yan, J., 2017, Fundamental characteristics of material removal and surface formation in diamond turning of porous carbon, *International Journal of Additive and Subtractive Materials Manufacturing,* 1(1), pp.23-41.

Heidari, M. and Yan, J., 2017, Nanometric-scale chip formation behavior of pure titanium in diamond turning, *The International Journal of Advanced Manufacturing Technology,* (DOI: 10.1007/s00170-017-1185-1) [Accepted for publication].

Heidari, M. and Yan, J., 2018, Material removal mechanism and surface integrity in ultraprecision cutting of porous titanium, *Precision Engineering,* [Accepted for publication].

Articles in international conference proceedings

Heidari, M. and Yan, J., 2015, Investigation on surface formation mechanism of porous carbon in diamond turning, *Proceedings of International Conference on Leading Edge Manufacturing in 21st century*, Kyoto, Japan.

Heidari, M. and Yan, J., 2018, Effects of pore size and cutting scale on machining of porous titanium, *Proceedings of 5th Annual of International Conference on Materials Science, Metal and Manufacturing*, Singapore [Accepted for publication].

Presentations at international conferences

Heidari, M. and Yan, J., 2016, Ultraprecision surface flattening of porous single-crystal silicon by diamond turning, *International Symposium on Micro-Nano Science and Technology*. 16-18 December, Tokyo, Japan.